Universities of Glasgow and Strathclyde,
Department of Naval Architecture and Marine Engineering.

On the kinematics of an alternative extreme wave

by

Nwaka Chuks Ojieh

A thesis presented in fulfilment of the requirements for the degree of
Doctor of Philosophy

2009

This thesis is the result of the author's original research. It has been composed by the author and has not been previously submitted for examination which has led to the award of a degree.

Some parts of this thesis have been published or accepted for publication in the journal of Ocean Engineering, 2009; proceedings of the international conference on Offshore Mechanics and Arctic Engineering, Lisbon 2008; international conference on Offshore and Polar Engineering, Vancouver 2008 and international Floating structures conference, Glasgow 2009; respectively.

Signed: Date:

ACKNOWLEDGEMENT

I wish to express my sincere gratitude to Prof. Nigel Barltrop for the opportunity to under-take this research. I am greatly indebted to him for his guidance, support, encouragement and the opportunity to tap from his vast wealth of experience in Fluid-loading and Marine/offshore structural analysis. I am grateful for the sponsorship of Nigeria's Petroleum Technology Development Fund. I am also grateful to research colleagues and staff at the joint department of Naval Architecture and Marine Engineering of the Universities of Glasgow and Strathclyde for making my stay at the department worthwhile. I am especially indebted to Dr. Li Xu for never getting tired of my constant and prolonged queries and to Dimitrios Mylonas, Cammile Azzi, Nicholas Rousselon and Dr. Clemence Strasser for sharing their knowledge of CFD with me. I would also like to thank Thelma Will for ensuring that everything was always sorted and under control. Last but not least, I would like to express my sincere gratitude to my family for their support and encouragement and to God for the ability.

Glasgow,
December, 2009.

Contents

FIGURES

ABSTRACT

Although the majority of extreme wave investigations have focused on the traditional extreme wave (new-wave) there have been a few published deep-water investigations on the importance of wave-shape. Using a viscous-flow model, the present work has added to the understanding of the implication of wave-shape by identifying the kinematics in the alternate extreme waves defined in terms of height and front-steepness respectively. It was observed that although the alternative wave is not as high as the traditional extreme wave it can produce more severe kinematics and by extension, higher wave-loads on marine structures depending on the type of structure. Interestingly, vertical convective particle accelerations obtained suggests a need for ensuring consistency in the definition of the various components of vertical wave-load within the context of conventional strip theory. As the conventional Engineering kinematics models (stretching and extrapolation methods) could not predict the observed kinematics, it was attempted to develop a model which is based on similar simple modification to linear theory and second order accurate for calculating water particle kinematics in large waves. Based on a similar idea and a simplified way of including higher order effects, the method is extended to a non-linear form. The effectiveness of the method in predicting the kinematics of the traditional and alternative extreme waves investigated was explored. Finally, an attempt was made to answer the question of how small a model extreme wave can be without being significantly modified by the effect of surface tension. This is important in laboratory testing of extreme (especially deep-water) waves where the length scale is so small that surface tension effects become sufficiently severe to make the model waves a poor representation of the full-scale wave. Some rational guidance on mitigating this effect in laboratory investigations of breaking-wave loads has been proposed.

1. Introduction

“It was a wall of water; it was as if we had fallen into a hole in the sea; it towered over the boat; it came out of nowhere”. These phrases conjure up frightening images of the sort seen in very bad dreams but were the phrases used in the accounts of extreme wave incidents reported in Smith (2006). These kinds of waves have been explained as the reason for such damages as that of the Norwegian tanker- Wilstar, in 1974 (Choi, 2005).

Figure 1.1: Damage to Wilstar as a result of a rogue wave in 1974. (Choi, 2005)

Even more worrying is the prospect that waves need not be as high as the popularly known rogue waves, in order to unleash a devastating blow such as the one suffered by BP’s Schiehallion FPSO in 1998 and shown in figure 1.2.

Figure 1.2: Wave impact damage to the bow of Schiehallion FPSO in 1998. (Xu, 2006)

The fact that the damage was localized below the fore-castle suggested that the height of the wave which caused the damage was abnormally low relative to the amount of force required to do such damage. So the possibility of such a wave with sufficient energy to damage bow-plating probably designed to withstand even higher waves is of greater concern than the conventional high rogue wave.

An interesting question then is: are such extreme waves real or are there alternative explanations to the damages mentioned above? If these waves are real, is it possible to theoretically explain and demonstrate (in the context of existing knowledge of wave-loading) the magnitude of loads they exert especially those due to waves whose height appear abnormally low for the degree of damage they cause?

1.1 Extreme wave Loading

The study of extreme waves has become very important since the recording of the “New-Year wave” at the Draupner platform in the north-sea. One of such studies has been the European SAFEFLOW project where it was demonstrated that steep-fronted waves can result in unexpectedly high impact pressures capable of causing damage to a marine structure in deep-water (Voogt and Buchner, 2004). An extensive record of real extreme wave accidents involving a whole range of marine structures in the past several decades is presented in Smith (2006, 2007). According to this record, at least 10 vessels were either capsized or severely damaged by extreme waves in 2006 alone. Apart from inducing large bending loads on ships by the fact of the height of extreme waves, the height is such that the structure's freeboard or air-gap may be exceeded, resulting in inundation of the deck. Extreme waves can also result in vessel motions that are so large that the vessel's bottom emerges from the water and slams back into the water in the downward part of the motion cycle. A similar event where the extreme wave can be so steep that it hits the structure as a vertical wall can occur, resulting in severe impulsive loads. These dynamic loads can thus induce dynamic responses (e.g whipping, ringing) in the structure. Large vessel motions due to extreme waves can also result in very large rolling motions which may compromise the stability of a vessel and result in capsize. Unfortunately, the theoretical description of these effects (i.e in extreme waves) is still unclear.

With the NewWave theory of Tromans et al (1991) it is possible to define the highest wave that is most likely to be seen in a given sea-state by essentially scaling the autocorrelation function of the underlying spectrum with typically, the one in three hour amplitude. Based on this most probable extreme value, Tromans and

Vandershuren (1995) have presented a method for estimating the maximum extreme.

1.2 An alternative extreme

Since the work of Tromans et al (1991), much work has been done using the concept of the most probable extreme wave but the understanding of "extreme" in the majority of these investigations has been with respect to wave-height. However, in the investigation of extreme (typically asymmetric) waves conducted by Kjeldsen and Myrhaug (1979), it was concluded that front steepness is similarly if not more relevant than the traditional definition of wave steepness which depended on height since the magnitude of shock pressures recorded in their experiment depended on the wave-form which they did not find to have a unique relationship with the traditional definition of wave-steepness based on height. Furthermore, it was found in the investigation of wave forces and overturning moments on a slender stiff cylinder by Kjeldsen et al(1986) that responses induced by a moderate but breaking deep-water wave was much higher than those induced by a much larger wave similar to the traditional design wave (most probable highest wave).

Therefore, an alternative extreme wave may be defined in terms of maximized front-steepness to give the steepest wave that is most likely to occur in a sea-state by applying the new-wave theory to the spectrum of surface slope instead of the spectrum of surface amplitude as in the traditional extreme wave (most probable highest wave) characterized by height. This definition was developed and used by Xu and Barltrop (2005, 2008 (1)) to conduct experimental investigation of steep wave impact on FPSO bows and a surface piercing vertical cylinder in shallow water. It is useful to note that earlier, Drake (1997, 2000, and 2001) used similar most probable extreme value statistics to obtain the shape of the wave which produced the most probable extreme green water and linear hull-girder wave-loads respectively by scaling the auto-correlation function of the linear hull-girder response spectrum with maximum mid-ship moment and bow-motion. It is suggested in Xu and Barltrop (2005) that the alternative class of extreme waves defined in terms of the statistics of extreme wave-front steepness is connected to the bow-damage suffered by BP's Schiehallion FPSO in 1998. The indication that the wave was not as high as what would be normally termed "rogue" appeared to contradict conventional offshore engineering practice where design conditions for many classes of fixed and floating structures were based on the assumption that maximum particle kinematics and by extension maximum wave-loading, occur in the highest waves due to the exponential increase in horizontal particle velocities with height.

Although an extensive record of impact loads and hull-girder bending responses was documented by Xu (2006), wave kinematics was not recorded. Similarly, the relative severity of the kinematics of the alternate extreme waves was not specifically investigated. Therefore the calculations presented by Xu and Barltrop (2008 (2)) and Xu et al (2007) for impact pressures and underlying kinematics, were based on empirically modified linear theory and strictly linear theory, respectively. However, extreme waves are highly non-linear and more robust investigation of the kinematics of the alternative extreme wave is necessary in order to theoretically explain the resulting loads and how it differs from those of the traditional new-wave (most probable highest wave).

This is especially important since most probable extreme value statistics indicates that the steepest wave that is most likely to be encountered in a sea-state will be considerably lower than the highest wave that is most likely to occur in the same sea-state. This raises the question of how the kinematics of the so called most probable highest wave and by extension induced loads, compare with those of the steepest wave that is most likely to occur in the same sea-state. It also raises the question: is there any remarkable difference in how this alternative extreme wave affects floating and fixed structures and if so, what are the practical implications?

1.3 Scale effects

Another question in the study of extreme waves is the effect of surface tension due to the scaling down of the full-scale wave to only a few tens of centimetres in order to fit physical wave-tank size-limitations. Such small-length scales inevitably increase the effect of surface tension which at sufficiently low scales, would be expected to result in the model scale wave being a poor representation of the full scale wave. Conventional texts deal with this problem for sinusoidal waves but the high surface curvatures in the crests of breaking waves suggest that the conventional guidance allow smaller waves than would be satisfactory. This therefore raises the question: to what extent do model-scale waves accurately represent full-scale waves and how can we tell that the results of extreme wave laboratory investigations are valid for realistic ocean waves?

1.4 Objectives

It is intended in the present study to explore the questions raised in sections 1.2 and 1.3 above. It is hoped to achieve this by:

- investigating the relative severity of the kinematics of the traditional and alternative extreme waves using a range of analytical and numerical models.

- exploring possible modifications to linear wave theory to reasonably improve prediction of extreme wave kinematics, without requiring large amounts of computational resources .

- investigating the effect of surface tension on extreme waves using a breaking wave simulated at various length scales, with a view to determining how small a model extreme wave can be without being significantly modified by the effect of surface tension.

- demonstrating the implications of observed kinematics on a floating structure and on a fixed structure.

It is hoped that completion of the above tasks will help establish the kinematics of extreme waves in general and in particular, the relative severity of the steepest and highest waves that are most likely to be seen in a sea-state thereby improving the understanding of what the “design wave” should really be in the context of the nature and theoretical basis of the load induced by extreme-waves. It is also expected that completing these tasks will culminate in a rational method for determining the minimum model length-scale required to ensure that a model extreme wave is a good representation of the actual wave.

1.5 Outline of Thesis

A theoretical background of free-surface flows is presented in Chapter two and the basic equations of viscous and potential flow is derived. Here also, potential flow wave theory is presented and the various simplified models for calculating wave kinematics are reviewed. An overview of experimental and full-scale investigations of the kinematics of extreme waves reported in literature by other authors is also given. In Chapter three, the kinematics of the traditional and alternative extreme waves are investigated using a numerical wave-tank implemented in a commercial viscous flow solver and wave-loads are inferred from the observed kinematics. Following in Chapter four, wave impact pressures are directly obtained from the numerical model of Chapter three by measuring the force on a 1m^2 panel placed at the position of the extreme wave-crest. In Chapter five, a simplified model which is based on a simple modification to linear theory is developed for calculating water particle kinematics in large waves. Based on a similar idea and a simplified way of including higher order effects, the method is extended to a non-linear form. The effectiveness of this method (and some of the methods reviewed in chapter two) in predicting the kinematics of the traditional and alternative extreme waves obtained from the simulation results of Chapter three is also explored in this Chapter. In Chapter six, the loading implications of the observed kinematics on a fixed and a floating structure, are respectively demonstrated. Using the same wave-tank of Chapter three, the effect of surface tension on a breaking traditional NewWave as well as an alternative extreme wave that is breaking is explored in Chapter seven, culminating in the recommendation of a minimum laboratory scale sea-state for investigating breaking wave effects on marine structures. Finally in Chapter eight, the entire work is summarized and the salient contributions outlined.

1.6 Contributions

The present work has contributed to better understanding of extreme waves in the following ways:

1. **Better understanding of the kinematics of an alternative extreme wave**: Although the majority of extreme wave investigations have focused on the traditional NewWave, there have been a few published deep-water investigations on the importance of wave-shape. Using a viscous flow model, the present work has added to the understanding of the implication of wave-shape by identifying the kinematics in the alternate extreme waves defined in terms of height and front-steepness respectively.

2. **Better understanding of the effect of the alternate extreme waves on various types of structures:** By applying the identified kinematics to rate of change of momentum, Morison equation and strip/linear diffraction theory, better understanding of the dramatic difference in the forces exerted by the alternate extreme waves has been realized. On the basis of the obtained forces, it is shown that the relative importance of the alternate extreme waves is dependent on the type of structure (floating or fixed, mono-cylinder or multi-leg etc) and loading type (vertical or horizontal, drag or inertial, impact or quasi-static) in question. This work can therefore serve as a guide for determining the appropriate wave (or combination of waves), critical to the performance of a given marine structure.

3. **Guidance on the effect of convective acceleration in extreme waves:** There has long been a debate about the significance of convective acceleration in wave-loading. For example, the conventional strip theory implicitly assumes that convective acceleration is negligible. Similarly, API RP 2A-LRFD (C.3.2.10) recommends that convective acceleration be neglected. While this recommendation may be valid for most fixed structures in practice, the present work has shown that it is not necessarily applicable to a typical floating (partially submerged) structure. It has been shown that the neglect of convective acceleration can result in under-estimation of the wave-load on the bottom of a floating (partially submerged) structure in extreme waves .

4. **Guidance on alleviating surface tension effects:** In the investigation of breaking waves, the effect of surface-tension on small (model-scale) waves have been long recognized but there has been very little or definitive guidance on how small a focused extreme wave can be before surface-tension effects become significant. The readily available guidance is based on regular wave dispersion relation (figure 7.2) which suggests that surface-tension effect set-in at wave periods of 0.3s and less. This cannot be applied to irregular waves and it has been shown in Chapter 7 that in breaking waves (generated by focusing), the effect of surface tension is quite considerable even in waves that are much larger than the dispersion relation will seem to suggest. By comparing extreme particle velocities and surface elevation observed in viscous-flow simulation at various model scales with those observed in a full-scale wave simulated in the same way, separate laboratory sea-states (characterized by T_z and H_s) have been identified as reasonable thresholds for the traditional and alternative extreme waves respectively, below which a laboratory wave will be a poor representation of the equivalent full-scale breaking wave.

5. **New simple method for resolving the problem of high frequency contamination:** Although several sophisticated non-linear wave models exist, simpler methods are desirable and several of such methods which essentially seek to remedy the problem of high frequency contamination inherent in the linear wave theory, are in existence. However, these methods are known to give unsatisfactory results especially in the crest of steep

waves. In this work, the problem of frequency contamination is resolved by allowing the spectral components of a random wave-field to "ride-over one another" in a systematic and rational way.

6. **Adaptation of the 5th order NewWave theory to wave kinematics:** The 5th order NewWave theory of Walker et al (2005), which deals with water surface elevation has been modified and developed into a method for calculating more non-linear particle kinematics.

2. Dynamics of Free-Surface Flows

Waves are essentially a propagation of energy through a medium. Therefore, in the case of water surface waves, their nature at some point in the medium is largely dependent on the physical properties of the water and is also related to the air above it. According to Barltrop and Adams (1991), these governing physical properties are density, viscosity, compressibility and surface tension in the case of the flow of water in waves. In practice, the propagation of water waves without turbulent fluid-structure interactions is usually assumed to be irrotational and the effect of viscosity of the water, the air above and surface tension of the water is neglected. However, in very steep waves such as are inherent in slapping seas, the effect of these factors (viscosity of the water, effect of the air above and surface tension of the water) are not very clear and need further investigation. The discussion in this chapter presents the general governing equations of fluid dynamics and how they give rise to the main equations of water wave theory.

In the mathematical description of waves, it is held that there is no flow through the free-surface and therefore the flow velocity normal to the surface must be equal to the normal velocity of the surface itself. Also, since the sea-bed is a solid boundary, there is no flow through it implying that vertical velocity is zero at the sea-bed. These two conditions constitute the so called kinematic boundary conditions. Also, mass and energy are conserved i.e dynamic equilibrium (acceleration=force/mass) and continuity (no net mass transport out) conditions apply. The application of these boundary conditions to the solution of Newton’s second law of motion for a fluid element results in the so called Navier-Stokes equation (see appendix A1 for derivation):

$$\frac{\partial u}{\partial t} + u\frac{\partial u}{\partial x} + \mathrm{v}\frac{\partial u}{\partial y} + w\frac{\partial u}{\partial z} = -\frac{1}{\rho}\frac{\partial P}{\partial x} + 0 + \upsilon\left(\frac{\partial^2 u}{\partial x^2} + \frac{\partial^2 u}{\partial y^2} + \frac{\partial^2 u}{\partial z^2}\right) \qquad 2.1$$

$$\frac{\partial \mathrm{v}}{\partial t} + u\frac{\partial \mathrm{v}}{\partial x} + \mathrm{v}\frac{\partial \mathrm{v}}{\partial y} + w\frac{\partial \mathrm{v}}{\partial z} = -\frac{1}{\rho}\frac{\partial P}{\partial y} + 0 + \upsilon\left(\frac{\partial^2 \mathrm{v}}{\partial x^2} + \frac{\partial^2 \mathrm{v}}{\partial y^2} + \frac{\partial^2 \mathrm{v}}{\partial z^2}\right) \qquad 2.2$$

$$\frac{\partial \mathrm{w}}{\partial t} + u\frac{\partial \mathrm{w}}{\partial x} + \mathrm{v}\frac{\partial \mathrm{w}}{\partial y} + w\frac{\partial \mathrm{w}}{\partial z} = -\frac{1}{\rho}\frac{\partial P}{\partial z} - g + \upsilon\left(\frac{\partial^2 \mathrm{w}}{\partial x^2} + \frac{\partial^2 \mathrm{w}}{\partial y^2} + \frac{\partial^2 \mathrm{w}}{\partial z^2}\right) \qquad 2.3$$

When viscosity is neglected ($\upsilon = 0$), the Navier-Stokes equation reduces to:

$$\frac{\partial u}{\partial t} + u\frac{\partial u}{\partial x} + \mathrm{v}\frac{\partial u}{\partial y} + w\frac{\partial u}{\partial z} = -\frac{1}{\rho}\frac{\partial P}{\partial x} \qquad 2.4$$

$$\frac{\partial \mathrm{v}}{\partial t} + u\frac{\partial \mathrm{v}}{\partial x} + \mathrm{v}\frac{\partial \mathrm{v}}{\partial y} + w\frac{\partial \mathrm{v}}{\partial z} = -\frac{1}{\rho}\frac{\partial P}{\partial y} \qquad 2.5$$

$$\frac{\partial \mathrm{w}}{\partial t} + u\frac{\partial \mathrm{w}}{\partial x} + \mathrm{v}\frac{\partial \mathrm{w}}{\partial y} + w\frac{\partial \mathrm{w}}{\partial z} = -\frac{1}{\rho}\frac{\partial P}{\partial z} - g \qquad 2.6$$

These are known as the Euler equations.

2.3 Surface Tension

The effect of surface tension is quite an important force in the flow of inter-facing fluids and is only neglected in the usual description of waves since gravity forces dominate in most cases. Therefore a good theoretical description of fluid flow would normally include surface tension. This is achieved by modelling surface-tension effect as a pressure jump at the free surface represented as a volume force:

$$\boldsymbol{\Delta P = \gamma\left(\frac{1}{r_1} + \frac{1}{r_2}\right)} \qquad \mathbf{2.7}$$

This pressure is added as a source term in the Navier-Stokes equation. The derivation of equation *2.7* is presented in Appendix A2.

2.4 Boundary Conditions

The conditions at the sea-bed and the water surface are known and can be used to solve the above Navier-Stokes equations. These constitute the kinematic boundary conditions.

2.4.1 Sea-Bed

As there is no flow through the sea-bed, the normal velocity component *w* is zero. It implies that $\frac{\partial \Phi}{\partial z} = 0$.

2.4.2 Water Surface

It is assumed that there is no flow across the water-air boundary which implies as earlier mentioned that the flow velocity normal to the surface must be equal to the normal velocity of the surface itself. If the free surface elevation is described by ζ and recalling that the velocity potential Φ is defined such that its gradient gives the velocity vector, the vertical velocity component *w* is given by $w = \frac{\partial \Phi}{\partial z}$ so that the above assumption of no flow across the free surface implies that:

$$\boldsymbol{w = \frac{\partial \Phi}{\partial z} = \frac{\partial \zeta}{\partial t} + \frac{\partial \Phi}{\partial x}\frac{\partial \zeta}{\partial x}} \qquad \mathbf{2.8}$$

Assuming that the free surface is of constant pressure, yet another boundary condition (dynamic free surface condition) applies based on Bernoulli's equation.

2.5 Bernoulli's Pressure Equation

By introducing the velocity potential Φ satisfying the Laplace equation:

$$\frac{\partial^2 \Phi}{\partial x^2} + \frac{\partial^2 \Phi}{\partial y^2} + \frac{\partial^2 \Phi}{\partial z^2} = 0 \qquad \mathbf{2.9}$$

a pressure relationship which can be very useful in describing the free surface evolution, can be obtained. Since the focus is on gravity waves, the relevant equation is the z (vertical) component of the Navier-Stokes equations (equation *2.3*). Since the velocity potential Φ is defined such that $w = \frac{\partial \Phi}{\partial z}$, we can write that:

$$\frac{\partial w}{\partial t} = \frac{\partial}{\partial t}\left(\frac{\partial \Phi}{\partial z}\right) = \frac{\partial^2 \Phi}{\partial z \partial t} \qquad \mathbf{2.10}$$

Substituting equation *2.10*, the Laplace condition i.e equation *2.9* written as:

$$\frac{\partial^2 \Phi}{\partial x^2} + \frac{\partial^2 \Phi}{\partial y^2} + \frac{\partial^2 \Phi}{\partial z^2} = \frac{\partial u}{\partial x} + \frac{\partial v}{\partial y} + \frac{\partial w}{\partial z} = 0$$

and the irrotational flow condition ($\frac{\partial u}{\partial y} = \frac{\partial v}{\partial x}$, $\frac{\partial v}{\partial z} = \frac{\partial w}{\partial y}$, $\frac{\partial w}{\partial x} = \frac{\partial u}{\partial z}$) into the z component of the Navier-Stokes equations (equation *2.3*) we have:

$$\frac{\partial^2 \Phi}{\partial z \partial t} + u\frac{\partial u}{\partial z} + v\frac{\partial v}{\partial z} + w\frac{\partial w}{\partial z} = -\frac{1}{\rho}\frac{\partial P}{\partial z} - g \qquad \mathbf{2.11}$$

Integrating equation 2.11 with respect to z yields:

$$\frac{\partial \Phi}{\partial t}+\frac{1}{2}(u^2+v^2+w^2)=-\frac{P}{\rho}-gz+c(t) \qquad 2.12$$

Thus the Bernoulli equation is obtained as :

$$\frac{\partial \Phi}{\partial t}+\frac{1}{2}(u^2+v^2+w^2)+\frac{P}{\rho}+gz=c(t) \qquad 2.13$$

By introducing the velocity potential relationship for irrotational flows and assuming a constant reference (gauge) atmospheric pressure of zero at the free surface where z = ζ(t) and that energy is conserved (c = 0 in equation 2.13), the Bernoulli equation can be written at the free surface as:

$$\rho\left\{\frac{\partial \Phi}{\partial t}+\frac{1}{2}\left[\left(\frac{\partial \Phi}{\partial x}\right)^2+\left(\frac{\partial \Phi}{\partial y}\right)^2+\left(\frac{\partial \Phi}{\partial z}\right)^2\right]+g\zeta\right\}=0 \qquad 2.14$$

Since $\rho \neq 0$, equation *2.15* implies that:

$$\frac{\partial \Phi}{\partial t}+\frac{1}{2}\left[\left(\frac{\partial \Phi}{\partial x}\right)^2+\left(\frac{\partial \Phi}{\partial y}\right)^2+\left(\frac{\partial \Phi}{\partial z}\right)^2\right]+g\zeta=0 \qquad 2.15$$

By linearizing equation *2.15* we have:

$$\frac{\partial \Phi}{\partial t}+g\zeta=0 \qquad 2.16$$

Therefore, the time history of free surface elevation above the mean water surface may be given as :

$$\zeta(t) = -\frac{1}{g}\frac{\partial\Phi}{\partial t} \qquad 2.17$$

This is the dynamic free-surface condition which describes the wave (elevation of the free surface) when potential flow is assumed. The beauty of this potential method is that from this one scalar (velocity potential) all velocity components and free surface elevation history is obtained.

2.6 Wave theory

Most wave theories are based on potential-flow assumptions and are therefore, usually formulated in terms of the potential function, Φ or the analogous stream function ψ. The standard method is a perturbation expansion where Φ is expressed as power series in a small parameter ε which increases with wave steepness:

$$\Phi(x,y,z,t) = \varepsilon\,\Phi^{(1)}(x,y,z,t) + \varepsilon^2\,\Phi^{(2)}(x,y,z,t)\ldots\ldots\ldots + \varepsilon^n\,\Phi^{(n)}(x,y,z,t)$$

Where $\Phi^{(n)}$ represents expansion to the nth order.

2.6.1 Regular Waves

Regular wave theories model waves of same form repeating one another in water of constant depth without changing shape. Stokes used $\varepsilon = ak$ to obtain a solution of the perturbation to 3rd order, where $k = \frac{2\pi}{\lambda}$ (wave-number), λ is the wavelength and a is the wave amplitude at lowest order. Other authors (see e.g Fenton, 1985) have obtained solutions to higher orders and it is now conventional in the relationship $\varepsilon =$

ak, to take $a = \frac{H}{2}$ (elevation of the wave crest/trough relative to the mean water surface). The following discussion will start with the first order expansion.

2.6.1.1 Small Amplitude (Airy) Waves

Retention of only first order terms in the perturbation expansion gives rise to the most elementary wave theory (small-amplitude or linear wave theory) developed in 1845 by Airy and presented in Appendix A3. This first order theory gives the free-surface as:

$$\zeta(x,t) = a\cos(kx - \omega t) \qquad 2.18$$

And the velocity potential as:

$$\phi = a\frac{g}{\omega}\frac{\cosh[k(z+d)]}{\cosh(kd)}\sin(kx - \omega t)] \qquad 2.19$$

2.6.1.2 Fifth-Order Stokes Wave

Fenton (1985) extended the standard perturbation expansion to the fifth-order and and after a great amount of mathematical manipulation, gave the solution for kd/2π > 0.5 (deep water) as:

$$k\zeta(x) = kd + \epsilon\cos(kx) + \epsilon^2 B_{22}\cos(2kx) + \epsilon^3 B_{31}[\cos(kx) - \cos(3kx)] + \epsilon^4[B_{42}\cos(2kx) + B_{44}\cos(4kx)] + \epsilon^5[-(B_{53}+B_{55})\cos(kx) + B_{53}\cos(3kx) + B_{55}\cos(5kx) + 0(\epsilon^6)] \qquad 2.20$$

where $B_{22} = ½$, $B_{31} = -3/8$, $B_{42} = 1/3$, $B_{44} = 1/3$, $B_{53} = 99/128$ and $B_{55} = 125/384$. $0(\epsilon^6)$ represents higher order terms which are assumed negligible. The derivation is given in Appendix A4.

Since Fenton assumed $\epsilon = kH/2$ where $H/2 = a$ (wave amplitude), $\epsilon/k = a$. So by replacing the phasing (kx) in each term with $\theta = kx-\omega t$ in the light of Fenton's solution, we can write with respect to a mean surface elevation y=0, that:

$$\zeta(x,t) = a\cos(kx-\omega t) + a^2B_{22}\cos(2(kx-\omega t)) + a^3B_{31}[\cos(kx-\omega t) - \cos(3(kx-\omega t))] + a^4[B_{42}\cos(2(kx-\omega t)) + B_{44}\cos(4(kx-\omega t))] + a^5[-(B_{53}+B_{55})\cos(kx-\omega t) + B_{53}\cos(3(kx-\omega t)) + B_{55}\cos(5(kx-\omega t))] \qquad 2.21$$

2.6.2 Irregular Waves

In the linear theory, the ocean surface is regarded as being comprised of an infinite number of waves that are out-of-phase with each other and therefore irregularly super-imposed. This assumption is most appropriate for so called Airy (linear) waves and valid as long as the conditions are not extreme e.g very high front-steepness. Faltinsen (1990) states that the wave elevation of a long-crested irregular sea propagating along the positive x-axis can be written as the sum of a large number of wave components j:

$$\boldsymbol{\zeta(x,t) = \sum_{j=1}^{\infty} A_j \sin(\omega_j t - K_j x + \theta_j)} \qquad 2.22$$

where A_j, ω_j, k_j and θ_j are respectively wave amplitude, angular frequency, wave number and random phase angle of wave component j. The random phase angles θ_j are uniformly distributed between 0 and 2π and constant with time. It is very important to note the relevance of the random phasing without which the resultant wave will cease to be random.

As a result of this randomness the occurrence of waves in a natural sea-way is said to be a stochastic process. The analysis of this process is therefore usually presented statistically and the analysis of structures subject to their effect inevitably requires statistical calculations. In chapter 3 of Barltrop and Adams (1991), an excellent introduction to the statistics necessary for this analysis is presented.

2.6.2.1 The NewWave theory

As a result of the stochastic nature of real seas, a deterministic analysis although very useful, was not possible since an extreme event was randomly embedded and could not be pre-defined. To obtain an extreme event therefore, very long time histories were run. Tromans et al (1991) presented the "NewWave" theory which describes the average form of the extreme waves. The "NewWave" theory accounts for the random nature of the sea, and gives the most probable value of an extreme: notably, maximum wave crest elevation. By assuming that the surface elevation can be modelled as a Gaussian random process, the expected elevation at an extreme event is derived theoretically as a scaled autocorrelation function of the underlying spectrum, to first order. Individual wave components ζ_n and their phase angles ϕ_n

are determined based on probability theory, to represent the extreme event. The extreme event is pre-defined to occur at a position x known as the target position by choosing the individual phases in such a manner that they are co-phased at a time t known as the target time on the target position x. Therefore to determine the elevation ζ at any time τ i.e $\zeta(\tau)$, and given position (x, y) the wave crest is defined to occur at a time t=0 having elevation ζ_a and zero vertical velocity $\zeta'_a = 0$. The statistical average time history of the most probable wave with the predefined crest height is simply the deterministic component $\rho(\xi,\tau)\zeta a$ and the mean water surface elevation at time τ from the crest is the autocorrelation function multiplied by the crest elevation i.e

$$\zeta(\tau) = \rho(\tau)\zeta_a \tag{2.23}$$

Since the autocorrelation function $\rho(\tau)$ is the inverse-Fourier transform of the water-surface elevation spectrum, we can write:

$$\rho(\xi,\tau) = \tfrac{1}{\sigma^2}\int_0^\infty S_{\zeta\zeta}\cos(k\xi - 2\pi f\tau)d\omega = \tfrac{1}{\sigma^2}\sum_n S_{\zeta\zeta}(\omega_n)\cos(k_n\xi - 2\pi f_n\tau) \tag{2.24}$$

Therefore the amplitude ζ_n of the nth wave component is given by:

$$\boldsymbol{\zeta \mathbf{n} = S_{\zeta\zeta}(f_n)\frac{\zeta_a}{\sigma^2}} \tag{2.25}$$

2.6.2.2 Extended NewWave theory

In Xu and Barltrop (2005) the new-wave theory is modified to generate waves with varying front-steepnesses which essentially have the same likelihood of occurring as the unmodified (highest) wave. They reasoned that if $y = a\cos\left(x\,\frac{2\pi}{L}\right)$ is the elevation of a point on the wave, the slope at the point will be:

$$\frac{dy}{dx} = a\frac{2\pi}{L}\left[-\sin\left(x\,\frac{2\pi}{L}\right)\right] = -ak\left[\sin\left(x\,\frac{2\pi}{L}\right)\right] \qquad \mathbf{2.26}$$

Therefore, a complex transformation T(ω) can be empirically defined in terms of wave-number k(ω), front-steepness parameter α ($0 \le \alpha \le 1$, steepness-balance) and for dimensional consistency H_s, as :

$$T(\omega) = [(1-\alpha)/5H_s + i\alpha\, k(\omega)\,] \qquad 2.27$$

When this transformation is applied to the wave spectrum, a transformed (slope) spectrum S_{xx} is obtained and by applying the NewWave theory as described earlier, the shape of the (most probable) highest wave or steepest-wave (with α=0 and α=1 respectively) can be obtained by:

$$S_{XX}(\omega) = |T(\omega)|^2 S_{\varsigma\varsigma}(\omega\,) \qquad 2.28$$

And:

$$\chi_n = \frac{\chi_a}{\sigma_x^{\;2}} S_{XX}(\omega) \qquad 2.29$$

where σ_x^2 is the variance of the transformed quantity S_{xx} (i.e zeroth moment of the spectrum S_{xx}) and χ_n is the most probable maximum value of the transformed quantity within a duration N where:

$$\chi_a = \sigma_x^2 \sqrt{2\ln\left(\frac{N}{T}\right)} \quad 2.30$$

[1]

which is the slope exceeded once over a sampling duration of N (T is period of the quantity, therefore $\frac{N}{T}$ is the number of times the quantity occurred). To obtain the water surface elevation ζ_n for each n frequency component, corresponding to the maximum of the transformed value, the reverse transformation is applied:

$$\zeta_\mathbf{n} = \frac{\chi_n}{\mathbf{T}(\omega_n)} \quad 2.31$$

Similarly particle velocities are defined using magnitude and phases of the above complex amplitudes.

2.6.2.3 Higher Order NewWave

The original NewWave theory described above is only valid to first order and does not take into account the non-linearities inherent in very steep waves as seen in the extreme events. As a result, Walker et al (2005) extended the theory to the 5th order using Stokes-type corrections to approximately but robustly account for the higher order contributions.

---

[1] N represents the statistical time scale (typically 3 hours) and T is the duration of each occurrence, which is typically zero up-crossing wave-period

The non-linear time and spatial history of water surface elevation was given by Walker et al (2005) as:

$$\eta=S_{11}D_{11}+\frac{S_{22}}{d}D_{22}+\frac{S_{31}}{d^2}D_{31}+\frac{S_{33}}{d^2}D_{33}+\frac{S_{42}}{d^3}D_{42}+\frac{S_{44}}{d^3}D_{44}+\frac{S_{51}}{d^4}D_{51}+\frac{S_{53}}{d^4}D_{53}+\frac{S_{55}}{d^4}D_{55} \qquad 2.32$$

Where $S_{ij}=B_{ij}(k)^{i-1}$ (k may be taken as zero-crossing wave-number)

B_{ij} is Stokes co-efficient and S_{ij} is the modified form of the co-efficients. D_{ij} is given as follows:

$D_{11}=a\cos\theta = \eta_L$

$D_{22}= \eta^2_L - \eta^2_{LH}$

$D_{31}=(\eta^2_L + \eta^2_{LH}) \eta_L$

$D_{33}=(\eta^2_L - 3\eta^2_{LH}) \eta_L$

$D_{42}=(\eta^2_L + \eta^2_{LH})(\eta^2_L - 3\eta^2_{LH})$

$D_{44}=(\eta^2_L - \eta^2_{LH})^2 - (2\eta_L \eta_{LH})^2$

$D_{51}=(\eta^2_L + \eta^2_{LH})^2 \eta_L$

$D_{53}=(\eta^2_L + \eta^2_{LH})[\eta_L (\eta^2_L - 3\eta^2_{LH})]$

$D_{55}=(\eta^2_L - \eta^2_{LH})^2 - (2\eta_L \eta_{LH})^2 \eta_L - 4\eta^2_{LH} \eta_L(\eta^2_L - \eta^2_{LH})$

Where η_{LH} is the Hilbert transform of the linear quantity η_L.

Stokes corrections are given by coefficients which are expressed in terms of hyperbolic functions of kd where k is wave-number and d is water depth. Walker et al have proposed the three methods below for estimating the value of k:

- Use a wave-number value based on the peak frequency (i.e. the frequency of the most energetic waves);
- Use a local time-varying wave-number value based on an instantaneous effective frequency at each point in the record.
- Use a wave-number value based on the mean zero-crossing frequency;

In their computations however, Walker et al have used a single kd for all the components which is obtained by comparing their Stokes-type coefficient with the equivalent Stokes coefficient and for the 1520 record of the "New-Year" wave they obtained a value of kd=1.6.The result is a narrower and higher crest while troughs are broadened and raised as seen in the laboratory (see e.g Baldock et al, 1996; Barltrop and Xu, 2005) and full scale measurements of the "New-Year" wave (see e.g Walker et al, 2005). It is pertinent to note that the 5th order new-wave theory of Walker et al only predicted water surface elevation and was not concerned with water particle kinematics.

2.7 Review of wave-kinematics

The first stage in assessing the effects of waves on a structure is characterising and quantifying the load induced on the structure by the wave. Since the real sea is random, the usual way of determining wave-induced loads has been to assume that the sea surface can be represented by numerous waves of different frequencies which are randomly super-imposed. Through statistical analysis of environmental data relevant to the site, a design-wave characteristic of the wave-climate (e.g most probable wave height) is obtained and by combining it with an appropriate wave-theory the kinematics of the water can be simulated. Since the consequently induced force is largely dependent on the energy in the waves, the load induced by the wave can be obtained by applying the kinematics of the waves to a Momentum or Morison type of equation. Thus, the ability to establish inherent particle kinematics is crucial for determining the consequent wave loading. It is therefore not surprising for Stansberg and Karlsen (2001) to conclude from their experiments that in the most critical impact events observed in steep random wave conditions, kinematics of the incoming waves is critical to understanding the impact problem and should therefore be further investigated.

Although second order Fourier perturbation approaches (e.g Zhang et al, 1992, 1993a and Dean and Sharmer, 1981 as implemented by Stansberg et al, 2006 and Kim, 2008) and more sophisticated fully non-linear methods (see e.g Bateman et al, 2001; Yan and Ma, 2008 and Grue and Fructus, 2008) have been presented, simpler methods which are suitable for routine engineering calculations are desirable and are thus the eventual aim of the present work. Therefore the discussion of theoretical methods here is restricted to the various simplified methods presented in literature for routine engineering calculations.

2.7.1 Simple Theoretical methods

In the linear theory as earlier mentioned, the sea is assumed to be comprised of individual linear waves randomly super-imposed on each other so that the horizontal particle velocity is given by:

$$\boldsymbol{U} = \sum_j \boldsymbol{a_j \omega_j} \frac{\mathbf{cosh[k_j(z+d)]}}{\mathbf{sinh(k_j d)}} \mathbf{cos\theta_j} \qquad \mathbf{2.33}$$

Where a_j , ω_j, k_j, θ_j, z and d are amplitudes, frequencies, wave-numbers phases, vertical elevation an d water depth, of the j^{th} wave respectively . In deep water where d is very large, the term $\frac{\cosh[k_j(z+d)]}{\sinh(k_j d)}$ tends to $e^{kj\,z}$. Thus we have for deep water:

$$\boldsymbol{U} = \sum_j \boldsymbol{a_j \omega_j}\, \boldsymbol{e}^{\mathbf{k_j z}} \mathbf{cos\theta_j} \qquad \mathbf{2.34}$$

However, the e^{kjz} term increases very rapidly above MWL and can give rise to the phenomenon of "high frequency contamination". This inherent problem in applying linear theory to irregular waves is well known (see e.g Sobey, 1990; Forristall, 1986; Taylor, 1992) and results in the exponential velocity profile being highly biased towards the higher frequency components above MWL, thereby giving extremely large and spurious velocities further up the wave crest. This is because the exponential term becomes very large at higher frequency and spuriously so at higher elevations as the baseline for all the elevation of any frequency component is taken to be the MWL. Sutherland et al (1991) explain the phenomenon as the lifting-up of small, high frequency wave components above MWL by much longer waves which results in a situation where $k_j\, z > 1$ and so, $e^{kj\,z}$ becomes very large.

Wheeler (1970) attempted solving this problem by stretching the vertical co-ordinate of each component such that velocity calculated for the individual wave component with height η_j is that given to the surface. This is implemented by replacing z+d in equation 1.0 with $\frac{(z+d)d}{d+\eta}$ where η is the wave elevation (sum/linear superposition of the component wave elevations).A variation of this stretching approach is the delta stretching method proposed by Rodenbusch and Forristal (1986). It effectively replaces the elevation z with a transformed/stretched elevation $Z_S = \frac{(z+Ds)(\vartheta\,\eta+Ds)}{(\eta+Ds)-Ds}$ when $z>D_s$. It is usual to set $D_s = \frac{H_s}{2}$ and stretching parameter, $\vartheta=0.3$. Sutherland et al (1991) reports that Chakrabarti (1971) also presented another variation where $\sinh(k_j d)$ in equation 1.0 is replaced with $\sinh[k_j(d+\eta)]$ so that the stretching satisfies the dynamic boundary condition. Yet another approach different from the above stretching approaches is the extrapolation method. Here, horizontal particle velocity is calculated up to the MWL using linear theory but linearly extrapolated from there to the surface by assuming that the vertical partial derivative of velocity remains constant above MWL:

$$\boldsymbol{U = U_o + z\frac{\partial U_o}{\partial z}} \qquad \mathbf{2.35}$$

U_o is the velocity at MWL. Solving equation *2.35* in deep-water condition results in

$$\boldsymbol{U = \sum_j a_j \omega_j \left(1 + k_j z\right)\cos\theta_j} \qquad \mathbf{2.36}$$

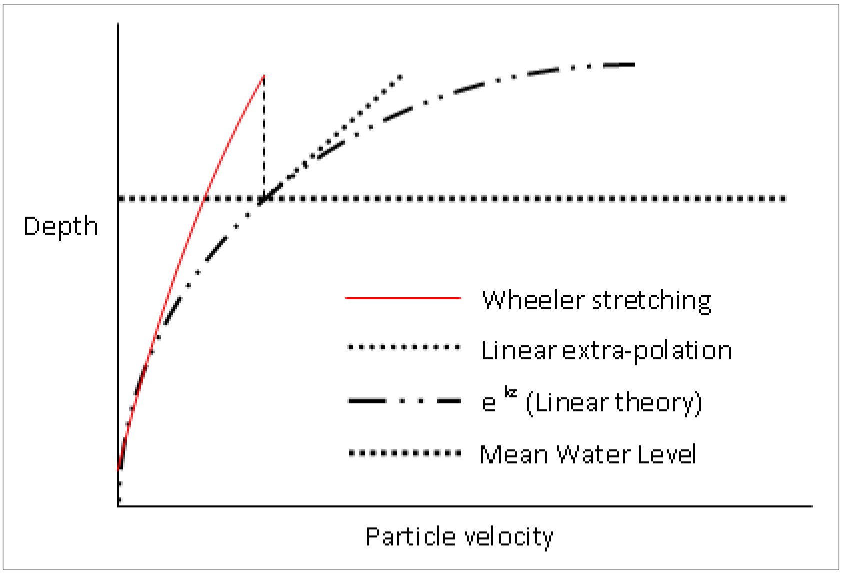

Figure 2.1: Schematic of various simplified kinematics methods

Useful as the above methods may be, they have been found to either under-predict or over-predict actual measurements with uncomfortable margins. It is therefore not surprising, when it is reported in Zhang et al (1996) that the above theoretical methods may result in a 50-100% difference in the predicted responses of a compliant tower structure. Grue et al (2004) presented a simple method which uses actual measured crest-heights and wave periods. The method proposes that the horizontal particle velocity profile under a steep crest is given by:

$$U(z) = U_o e^{k'z} \qquad 2.37$$

Where $U_o=\varepsilon'\sqrt{(g/k')}$. Here, k' and ε' are third-order wave-number and steepness respectively, based on period and crest height obtained from actual measurements. Stansberg et al (2006) however observed that although Grue's simple method works reasonably well in many cases above mean water level, it over-predicts horizontal velocities below. They therefore concluded that the second order irregular wave model (Dean and Sharmer, 1981 implemented by Stansberg et al, 2006 and Kim, 2008) works best at all levels under a steep crest in deep water. The second-order irregular wave approach in deep water is effectively a combination of linear extrapolation of MWL velocity above MWL and a second order difference-frequency contribution which is generally negative under energetic wave groups (Stansberg, 2006). The method developed by Zhang et al (1992, 1993a) takes this second-order wave-wave interaction into account. This therefore gives velocities that are less than strictly linear theory results and results obtained by linear-extrapolation above MWL. Taylor (1992) presented a similar method where velocities above MWL are linearly extrapolated from MWL and combined with a negative return current which is based on a simple two-wave interaction where short waves ride on the long wave components of the spectrum so that the amplitudes and wave-numbers of the short waves are modulated by the long waves. Unfortunately, a comparison of the method with physical measurement or results of other theoretical methods was not presented in the paper.

2.7.2 Laboratory Investigations

Sutherland et al (1991) reported that crest kinematics obtained by Charkrabati stretching were lower than those obtained by Wheeler stretching and that both methods gave results that were lower than their experimental results. They therefore favour linear extra-polation and have observed it to give results that are closer to their experiments. However, Grue et al (2004) in their investigation of very steep waves, noted that linear extra-polation is only useful for the range of wave-slope (local amplitude multiplied by local wave number) between 0.11 and 0.19. They concluded that although linear extrapolation is more useful than the other stretching methods, it still under predicts kinematics in very steep waves. It is obvious that the challenge now lies in the more non-linear cases (e.g very steep and asymmetric random waves).

This is corroborated by the experimental measurements of other investigators who considered steeper cases of extreme waves. Choi (2005) measured kinematics in the crest of regular, irregular and rogue waves. Applying the measured kinematics to Morison's equation, non-linear wave forces on a truncated slender cylinder were computed. These results were compared with those obtained from linear extrapolation, Wheeler stretching and a modified stretching method presented by Kim et al, 1997(cited in Choi, 2005) which essentially is a geometric modification of the stretching model to take into account, the asymmetries of the wave in predicting highly non-linear wave kinematics. Choi concluded that Wheeler stretching generally underestimates the actual wave kinematics, while linear extrapolation is very sensitive to the cut-off frequency of the wave spectrum. It was observed that the modified stretching method tends to predict the maximum value of wave kinematics above SWL well but is less accurate in predicting lower velocities. It is also obvious that horizontal particle velocities recorded by Choi were less than linear-extrapolation results and by extension linear theory results, even in the steepest case of a wave twice the significant wave-height.

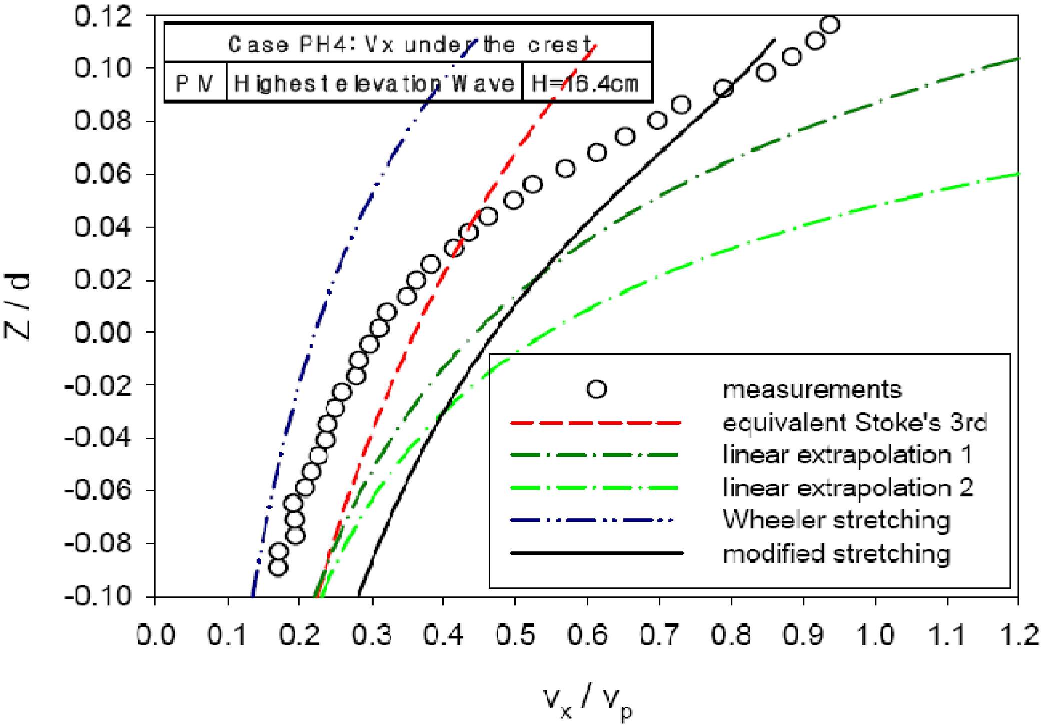

Figure 2.2: Horizontal Particle velocity under a rogue wave crest (Choi, 2005).

Kjeldsen (2000) also studied the kinematics of steep plunging waves in the laboratory, using the non-linear packet-focusing technique. Kinematics just up-wave of the onset of plunging is measured and compared with results from a superposition, a modified stretching and a Stokes third-order theory based model which Kjeldsen reports to best represent the velocity beneath the plunging breaker. Similarly, Baldock et al (1996) generated a very large transient wave group by focusing a large number of waves at one point in space and time. Measurements of the water surface elevation and the underlying kinematics were compared with both a linear wave theory and a second-order solution based on the sum of the wave-wave interactions identified by Longuet-Higgins & Stewart (1960). Their data showed that the focusing of wave components produces a highly nonlinear wave group in which water surface elevation and near-surface particle kinematics are significantly larger that those predicted by the linear sum of the wave components and much higher than predictions based on their second-order solution. This is at odds with Stansberg et al (2006) who showed that the measurements of Skjelbreia et al (1991) were much less than linear theory predictions and concluded that the second-order approach gives results that are closer to the measurement.

To get a wider view of these seemingly conflicting particle velocity results, they are grouped in table 2.1 as results that are less and results that are more than strictly linear theory results in the region above mean water level.

Table 2.1: Summary of some published crest horizontal particle velocity results
(A_o= extreme crest height, K_o= wave-number based on zero-crossing period about the extreme crest, d=water depth)

Ratio of measured velocity to linear theory prediction	**Authors/ Investigators**	**Measurement method**	**Wave generation method**	**Estimated A_oK_o (local steepness)**	**K_od (water depth)**
$\leq$ **1**	Skjelbreia (1991)	LDV	Random	0.395	2.456
$\leq$ **1**	Longridge et al (1996)	LDA	Random	0.208	3.269
$\leq$ **1**	Choi (2005)	PIV	Random / distortion	0.408	4.015
$\leq$ **1**	Clauss et al (2007)	LDV	Random/ optimization	0.331	2.685
≥ 1	Baldock et al (1996)	LDA	Focusing	0.335	3.122
≥ 1	Grue et al (2004)	Potential solver	Focusing	0.335	∞
$\leq$ **1** **≥ 1**	Present work	RANS solver	Focusing	0.326 (highest wave) 0.315 (steepest wave)	4.583 6.846

Curiously, there appears to be two distinct schools of published horizontal particle velocity results under extreme crests, which do not seem to depend on the method of velocity measurement, local-steepness of the extreme crest, water depth or method of generating the extreme event. Apart from the distinction according to particle velocity being higher or lower than linear theory prediction (in the region above mean water level), no definite trend is apparent and based on the above known particulars of the various experiments, the reason for the disparity is unclear.

2.7.3 Full-scale Investigations

It is pertinent to note that although each method developed in the above studies seem to give better results relative to stretching and extra-polation methods, their accuracy with respect to actual field measurements, needs to be verified. Therefore, Farmer (2002) conducted full-scale (Danish Sector of the North Sea) measurement of velocities within the crests of large steep waves. Observations in a storm of wind speed up to 17m/s led Farmer to conclude that at the ocean surface, the downwind velocity in the crest of large waves substantially exceeded that predicted by the second-order Stokes model. This is consistent with the findings of Baldock et al(1996). However, Farmer's conclusion is at odds with Stansberg et al(2006) who concluded that the second-order approach gives results that are closer to experiment while noting that the quasi-empirical method of Grue et al (2004) over-estimated velocities in the region below MWL because they did not take the second order effect of difference frequency contribution/set down into account. Grue et al (2004) have argued that prior to their work in 2004, most work in the area has not gone beyond moderately steep waves so that despite numerous studies on the subject, proper knowledge of kinematics of very steep irregular ocean waves is still lacking. By defining a, as the crest elevation of the extreme wave, and k, the local wave-number based on a 3rd order dispersion-relationship with trough-to-trough period about the extreme event, Grue et al (2004) concluded that in the cases of very steep waves generated by focusing and having ak values above 0.3 (Longuet-Higgins and Cokelet, 1978 gives ak=0.38 at overturning, for a regular-wave), the exponential profile was the best fit with a non-dimensionalized version of their experiments. This is consistent with the findings of Baldock et al (1996) that the focusing of wave components produces a highly non-linear wave group in which water surface elevation and near-surface particle kinematics are significantly larger than those predicted by the linear sum of the wave components, as done in the classical linear theory and much larger than velocities obtained in their second-order solution.

2.7.4 Wave-Breaking.

In deep water, the common geometric breaking criterion for regular waves (Mitchel, 1893) is $\frac{H}{L} \geq \frac{1}{7}$, where H and L are wave height and length respectively. For irregular waves, this criterion becomes difficult to apply since there is no obvious H or L. As an alternative, Xu and Barltrop (2005) used the concept of a “significant (sea-state) steepness” given as the ratio of significant wave-heigth to zero-crossing wave-length, $\frac{H_S}{L_z}$ with $L_z = \frac{g(T_z)^2}{2\pi}$ and T_z= zero-crossing period of the sea-state. The authors found that the most probable highest limiting wave occurred in a sea-state with $\frac{H_S}{L_z} = \frac{1}{13}$. Using H$_{\max}$=1.86$H_s$, it is found that $\frac{H}{L} = \frac{1.86Hs}{13} = \frac{1}{6.99}$, which is almost identical to the value for the limiting stokes wave. In the present work, another notion of wave steepness, ak is adopted and for the sake of distinction, it is referred to as “local steepness”. Here, a represents the crest elevation of the extreme wave and k defined as the local wave-number based on a linear dispersion-relationship with zero-crossing period about the extreme event.

Thus in total, two different notions of steepness are used in the present work:

1. A local-steepness based on crest height and zero-crossing period in the vicinity of the crest.
2. A sea-state steepness defined as the ratio of the significant wave-height of the sea-state to the zero-crossing wave-length based on a linear-dispersion relationship with the zero-crossing period of the sea-state.

3 Viscous Flow Simulations: Extreme wave kinematics.

It has been usual to study kinematics of extreme waves using physical experiments. Unfortunately, several conflicting experimental measurements have been presented (see eg Stansberg et al, 2002 Vs Grue et al 2002 and table 2.1). This discrepancy in the conclusions of different authors about maximum particle kinematics at higher wave steepness's (the present work started out with the hypothesis that viscous flow would apply in such extreme conditions) confirms the difficulty inherent in obtaining reliable theoretical and experimental results at the top of extreme wave crests where incidentally, maximum velocities are expected. Reliable theoretical methods are therefore desirable for obtaining more precise kinematics in the crest of extreme waves and several methods have been proposed.

Yan and Ma (2008) have noted that with the exception of viscous-flow and a few fully non-linear potential flow methods, most of these methods are unable to cope with very extreme surface deformations. The modelling of extreme waves using viscous flow-based methods have recently come into focus (see e.g Westphalen et al, 2008; Clauss et al, 2006, 2007 and 2008; Kristiansen et al, 2005; Zhaowei et al, 2005; Kleefsman, 2004; Nielsen and Mayer, 2004). In the present study, a comparison of potential and viscous flow methods is not intended and one is not recommended over the other. Instead, a viscous flow method is used since it is also sought in the next chapter to investigate the effect of viscosity and surface-tension on breaking waves in the laboratory.

The modelling of viscous flow is based on the solution of the Navier-Stokes equations which were almost impossible to solve without computers thereby necessitating the assumption of potential flow. With the advent of considerable computer power, viscous flow solution of the Navier-Stoke’s equation is now done in a variety of ways which can be broadly categorized in 3:

1. Direct Numerical Simulation (DNS). The equations are solved without any modifications but this requires a very large amount of computer resources.
2. Large Eddy Simulation (LES). The major dilemma in solving the equations lies in the large difference between the scale of the smallest and largest turbulent eddies and the impractically large amount of computer resources required for handling both scales simultaneously. The LES therefore computes the larger eddies and averages the small scale eddies by assuming them to be 'self similar' and independent of flow geometry.
3. Reynolds Averaged Navier-Stokes (RANS). In order to make the equations more practical to solve, the turbulent eddies are removed and the equations solved for the mean flow. This is done by averaging the equations over a time somewhere between the largest and smallest turbulent scales (Larsson and Raven, 2004) and the resulting equations are thus termed RANS equations.

The LES and RANS techniques are implemented in commercial codes like FLUENT, CFX, STAR CCM and Flow3d. In the present work, the RANS technique implemented in Fluent is used.

3.1 RANS Turbulence Modelling

Due to averaging of the turbulent fluctuations in the velocity and pressure terms of the Navier-Stokes equation when using the RANS approach, the system has more variables than equations resulting in a problem of “closure”. This is resolved by introducing so called turbulence models which simulate turbulence by approximations and empirical tuning. The subject of turbulence is a complex field and research is still on-going. Therefore, a brief introduction to the main ideas in the simplest models should suffice for the purpose of the present work. To this effect, the main concepts of turbulence modelling in RANS are presented in Appendix A5.

3.2 RANS Wave-tanks

Zhaowei et al (2006) studied the incidence of green-water on an FPSO (Floating Production Storage and Offloading vessel) using the commercial CFD (Computational Fluid Dynamics) code- FLUENT, to solve the associated continuity and Navier-Stokes equations. Regular waves were generated by the addition of source-terms to the momentum equations and the movement of the free-surface was captured using the VOF (volume-of-fluid) method. Since they were only concerned with “green-water” they did not present any results of kinematics. Nielsen & Mayer

(2004) also modelled the “green-water” experiment of Greco et al (2001) in a 2-d NWT using the incompressible Navier-Stokes solver- NS3. Boundary conditions similar to those of Zhaowei et al (2006) were used, except that the “wall” at the beginning of the tank was replaced with a flap-type wave-maker so that rather than using source terms, regular waves were generated by the motion of the wave-maker flap. In Kristiansen et al (2005), 3-d regular waves were generated by imposing velocities according to linear theory, at the beginning of the tank (inlet) using linear extrapolation of mean water level velocities to the free-surface and the waves driven by gravity. At the bottom of the tank, a “no-slip” boundary condition was prescribed while at the far end and on top of the tank, a radiation and atmospheric pressure conditions were respectively prescribed. Their tank was implemented in the commercial CFD code – Flow3d which applies FVM (Finite Volume Method) to solve 3-d RANS equations with the free-surface being captured by the VOF method. Clauss et al (2006) implemented a wave tank in FLUENT, CFX and COMET viscous flow solvers. An RNG K-ε turbulence model was used while the geometry of the free-surface was captured with the VOF (Volume of Fluid) method. Similar boundary conditions as those of Zhaowei et al (2006) were used. Regular and irregular waves were generated by impressing transient velocities on the inlet and these velocities were defined by the time derivative of the motion of a wave-board measured in a physical wave-tank.

In the case of Kleefsman (2005), the focus was on development of a robust RANS solver (COMFLOW) which unlike the general purpose CFD solvers was specially aimed at simulating waves that result in loading on an offshore structure. A part of the customization was the implementation of a special VOF method using a local height function to ensure almost exact mass conservation and consequently better prediction of the wave elevation than general purpose RANS codes. Like the general purpose solvers, Kleefsman's solver relies on an external program to prescribe the waves. It was suggested that waves could be generated by either prescribing the motion of the numerical wave-board (near end of tank) according to the measured motion of a wave-maker as done by Clauss et al(2006) or prescribing velocities at the inlet with velocities calculated externally. The work of Kleefsman (2005) culminated in using COMFLOW to simulate "green-water" and wave-impact events. Since wave-impact and green-water loads were obtained directly in COMFLOW, wave kinematics were not needed and were consequently not investigated. Similarly, Zhaowei et al (2006) and Nielsen and Mayer (2004) whose works were based on regular waves were interested in green-water loading and did not investigate wave kinematics. In the case of irregular ocean waves, calculation and simulation have been a major challenge. Therefore the work of Clauss et al (2006 and 2007) which was aimed at reproducing specific real-life extreme waves like the Yura and Draupner waves, was very welcome. More recently, Westphalen et al (2008) presented results of water surface elevation of the traditional extreme wave (focused crest new-wave) using the viscous flow solvers – CFX and STAR CCM.

3.3 Focus on the alternative extreme wave

Apparently, many viscous flow investigations of the traditional extreme wave (most probable highest wave) have been conducted. In the present study, the focus is on understanding the loads induced by the alternative extreme wave in terms of the underlying kinematics and how it differs from those of the traditional new-wave (most probable highest wave). Swan et al, (2000) had earlier modelled a simple version of this alternative extreme wave where component wave slopes rather than crests are focused and it was concluded that such a wave resulted in the more extreme particle accelerations. However their input spectrum was narrow banded relative to more practical spectra like the JONSWAP, PM and Bretschneider spectra. Also, the same spectral amplitudes were used in generating the steepest as well as the highest waves and therefore, statistics were not taken into account in order to ensure that the probability of occurrence remained equivalent. As a result, their steepest and highest wave cases are not comparable in the context of a realistic random sea-state. The NewWave theory shows that this is not so in a realistic random wave spectrum rather the maximization of slope (front-steepness) negatively compensates for height and vice versa. The implication is that relative to the most probable highest wave, the most probable steepest wave will be lower and much lower than the case where statistics are not considered as in Swan, Bashir and Gudmestad (2000). Therefore in a situation where the most probable steepest wave is being compared with the most probable highest wave, the question arises as to which of the two extremes result in higher particle kinematics in a standard ocean wave spectrum. The present work includes an attempt to answer this question.

Based on laboratory measurements of impact forces on an FPSO model, Xu (2006) had earlier concluded that the most probable highest wave in a sea-state did not necessarily give the highest impact load. Beyond measuring exerted forces, the nature of the underlying wave kinematics need to be understood in order to develop a good theoretical understanding of the problem. Indeed, Stansberg and Karlsen (2001) had argued that as a result, kinematics in extreme waves needed to be further investigated. The present work is therefore concentrated on understanding the induced wave-loads in terms of the particle kinematics of the alternate extreme waves.

For the purpose of this study, the traditional "new-wave" is simply referred to as the *"highest wave"* while the alternative extreme wave which represents the steepest wave that is most likely to occur (ignoring breaking) is also simply referred to as the *"steepest wave"*. The "highest wave" and "steepest wave" are obtained by setting $\propto = 0$ and $\propto = 1$, respectively in equation *2.27.* Based on the alternative definition of "extreme" in terms of wave-slope, an alternative understanding of wave steepness which defines steepness as the slope of a wave-front is assumed through-out this work rather than the traditional definition of wave-height to wave-length which does not properly account for the asymmetry inherent in extreme waves. This alternative extreme has not been given much consideration probably because it implies a relatively lower crest height in a random wave spectrum.

3.4 Wave Generation In Numerical Wave Tank

Since wave-maker motions were not recorded in the physical experiment, velocities according to a suitable wave theory were prescribed at the inlet, in line with the suggestion of Kleefman (2005). The extended version of the new-wave theory described in section 2.6.2.2 is used to simulate the "most probable extreme wave" and by coupling the resulting velocities with the predicted height of water at the inlet, realistic waves were generated.

3.5 The Present Numerical Wave-tank

The present numerical wave tank is implemented in the RANS code – Fluent. Since Fluent is a commercial and widely validated code, it is superfluous to go into the details of how it works. Therefore, only the salient features associated with setting-up a general CFD simulation are highlighted.

3.5.1 Viscous model

There is a natural inclination to simulating wave propagation as a laminar flow. This also applies to the present study where interest is skewed towards the flow behaviour up to when the wave is just breaking rather than the post-breaking phase where turbulence is then evidently significant. However, it is also desirable to check whether the effect of turbulence in such (near)breaking conditions are indeed negligible, in the context of extreme wave-loading (as indicated by extreme particle kinematics before overturning). This check has been achieved by comparing horizontal particle velocity results obtained (at full-scale surface-tension) with a turbulence model (standard k-ε) and without a turbulence model (viscous laminar) in a wave that is just about over-turning (vertical surface). The result is shown in figure 3.1.

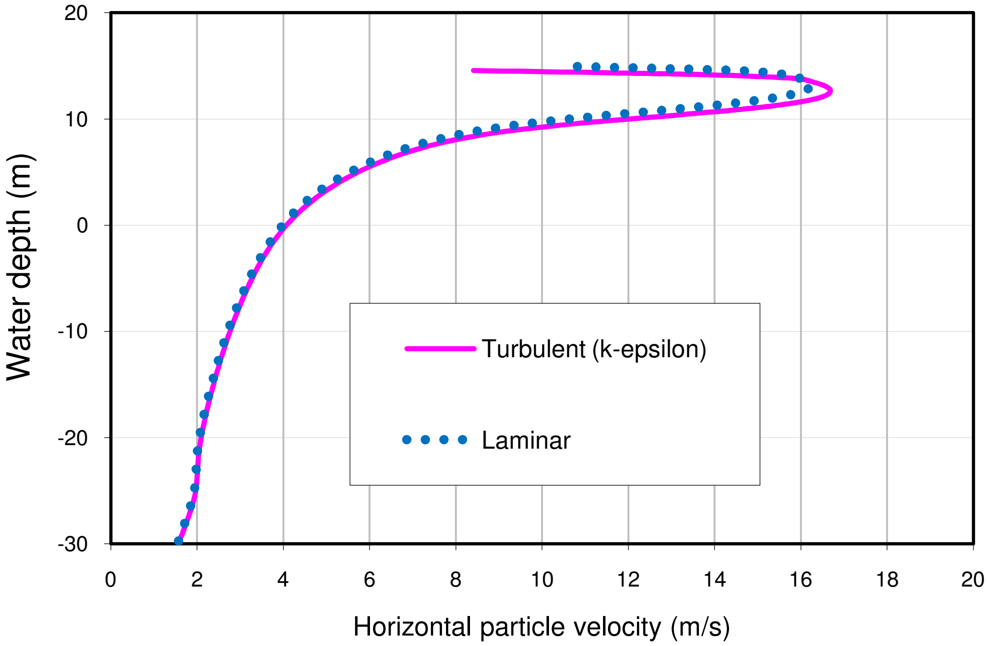

Figure 3.1: Effect of turbulence modelling on kinematics (Random extreme: H_s =17.67m , T_z=13.4s, JONSWAP peakedness parameter=2).

Notice that unlike in linear theory where maximum velocity occurs at the free surface, the velocity in the just-breaking wave shown in figure 3.1 is highest just below the crest top. This is understandable since the wave is just breaking and represents the initial stage of spout formation evidenced in the very steep crest shown in figure 3.2.

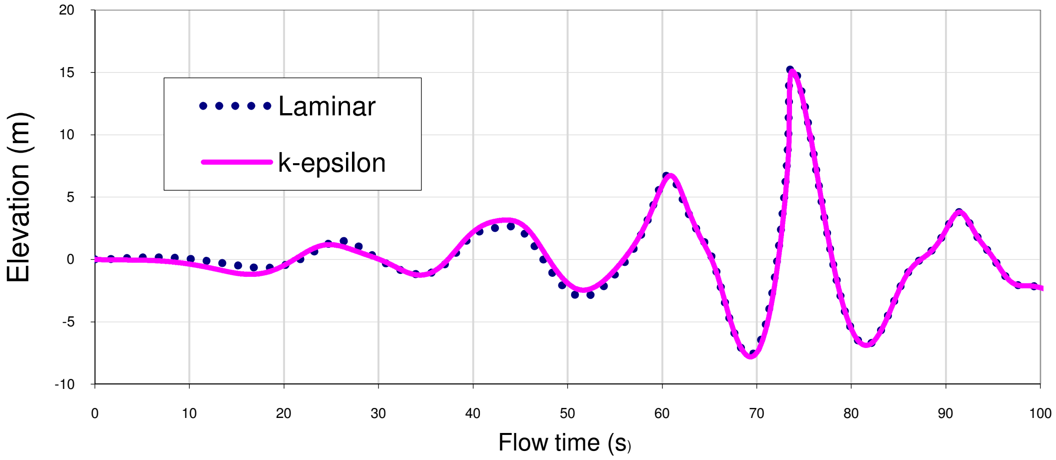

Figure 3.2: Effect of turbulence modelling on surface elevation (Random extreme: H_s =17.67m , T_z=13.4s, **JONSWAP peakedness parameter=2).**

Apparently, the results are the same except at the crest-top where the difference is also very small. This shows that in the context of maximum full-scale wave-loading, horizontal particle velocities are not very much affected by turbulence i.e turbulence is negligible in the context. This is consistent with conventional expectation that turbulence only becomes significant in the post-breaking/overturning phase of wave propagation which phase is not of immediate interest in the context of maximum wave-loads. As a result, the waves investigated are simulated as viscous laminar flows.

Curiously, the observation of very little turbulence (at least in the sense of a k-epsilon turbulence model) in the crest of the breaking wave gives rise to the question of how viscosity affects the dynamics of such extreme crests. An attempt is made to answer this question by comparing the above results (viscous flow) with results of inviscid-flow simulation (Euler equations).

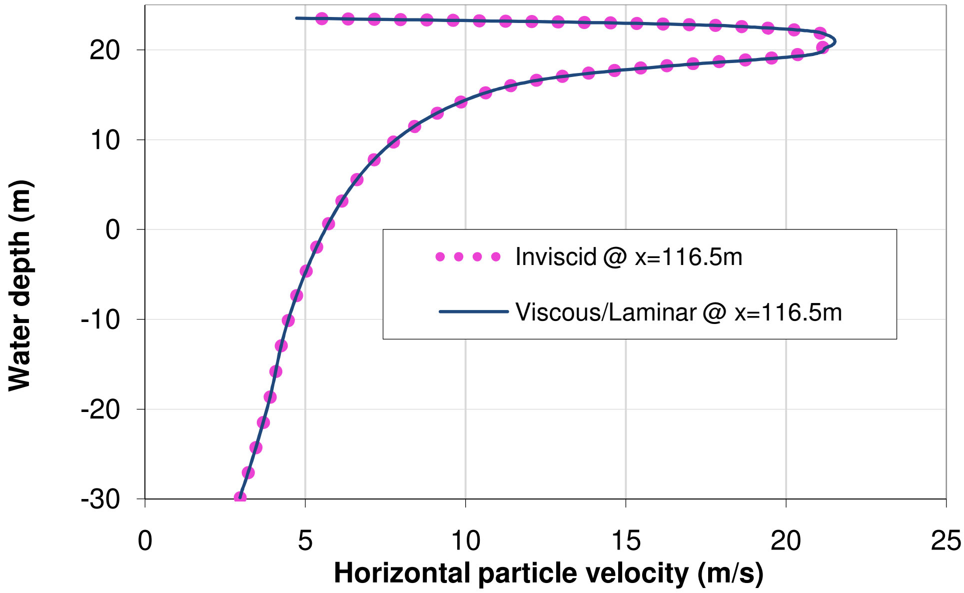

Figure 3.3: Effect of viscosity on kinematics (Traditional extreme: H_s =21.56m , T_z=13.4s, JONSWAP peakedness parameter=2).

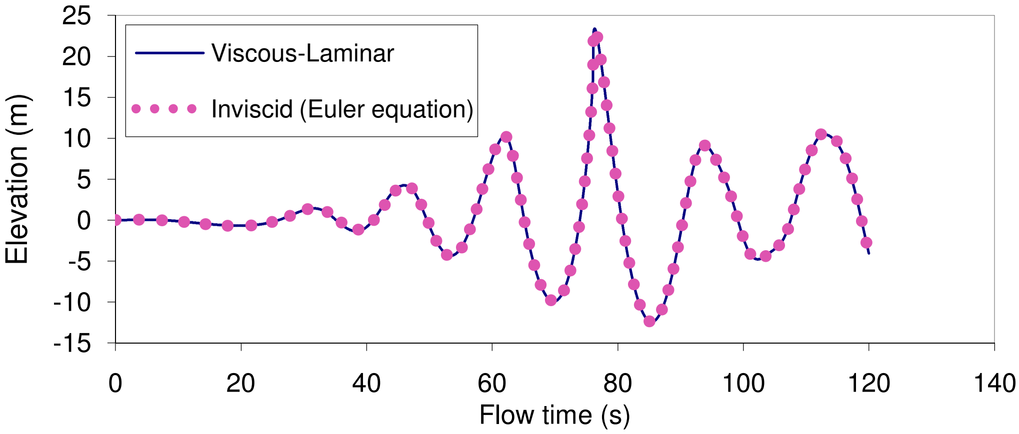

Figure 3.4: Effect of viscosity on surface elevation (Traditional extreme: H_s =21.56m , T_z=13.4s, JONSWAP peakedness parameter=2).

It is interesting to see that there is no significant difference in the results even when viscosity is neglected. This reinforces the earlier observation that turbulence is indeed negligible in this situation and disproves the viscous flow hypothesis adopted at the beginning of this Chapter.

3.5.2 Grid

The mesh is a two dimensional structured grid, 360m high and 468m long and consists of a very fine region around the mean water level and very coarse regions far away from the mean water level (see figure 3.5).

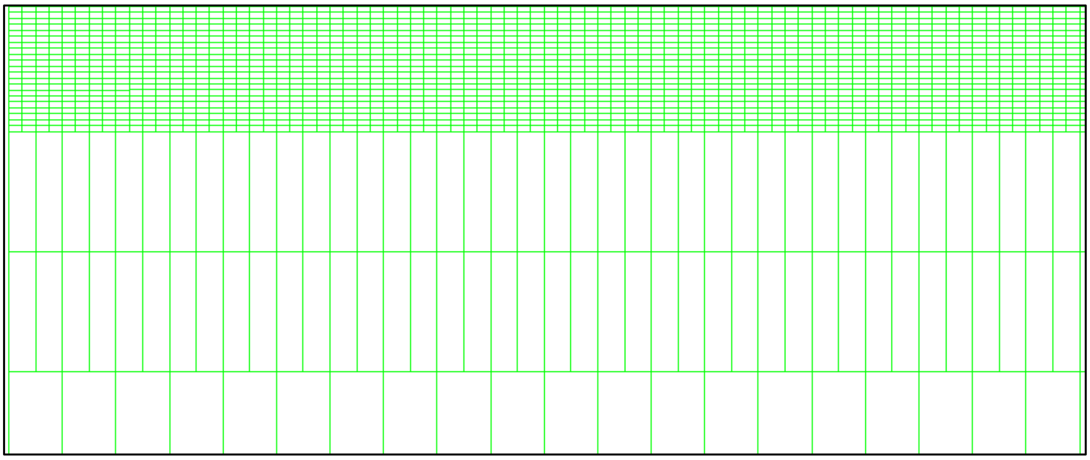

Figure 3.5: **Close-up view of the mesh around the free-surface.**

Cells in the very fine region are 0.66% (19.75cm) of the extreme wave-height and is slightly finer than the 0.91% recommended for grid-independence (Westphalen et al 2007 and 2008).Water depth is kept at 300m to generally represent deep water (dominant wavelength=187m) and the length of the numerical tank is such that reflected waves do not reach the target position until well after the extreme event has occurred (target time). General sketch of the numerical tank is shown in figure 3.6.

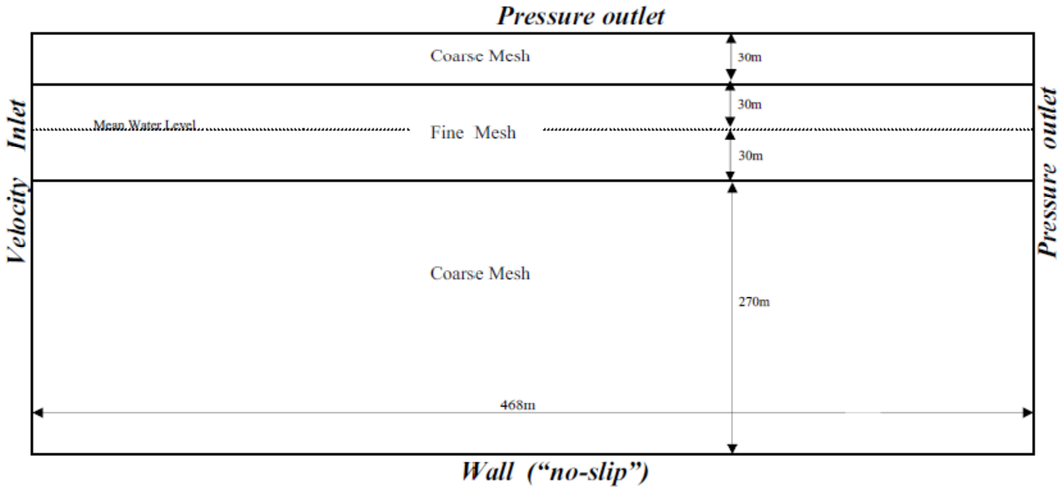

Figure 3.6: **Numerical wave tank.**

The wave is simulated using a pressure based segregated unsteady solver with times steps of 0.01s. Laminar flow and a water viscosity of 0.001003 kg/m-s is assumed. The momentum and VOF (Volume-of-Fluid) equations are discretized with the 3rd Order MUSCL (Monotone Upstream-Centered Schemes for Conservation Laws) and Modified HRIC (high resolution interface capturing) schemes respectively. The HRIC scheme is essentially a non-linear blend of upwind and downwind differencing while the 3rd order MUSCL is essentially an optimum combination of central differencing and second-order upwinding. Boundary conditions applied are shown in figure 3.6 above.

The wave is generated by impressing a transient velocity (linear wave theory) profile and non-linear water surface elevation (Walker et al, 2005) defined to include the modification to the NewWave theory discussed earlier, on the inlet.

The wave components are phased in such a manner that they are co-phased (focused) at a so-called "target-position" downstream of the inlet. These inlet and outlet conditions are implemented in a "user defined function (UDF)" which is an external C code (see Appendix A6 for details) added-on to FLUENT and specifies the particle velocities and water level at the inlet as well as hydrostatic pressure at the outlet where water level is kept at the mean level. The linear theory velocity without stretching (e^{kz}) is used to specify particle velocities at the inlet since several authors (e.g Baldock et al, 1996; Grue et al, 2004) have shown in unidirectional focused waves that while linear theory will under-predict crest elevation more than the higher order representations, linear theory particle velocities are closer to measurements than the second order representation. It is therefore reasonable to initialize the simulation with linear particle velocities considering the following:

1) In wave groups, the condition should be more linear at the inlet than at the position of the extreme event
2) The amount of computational resources required to obtain third and higher order velocities would be relatively high.

3.5.3 Grid dependence

In this section, it is attempted to determine the number of cells necessary to obtain good results of water surface elevation. The simulations are performed using the conventional NewWave in a sea-state with H_s=17.67m and T_z=13.4s (dominant wavelength=187m), in water depth of 300m.

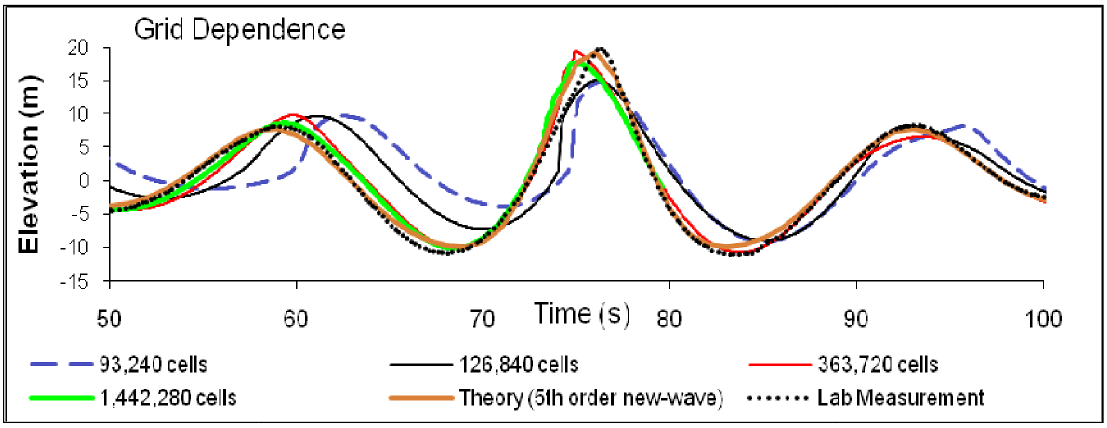

Figure 3.7: Shape of the extreme wave with different grid fineness.

It can be seen that there is very little improvement in the accuracy of results beyond 363,720 cells. Besides, the surface elevation at the extreme event obtained using this grid seems to be in slightly better agreement with theory and measurement. Although the difference between the two finer grids is quite considerable and it may be that some grid size in-between them may be the optimum, it is important to recognize that 363,720 cells already implies that very large computational resources will be required and it is doubtful if the marginal improvement in results obtained by further grid refinement can justify the further, extremely large, computational resource required. The grid with 363,720 cells is therefore chosen to be the optimum for the present study. In the very fine region of the mesh around the mean water level, the chosen grid has a cell size of 0.1975m which is 0.66% of the extreme wave-height and is slightly finer than the 0.91% recommended for grid-independence (Westphalen et al 2007 and 2008).

3.5.4 Numerical Dissipation.

The discretization of the Navier-Stokes equations requires the interpolation of cell-face values from cell-centre values, for the calculation of the convective terms. Using an upwind scheme, the cell-face value is essentially the cell-centre value of the adjacent upstream cell. In a considerably convective flow, the convective gradient is such that cell-face values may be significantly different from the values in the centre of the upstream cell thereby resulting in a small discretization error which can become considerable over several cells. This error is treated by a diffusive term in the transport equation which has the effect of an artificial viscosity given by $uh/2$ (u =velocity and h = cell size), adding to the physical viscosity μ/ρ in the various cells. This artificial viscosity can be several orders of magnitude larger than the physical viscosity and over several cells, can result in considerable damping of the free surface. This has considerable implication in the conservation of energy of waves propagating over several wave-lengths. In the central difference scheme, this effect is less since the cell-face value is essentially calculated as the average of the adjoining cell-centre values and gives a more accurate result (Fluent Inc., 2006).

The discretization method adopted in the present study is an optimal blend of the central difference and second order upwind scheme. It is optimal in the sense that central differencing is used where upwinding errors can be considerable and second order upwinding used where the resulting discretization errors are negligible. It is thus expected that numerical damping of the waves will be very small. Moreover, the grid used is very fine and the domain is less than twice the dominant wave-length whereas the effect of numerical diffusion is only visible over several wave-periods and with increasing cell size (Fluent Inc., 2006). For example, using a first order upwind scheme, Kleefsman (2005) found that there was no appreciable dissipation even after 4 wave-periods but noticed a decrease in wave-height of 22% and 28% after propagating over 14 and 20 wave-lengths respectively.

3.6 Comparison With Physical and Analytical Results.

In order to check the usefulness of the Numerical wave tank, its results are compared with physical laboratory measurements (Xu, 2006) and the 5th order new-wave theory (Walker et al, 2005) predictions of the most probable highest and steepest waves for a JONSWAP spectrum (Significant Wave-height =18.73m and Zero-crossing period=13.4s). The Physical measurements were made at a scale of 1:80 in a tank with 2.3m water depth, 76m length and 4.6m width which is shown in figure 3.8 below.

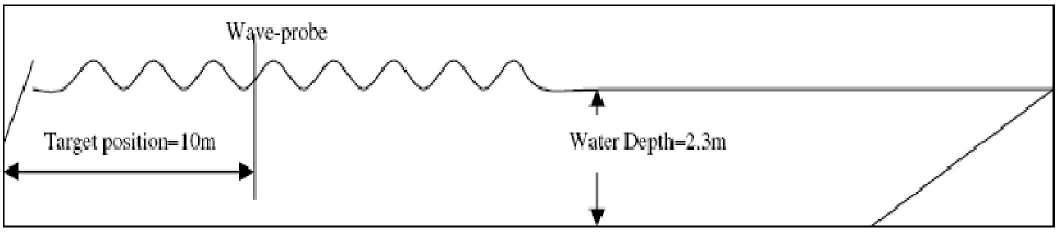

Figure 3.8: **Physical wave tank.**

Using a flap type wave-maker, waves were generated according to linear theory with phases in such a way that they focus at a wave probe placed 10m (800m full-scale) downstream of the wave-maker. Although there was a beach, avoidance of reflections mainly relied on the tank being long enough for measurement at the wave-probe to be completed before reflections arrived. Only water surface elevation was measured in the physical experiment. Figures 3.9 and 3.10 compare the present numerical results with physical measurements and non-linear new-wave (Walker et al, 2005) results of the highest and steepest wave elevations measured at the "target position".

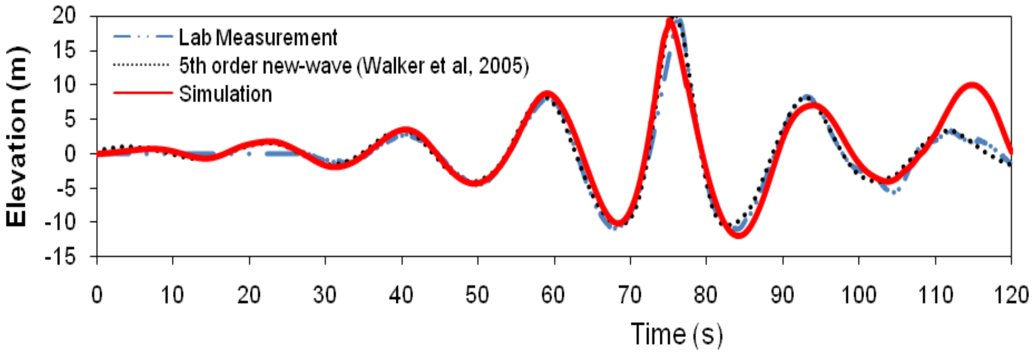

Figure 3.9: **Water surface elevation at designed focus position for the most probable highest wave (traditional "new-wave") : H_s=18.73m, T_z=13.4s, JONSWAP peakedness parameter=2.**

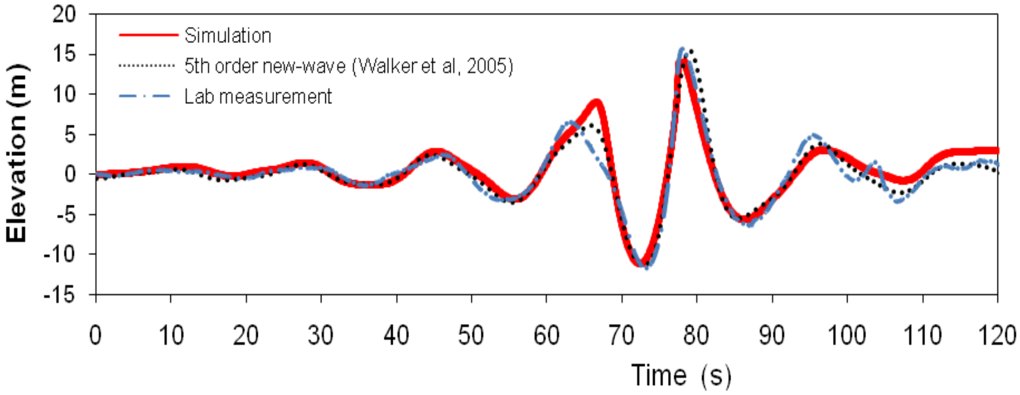

Figure 3.10: **Water surface elevation at designed focus position for the most probable steepest wave (alternative extreme) : H_s=18.73m, T_z=13.4s, JONSWAP peakedness parameter=2.**

3.7 Extreme Particle Kinematics

Both the highest and steepest waves of the above sea-state (H_s=18.73m and T_z=13.4s) were found to break during the simulation despite the maximum crest of the steepest wave being about 25% lower. The significant wave-height was so high that the most probable steepest wave broke before focusing and was sufficiently high for even the most probable highest wave to break. But what happens in a slightly lower sea-state where the most probable steepest wave does not break before focusing? To answer this, the significant wave-height is reduced to 17.67m keeping the zero-crossing period constant at 13.4s. In this slightly lower sea-state, the most probable steepest wave broke well after the "target position" but the highest wave did not break throughout the simulation. It was also found that the maximum particle kinematics in the most probable highest wave did not occur at the designed "target position" but occurred at a point further downstream which is a well known non-linear effect (Baldock et al, 1996; Rainey, 2006; Gibson and Swan, 2006 etc). Therefore, maximum kinematics in the steepest wave is taken at a point 253m downstream of the inlet where the water surface is virtually vertical, on the verge of forming a spout and is shown in figure 3.11 below.

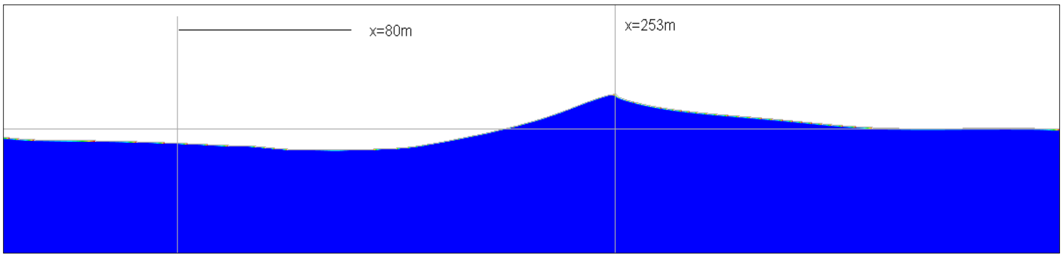

Figure 3.11: **Water surface of the steepest wave at the verge of breaking (H_s=17.67m, T_z=13.4s, JONSWAP peakedness parameter=2) Crest moving from left to right.**

For the highest wave maximum kinematics, the region in time and space where maximum surface elevation occurs is carefully examined for maximum dynamic pressure and horizontal particle velocity. This was found to occur slightly after the point of maximum surface elevation 171m downstream of the wave-maker as shown in figure 3.12.

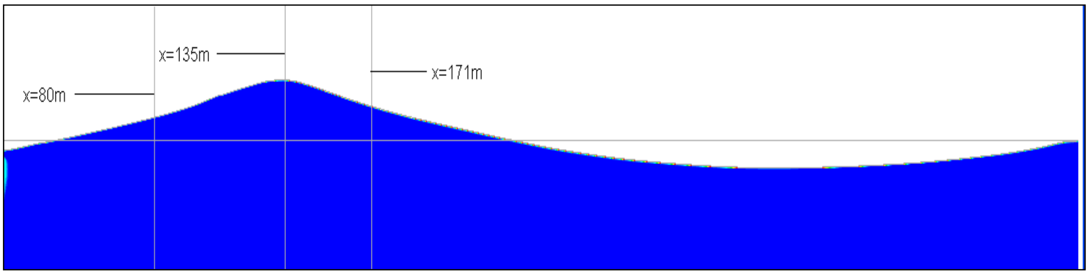

Figure 3.12: **Water surface of the highest wave at the instant of maximum surface elevation (H_s=17.67m, T_z=13.4s, JONSWAP peakedness parameter=2) Crest moving from left to right.**

3.7.1 Comparison of observed steepest wave and highest wave particle kinematics.

Since maximum horizontal particle velocity and vertical particle acceleration are expected under the maximum crest, the steepest and highest wave maximum values were measured when the maximum crest arrives at x=253m and x=135m respectively. Similarly, maximum horizontal particle acceleration and vertical particle velocity was measured at the zero-up crossing just before the maximum crest occurs at x=171m and x=135m (at which points the wave attained their maximum heights) for the steepest and highest wave (H_s=17.67, T_z=13.4) respectively.

3.7.1.1 Maximum Horizontal Velocity

Figure 3.13 shows the variation of horizontal particle velocity along the water column at the points where the steepest wave is steepest (x=253m) and the highest wave is highest (x=135m). To provide context, the celerities (obtained by determining the distance travelled by the crest in the last time-step leading up to the extreme event) of the respective extreme waves are also presented.

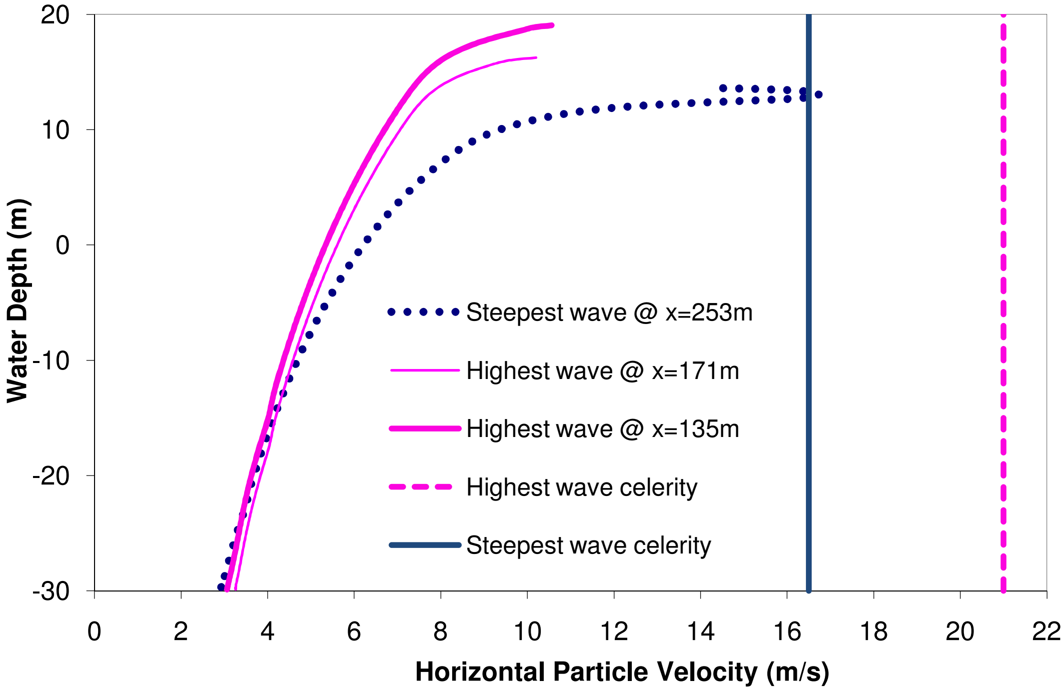

Figure 3.13: **Maximum Horizontal Particle Velocity under crest (H_s=17.67m, T_z=13.4s, JONSWAP peakedness parameter=2).**

Near the free surface, velocity is about 43% higher in the steepest wave compared to the highest wave. It can also be seen that the crest velocity of the steepest wave is very close to its celerity which is however, smaller than that of the highest wave. It is thus not surprising that while the highest wave is far from breaking; the steepest wave is just on the verge of overturning. It is therefore apparent that the breaking mechanism in the steepest wave is a combination of increasing particle velocity and decreasing celerity which results from the steepest wave being biased to the higher frequency components of the spectrum. In the region far below mean water level where kinematics is dominated by low-frequencies, horizontal particle velocity in the steepest wave is slightly less than in the highest wave. However in the region above mean water level where kinematics is dominated by the high frequency components, the reverse is the case. This is evident in figure 3.14 where the front of the steepest wave which is just on the verge of breaking is indeed very much steeper than that of the highest wave although not as high.

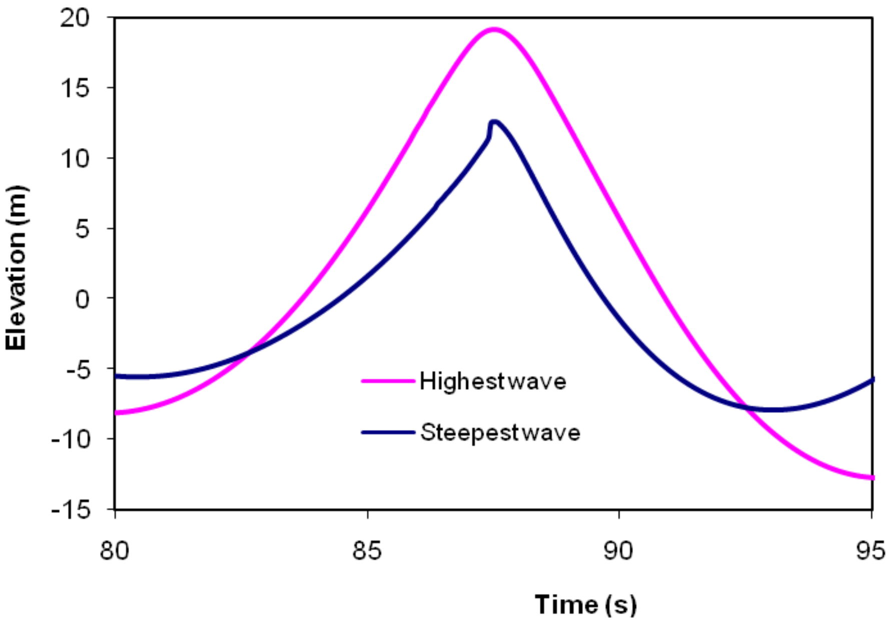

Figure 3.14: **Extreme water surface elevation: H_s=17.67m, T_z=13.4s, JONSWAP peakedness parameter=2 (time shifted for extreme to coincide).**

3.7.1.2 Maximum Dynamic Pressure

Although the general behaviour of the dynamic pressure ($\frac{1}{2}\rho v^2$) under crest was found to correspond with maximum particle velocity (see figure 3.15) in the steepest wave, this was not so in the highest wave. Maximum dynamic pressure in the highest wave was found to occur at a position 36m (13% of the zero-crossing wave-length) downstream of the point where maximum crest elevation and maximum horizontal particle velocity occurred. This is surprising since in theory, they are expected to occur at the same point (in theory, dynamic pressure under crest is directly proportional to the square of the horizontal particle velocity under the crest where vertical velocity is negligible). As a result, horizontal velocity at x=135m and dynamic pressure at x=171m are shown in figures 3.13 and 3.15 where both quantities are respectively found to be maximum.

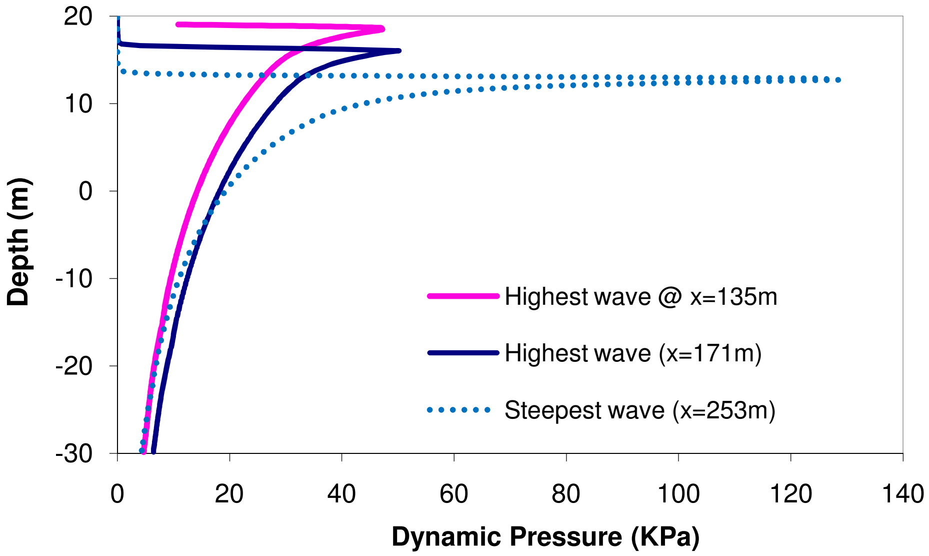

Figure 3.15: **Maximum dynamic pressure under crest (H_s=17.67m, T_z=13.4s, JONSWAP peakedness parameter=2).**

3.7.1.3 Maximum Vertical acceleration

A very interesting behaviour noticed in the vertical particle acceleration (figure 3.16) is that the total vertical acceleration reaches a maximum of -0.41g just below the free surface but drops to almost zero at the free-surface. This seems to contradict linear theory (where maximum kinematics is expected at the free-surface) but corroborates the numerical results of Bateman et al (2003) and the analytical inference of Longuet-Higgins (1986) that in very steep waves, the vertical acceleration beneath the crest must increase with depth at first, reaching a maximum below the free-surface before decreasing exponentially to negligible values at great depth.

Similar to maximum horizontal velocity, steepest wave vertical accelerations are lower below but higher above MWL and reach a maximum of -0.41g which is 37% higher than the comparable maximum in the highest wave (figure 3.16).

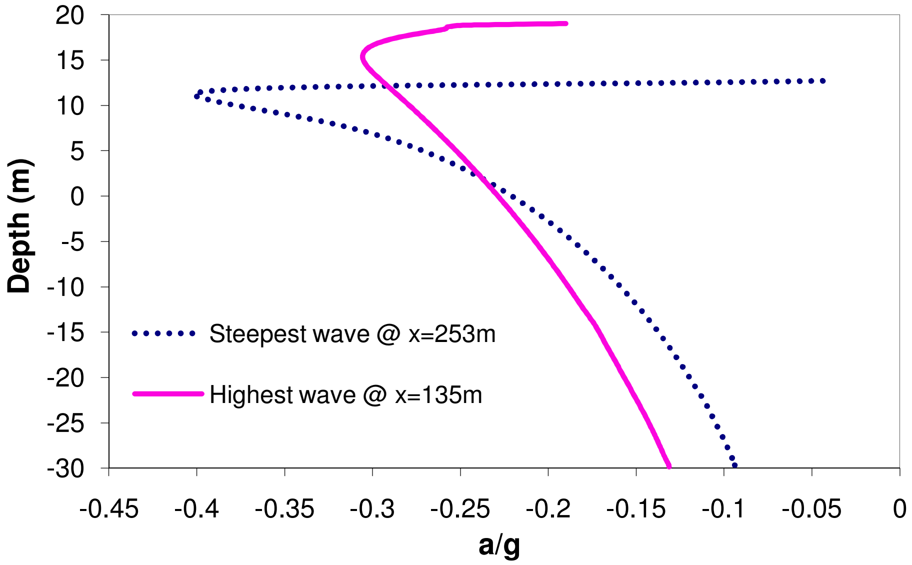

Figure 3.16: **Maximum vertical particle acceleration non-dimensionalized with g (H_s=17.67m, T_z=13.4s, JONSWAP peakedness parameter=2**

This observed maximum vertical acceleration is the same as the experimental value reported by Griffin et al (1988) and very close to the value of -0.4g reported by Ochi and Tsai, 1983; Srokosz, 1985 and Longuet-Higgins,1986. The implication is that the steepest wave can at the point of breaking, result in a vertical inertial force (on a fixed structure) that is generally higher than that resulting from the equivalent highest wave in the sea-state simulated here (H_s=17.67m and T_Z=13.4s) despite not being as high as the highest wave.

Curiously, the local/temporal ($\frac{\partial}{\partial t}$) and convective ($u\frac{\partial}{\partial x} + v\frac{\partial}{\partial y}$) parts of the vertical particle acceleration in the steepest as well as the highest wave were found to be opposite in sign and of the same order of magnitude so that neglect of the convective part could have resulted in over-estimation of the maximum steepest wave acceleration by up to 3 times. This is consistent with the observation (in the context of the traditional extreme wave that was not breaking) of Jensen et al (2006) who argued that as a result, the convective part of acceleration in extreme waves should not be neglected as is conveniently done in routine analysis. In the case investigated, maximum convective and local (temporal) acceleration in the steepest wave which was on the verge of breaking was 0.825g and -1.204g respectively and is shown in figure 3.17. Note that these maxima occurred at different water depths.

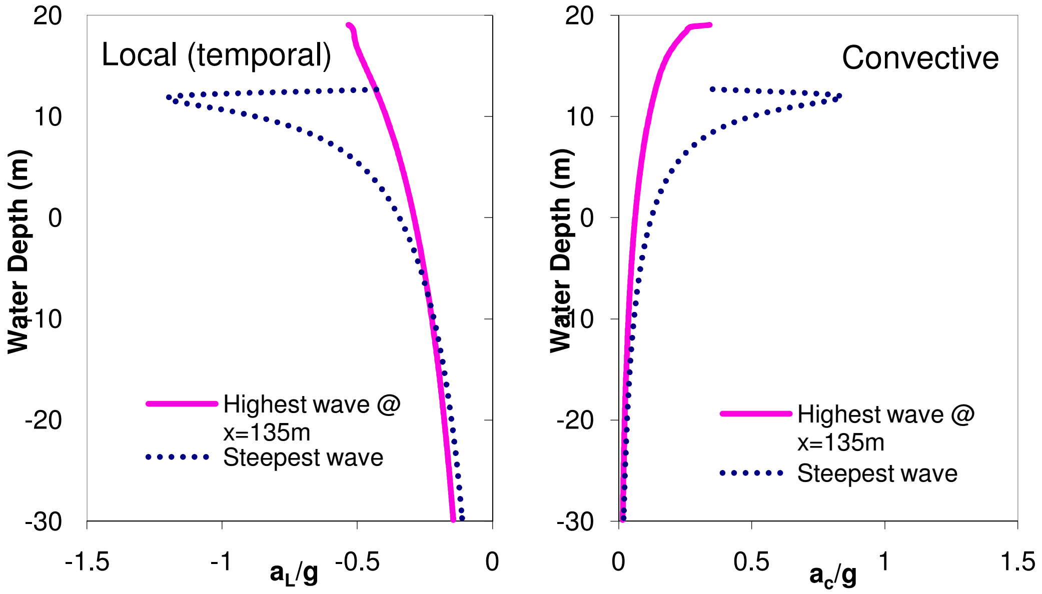

Figure 3.17: **Maximum Vertical particle acceleration components non-dimensionalized with g (H_s=17.67m, T_z=13.4s, JONSWAP peakedness parameter=2).**

3.7.1.4 Maximum Horizontal Acceleration

The steepest wave was found to be about 80% higher than the highest wave in terms of maximum total horizontal acceleration shown in figure 3.18 below.

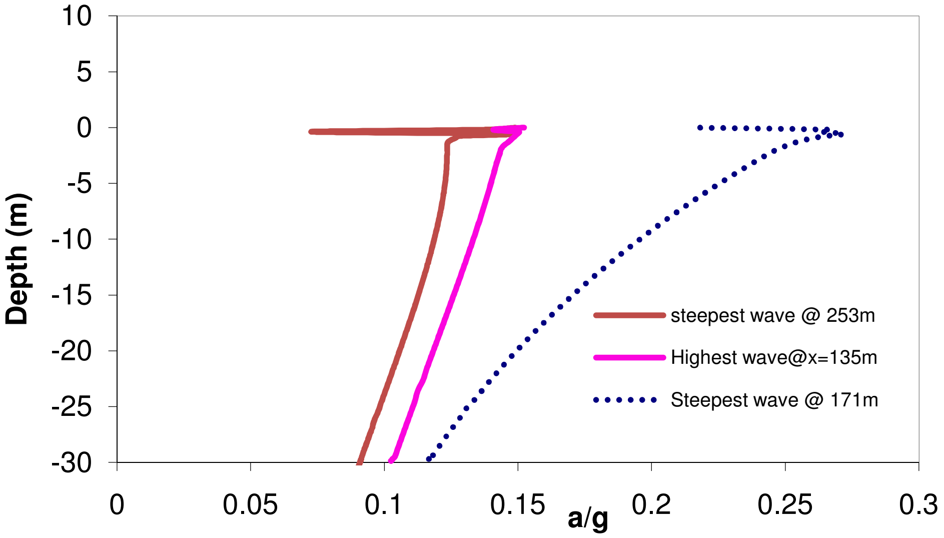

Figure 3.18: Maximum total Horizontal particle acceleration non-dimensionalized with g (H_s=17.67m, T_z=13.4s, JONSWAP peakedness parameter=2).

This is consistent with the conclusions of Swan et al (2000) that the maximum horizontal particle acceleration in the steep wave produced by focusing fronts can be greater than the highest wave generated by focusing crests. This implies that in a random sea state, an under prediction of the most likely horizontal inertial force on slender bodies will occur when the traditional NewWave is taken as the most extreme wave. This is also consistent with the laboratory work of Barltrop and Xu (2005) and Xu (2006) which determined that the highest wave does not necessarily result in the highest bow slapping loads. Similar to vertical acceleration, the convective and local parts of the horizontal acceleration were of opposite signs and similar order of magnitude. In the steepest wave at the zero up-crossing, the maximum convective and local (temporal, $\frac{\partial}{\partial t}$) components were

-0.37g and 0.58g respectively and are shown in figure 3.19.

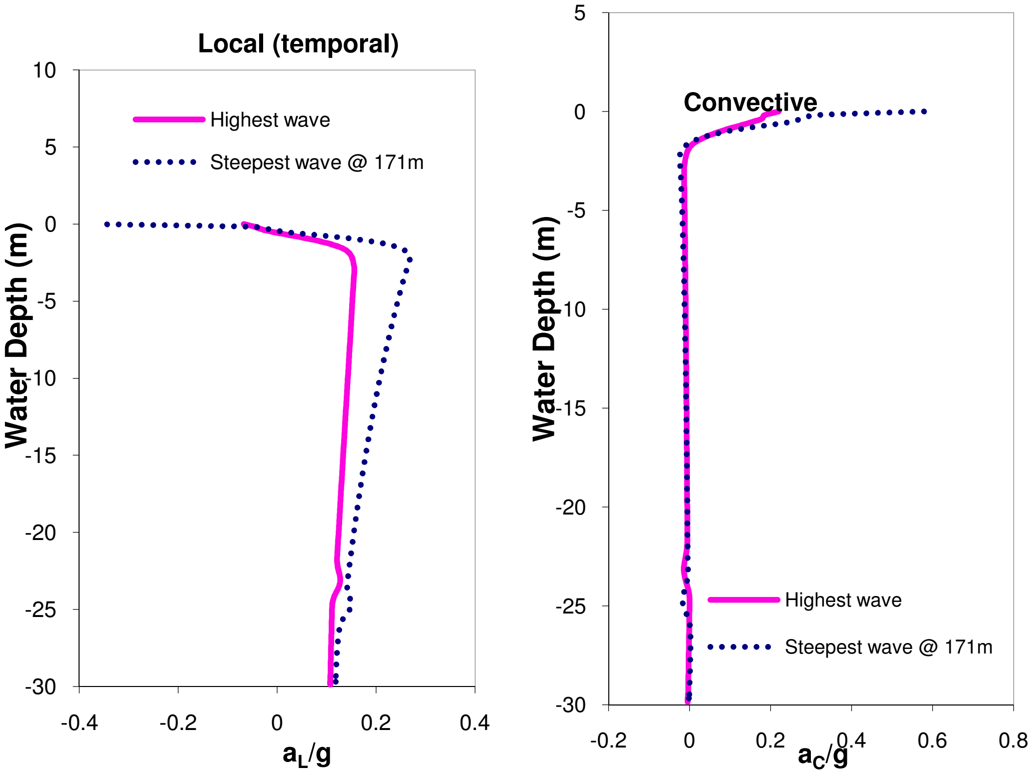

Figure 3.19: **Maximum Horizontal particle acceleration components non-dimensionalized with g (H_s=17.67m, T_z=13.4s, JONSWAP peakedness parameter=2).**

3.7.2 Frequency content of the extreme waves

In order to get a better understanding of the observed kinematics, it is useful to examine the spectral content of the extreme waves and the Stockwell transform (Stockwell, 1986) is quite attractive for this. The advantage of the Stockwell transform (S-transform) over conventional FFT (fast Fourier transform) of non-stationary data such as seen in focused extreme waves is described in Gibson and Swan (2006). In figure 3.20, contour plots of the amplitude spectrum (based on the S-transform of a 113s trace of water surface elevation) at the point in the tank (x=253m and x=171m for the steepest and highest wave respectively) where the extreme event was observed, is presented.

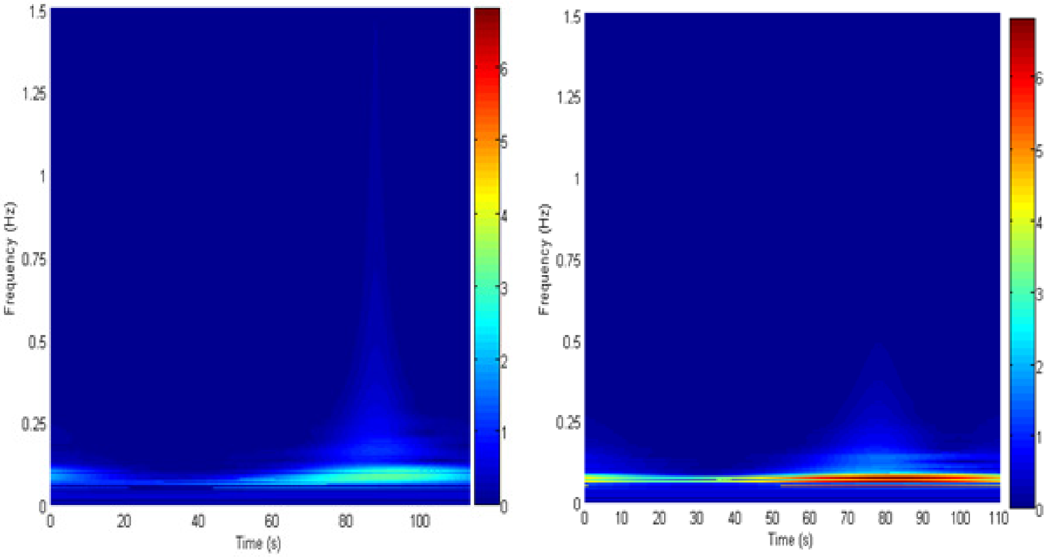

(a) Steepest wave

(b) highest wave

Figure 3.20: **Contour plots of spectral amplitudes (S-transform of 113s trace) recorded at the point in the tank where the extreme event was observed: (H_s=17.67m, T_z=13.4s, JONSWAP peakedness parameter=2).**

Notice how energy increases in the higher frequencies as the wave evolves towards focusing, reaching a maximum spectral width at the time of the extreme event and reducing as the wave defocuses. To present the data in the traditional 1-dimensional spectrum format, spectral amplitudes are extracted at the time (t=87.5s and t=77.77s for the steepest and highest wave respectively) of the extreme event and presented in figure 3.21 as a plot of amplitudes (normalized by amplitude of the dominant highest wave component) against frequency.

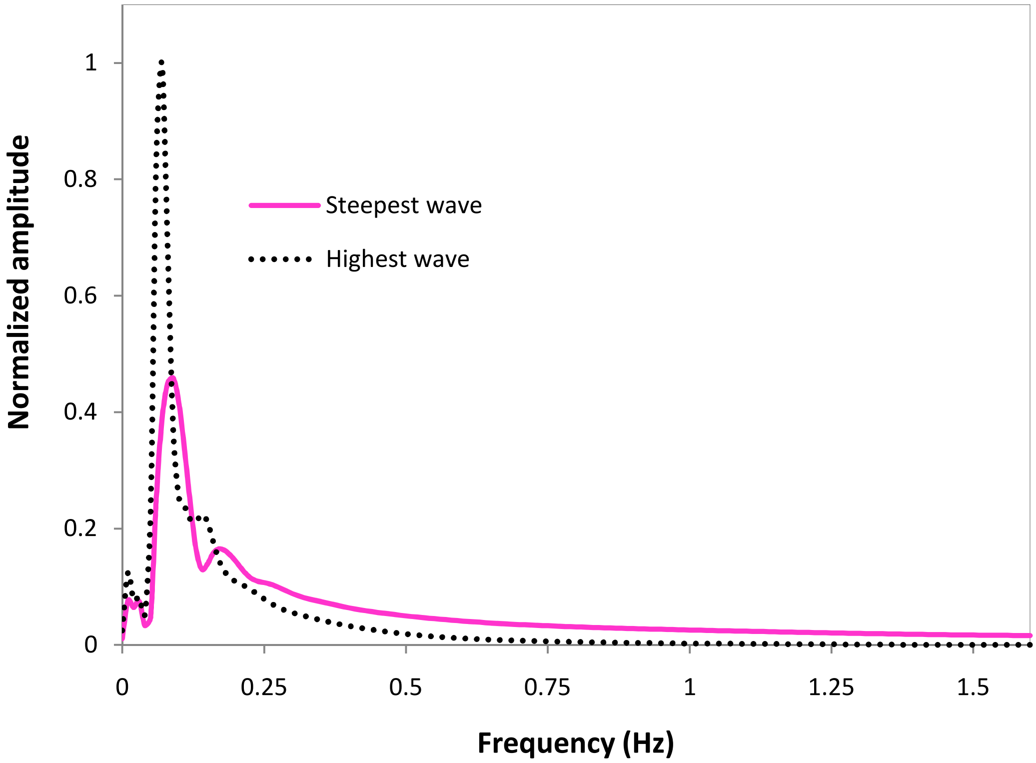

Figure 3.21: **Spectrum extracted at the instant of the extreme event (87.5s for steepest wave and 77.77s for highest wave) from figure 13 above: (H_s=17.67m, T_z=13.4s, JONSWAP peakedness parameter=2).**

It can be seen that although the dominant frequencies in the steepest wave are less energetic, there is greater energy in the tail of the spectrum. Whereas amplitudes drop to zero beyond 0.75Hz in the highest wave, amplitudes are quite appreciable in the steepest wave well beyond 0.75Hz and appear to continue to infinity in the tail of the spectrum. It is therefore not surprising that a very sharp increase in steepest wave horizontal particle velocity is observed in the region above MWL where kinematics is dominated by the higher frequencies and although the wave is not as high as the traditional "NewWave", higher kinematics are observed in the steepest wave. This is analogous to the observations of Gibson and Swan (2006) that in highly non-linear deep-water waves, the higher frequency components are modulated and energy is transferred into them to give a non-linear increase in kinematics. At this point, it is important to distinguish the present case from that investigated by previous authors (e.g Swan et al, 2000; Gibson and Swan, 2006 and Baldock, Swan and Taylor, 1996). Previous authors like Gibson and Swan (2006) and Baldock, Swan and Taylor (1996) were concerned with the highest wave and did not investigate the steepest wave. Swan et al investigated the alternative extreme wave (steepest wave) but as earlier mentioned, did so in the context of a narrow spectrum and without regard to the randomness of the wave components.

3.8 Concluding Remarks

Based on the new-wave theory, an alternative extreme wave can be defined to represent the steepest wave that is most likely to occur in a sea-state by working in terms of wave slope rather than amplitudes (crest-heights) as done in the traditional extreme wave characterized by height. This alternative extreme has not been given much consideration in the context of a realistic broad-banded random wave spectrum. Using a RANS/VOF model validated by experiment and the analytical higher order “NewWave” theory of Walker et al (2005), the properties of the alternative extreme wave and the traditional “NewWave” are investigated and compared. It was observed that the convective parts of particle acceleration were of similar magnitude with the local component and acted in opposing direction so that the neglect of the convective term could result in over-estimation of total acceleration by up to a factor of 3 in very extreme waves. It was also observed that although the steepest wave is not as high as the traditional new-wave, it gave particle velocities and accelerations that were greater than those of the traditional new-wave.

4 Observed Impact Pressure.

In chapter 3, kinematics of the simulated extreme waves were presented and some inferences about wave-loads were made from the observed kinematics. The aim in this section is to directly obtain (using the numerical model in Chapter 6) impact pressures on a small vertical panel placed at the position where the extreme wave crest occurs.

4.1 Background

A large number of wave impact load investigations have been conducted and an exhaustive review of them is not intended here. Rather, only a few of these works will be highlighted since the present focus is on comparative investigation of the impact loads induced by the traditional and alternative extreme waves in deep-water. Many investigations of wave impact loads on coastal structures have been conducted (e.g Cuomo et al, 2007; Wienke and Oumeraci, 2005; Peregrine et al, 2004; Causon et al, 2000; Kırkgöz, 1991; Blackmore and Hewson, 1984 etc). The majority of available results in deep-water are related to the problems of deck-slamming due to extreme wave-heights (see e.g Stansberg et al et , 2005; Sulisz et al, 2005; Baarholm and Faltinsen, 2004; Baarholm et al, 2001; Baarholm, 2001; Bea et al, 1999; Kaplan, 1992 etc) and green-water (e.g Pham, 2007; Fonseca and Guedes-Soares, 2005; Varyani et al, 2004; Nielsen and Mayer, 2004, Buchner, 2002 etc). The few deep-water investigations dealing with breaking-wave impact loads are mostly based on impact events resulting from waves akin to the limiting traditional extreme wave. For example, Chan and Melville (1988) investigated pressures on a vertical wall resulting from the plunging breaker generated by focusing wave-crests of individual components of a wave-train.

Investigations of deep-water extreme wave impact which explores the relative significance of wave-front steepness and wave-height with respect to induced load, is however rare. Indeed, Kjeldsen et al (1986) and Kjeldsen and Myrhaug (1979) had concluded from their investigation of extreme (typically asymmetric) waves, that wave front-steepness is similarly if not more relevant than the traditional wave-height parameter in characterizing extreme wave loading. More recently, Xu and Barltrop (2008 (1) and (2)) have reported experimental results of breaking-wave impact loads on an FPSO bow in deep-water and showed that the traditional extreme wave (based on height) did not always result in the largest loading.

4.2 Approach

Using the numerical approach described in chapter 3, it is aimed in this section to explore the relative severity of the impact load exerted by the traditional and alternative extreme waves on a stationary vertical wall as a simplistic precursor to the side-shell of a ship-shaped marine structure. Having determined the time and position where the extreme event occurs in the traditional as well as the extreme wave, a 1m panel is placed at the point where the top of the extreme wave crest occurs (as determined in Chapter 3) and the time history of the force on the 1m^2 panel is recorded as the time history of maximum pressure exerted by the wave crest.

4.3 Observed impact pressures

The recorded pressures exerted by the traditional and alternative extreme waves on the panel at their crests are shown in figure 4.1.

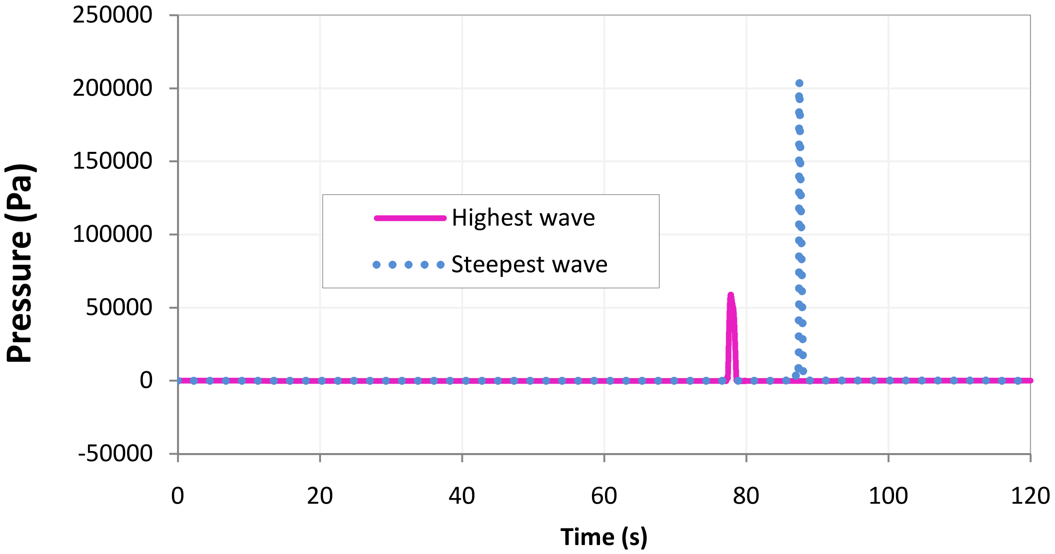

Figure 4.1: Time history of observed pressure on the 1m^2 vertical panel at the wave-crest top.

Similar to the inference from the kinematics recorded in chapter 3, the steepest wave indeed has a peak pressure that is several times that of the highest wave. Furthermore, the duration of the steepest wave impact seems slightly shorter than that of the highest wave. Figure 4.2 is a zoom-in on the impact segment of the time history.

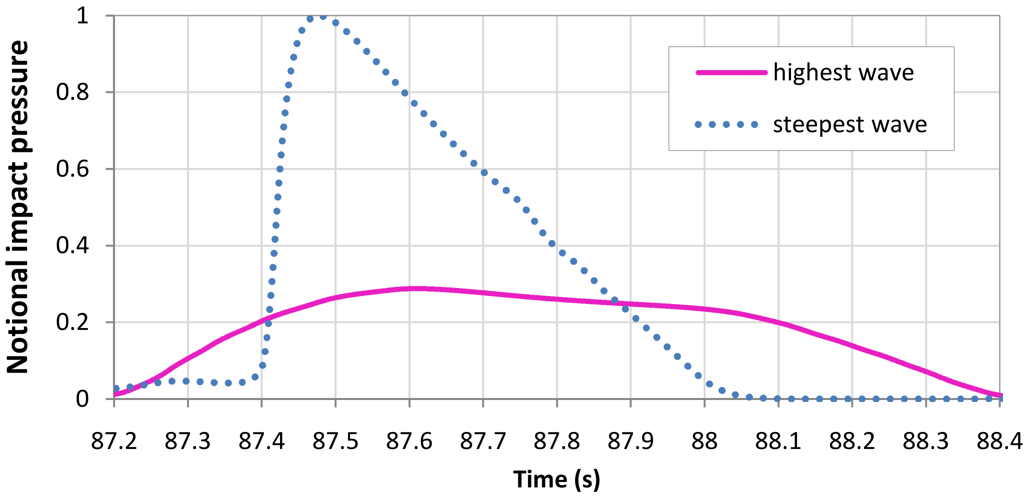

Figure 4.2: Magnified time history of normalized impact pressures observed (highest wave pressure has been shifted in time to coincide with the steepest wave impact pressure)

It can be seen that while the rise time of the steepest wave is about 0.075s, it is about 0.4s for the highest wave. During the rise phase of the impact, an average dynamic force (pressure rise) of 2,520 N per milli-second and 47 N per milli-second are exerted by the steepest and highest waves respectively, on a unit area of panel. This means that during impact, pressure rises faster with the steepest wave than the highest wave by a factor of nearly 54. Furthermore, the rise and decay phases are almost symmetrical in the highest wave (total impact duration is about 1.2s) but asymmetrical in the steepest wave (decay phase is slightly more than 7 times longer than the rise phase).

4.4 Discussion.

It can also be seen that the usual pressure oscillation present in measurements is virtually absent in the present results. This can be explained by the fact that in the present simulation, the wall on which pressure is measured does not move in contrast to physical experiments where the wall or even the pressure sensor may be vibrating as a result of the impact (Peregrine, 1995) . Furthermore, little or no air is trapped by the breaking wave and there is no significant ‘pile-up’ of water on the wall-structure (vertical plate) since the plate is small (1m^2) in comparison to the crest height (12.5m above MWL) and is placed at the point where the crest-front is just vertical. Obviously, this is before the wave-overturns and air is entrapped by the emerging jet. Unlike in typical 2-d experiments, the 3rd dimension in a 3-d impact provides an escape avenue for the air that might be trapped in a 2-d air-pocket (Peregrine, 1995). This can result in less air-cushioning, higher impact pressures and less pressure oscillations. It is important to point out however, that more detailed discussion of the effect of air in wave impact events is outside the scope of the present work. As a result, let it suffice to limit the treatment of aeration and air entrapment to the above discussion.

One of the advantages of the present approach over experiment is the elimination of the scale effects of surface-tension. Another important advantage is the possibility of obtaining very high resolution of impact pressure measurement. This is important since in dealing with waves, it is necessary to account for the variation of pressures with height without which measurement of forces over a height greater than one meter will give lower pressure values as a result of averaging over a larger area. While it has been possible in the present viscous flow simulation to record the force on a 1m panel at the wave crest, obtaining such degree of resolution in a 1:80 scale experiment for example, will require a 12.5mm pressure pad. Apparently, the practical challenges of finding such a small pressure pad and obtaining meaningful measurements from it, is quite considerable. For example, it was noted in Xu and

Barltrop (2005) that the smallest loaded area on which they could measure forces was equivalent to a full-scale value of 1.9m^2.

5 Wave-rider: alternative approach to water particle kinematics.

While the theoretical analysis of regular waves and hydrodynamic loading in general are fairly mature subject areas, the underlying kinematics of a random sea is not very clear especially in the region above the calm-water surface (i.e mean water level). This has been a major challenge and the many Fourier perturbation approaches put forward with the exception of the second order methods (e.g Zhang et al, 1992, 1993a and Dean and Sharmer, 1981 as implemented by Stansberg et al, 2006 and Kim, 2008) and the fully non-linear methods (Bateman et al, 2001; Grue and Fructus 2008) have not been very robust because they do not take into account the inherent wave-wave interaction which is a very important factor in kinematics. The method proposed by Taylor (1992) accounts for this interaction in a simple way analogous to second-order theory but its prediction is not in good agreement with results obtained from the simulations in Chapter 3. Although the more robust methods are extensively validated, they are complex and involve considerable computational resources. A procedure which is simple and is based on the linear theory like the other simple stretching/extrapolation methods and yet gives better results is therefore desirable from a practical engineering point of view. It is attempted to develop such a method in the following section.

5.1 Wave-rider

Longuet-Higgins and Stewart (1960) have showed the interaction of two waves in the form of long-waves lifting-up the shorter, high frequency wave components above MWL so that the short waves are said to be riding on the longer wave components. The new method (here referred to as "wave-rider") is based on this assumption of short wave components riding on the long wave components. The elevation of the shorter wave is thus calculated from the surface of the longer wave using it as the datum.

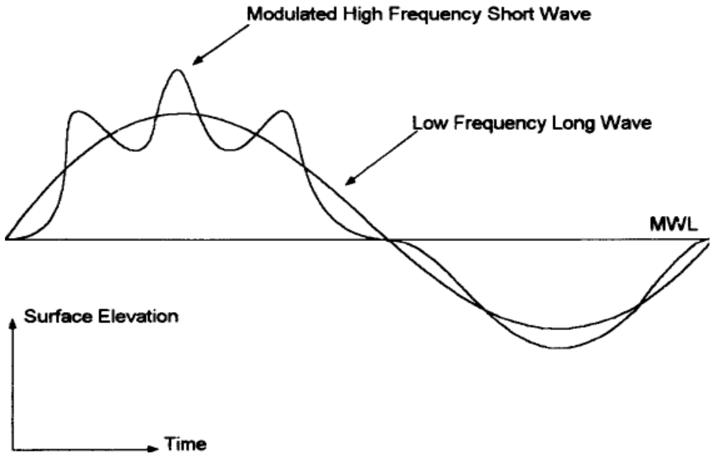

Figure 5.1: **Modulated High frequency (short) wave riding on a Long frequency wave** **(Longridge et al, 1996)**

The datum of the first (lowest) frequency component w_1 is taken as y=0 while for the next component w_2, the datum is taken as the water surface constituted by w_1 i.e $a_1*\cos(k_1x-w_1t)$. For the third frequency component, the datum is the water surface constituted by the superposition of the first two components. This is continued for all frequency components- in effect, wave-wave interaction is assumed to be in the form of shorter waves riding on the longer waves. This interaction is triggered on the basis of the relative lengths of component waves and discretely implemented by assuming that the degree of this "riding" is different for waves close to j in length and waves much longer than j. An assumption that is consistent with the observations of Zhang et al (1996) that the interaction of waves which are far apart and those which are closer together in a frequency spectrum are distinct. The implication of this “short wave-riding-long wave” interaction is that in the e^{kz} term, a different z (elevation) is defined for each component j, on the premise that the datum for each wave-component’s elevation is the sum of the elevations of all components longer than j since j is assumed to be riding on waves longer than it.

To further understand the present simplistic form of long-wave/short-wave interaction, consider the short wave j in a spectrum with q other waves. Obviously, waves shorter (frequencies higher) than j are ignored in defining the elevation of j since j is assumed to be riding on only waves longer than itself. Among the waves which are longer than j, there are some on which j will fully ride because they are much (greater than twice) longer than j. However, j will only ‘partially ride’ on the other components which are of intermediate length (i.e longer than j but not more than 2 times longer). This is because intermediate waves are closer to j in length and are also being pushed up to the surface by the much longer waves. Therefore in defining the baseline/datum for the elevation of j, the full elevation of the long waves are taken into account because j is fully riding on them but only a fraction of the elevation of the intermediate waves are taken into account since j is only partially riding on them. This as earlier mentioned is in line with Zhang et al (1996). The degree of “riding” on the intermediate waves by j, reduces as the length/frequency of the intermediate wave approaches that of j and tends to zero when they are equal (i.e j is not allowed to ride on itself or other components shorter than it).

The above simplistic interaction is mathematically implemented using a term "Num" which defines for every j component the fraction of spectral components (longer than j) which are at most two times longer than the j^{th} component and assumed not long enough to fully interact with j as long-waves so that the fraction of components upon which j is fully riding is given by nNum = 1-Num. One may expect a slight variation in nNum depending on the descretization of the spectral frequencies, δω. However, it is found that a useful approximation for nNum may be obtained by first defining a function, P which compares the length of the j^{th} component with the length of all other components q:

$$P(q,j) = q\ ,\ \text{if}\ \ \frac{\omega_j^2}{\omega_q^2} > 2;\ \ \text{else}\ \ P(q,j) = 0, \quad \text{where } q \equiv j.$$

The maximum value of P(q,j) for a given j gives Num which represents the number of components longer than j by not more than a factor of 2. By plotting $\frac{1-\mathrm{Num(j)}}{\mathrm{j}}$ against a range of $\frac{\mathrm{j}}{\mathrm{Nn}}$ (Nn= total Number of components) and fitting a polynomial to the curve, an expression for nNum is obtained in terms of j (for the case investigated) as:

$$\mathrm{nNum}(j) := \min\left[3.8356\left(\frac{j}{Nn}\right)^4 - 10.93\cdot\left(\frac{j}{Nn}\right)^3 + 11.745\left(\frac{j}{Nn}\right)^2 - 5.8997\cdot\left(\frac{j}{Nn}\right) + 1.6669, 0.99\right]$$

where nNum(j) is truncated just before 1.0 to indicate that all components equal to or greater than twice the length of the jth component are very long waves relative to j and will fully carry j (to the same degree) which is consistent with classical concept of long-wave-short-wave interaction.

5.1.1 Long waves

Using the criterion that all waves greater than twice the length of j are long enough to fully interact with j by acting as a carrier for j, we can find for every j, the percentage of all waves longer than j which are long enough (greater than twice the length of j) to fully carry j.

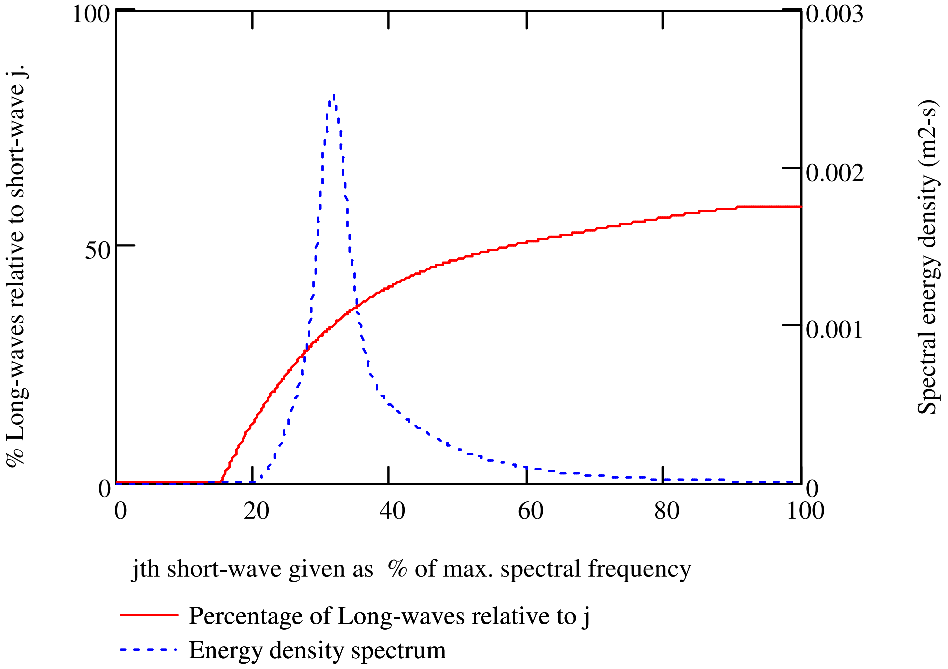

Figure 5.2: Long waves (relative to a short wave j) in a spectrum.

In figure 5.2, 0 to 100 on the x-axis represents all frequency components j in the spectrum expressed as a percentage of the maximum frequency of the spectrum. The y-axis represents the percentage of components longer than j assumed to be fully carrying j by virtue of being at least twice its length.

5.1.2 Intermediate waves

Since we know all waves longer than j will interact with j and among these, a certain fraction nNum = 1-Num shown in figure 5.2, will interact fully; it is easy to determine the waves which are close to j and will only partially carry j.

5.1.3 Interaction Mechanism

Having established the longer full carrier waves and the intermediate partial carrier waves, a discriminatory function f(j,q) can be defined which describes the degree to which a short wave j in the spectrum rides on q long-waves in the spectrum. Therefore the discriminatory factor f(j,q) is introduced, which assigns a value of 1 to fully carrying long waves and a value between 1 and zero to intermediate partially carrying waves: zero implying that the short wave j does not ride on itself. This reflects the degree of interaction depending on the ratio of the frequencies of the interacting waves.

$$f(j,q) := \text{if}\left[q > ii(j), \left(\frac{w_j}{w_q}\right) - 1, 1\right] \tag{5.1}$$

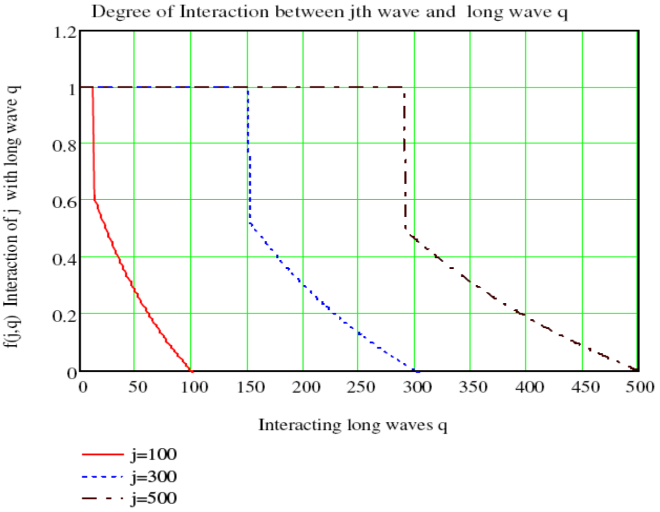

Figure 5.3: Degree of interaction ("riding") between jth wave and long waves q

In equation 5.1 above, ii(j) is a counter which defines the threshold at which the transition from full to partial carriers occur and is given by

$$ii(j)=floor(nNum * j) \qquad (5.2)$$

Therefore, f(j,q) represents the degree of classical Long-wave/short-wave interaction between any short wave j and longer waves q .

5.1.4 Implementing Interaction

The component j is thus considered to be riding on these longer components which interact with it and the elevation of j is therefore measured from the water surface constituted by the linear sum of the elevation of all waves longer than it but taking into consideration that j only rides partially on the intermediate waves.

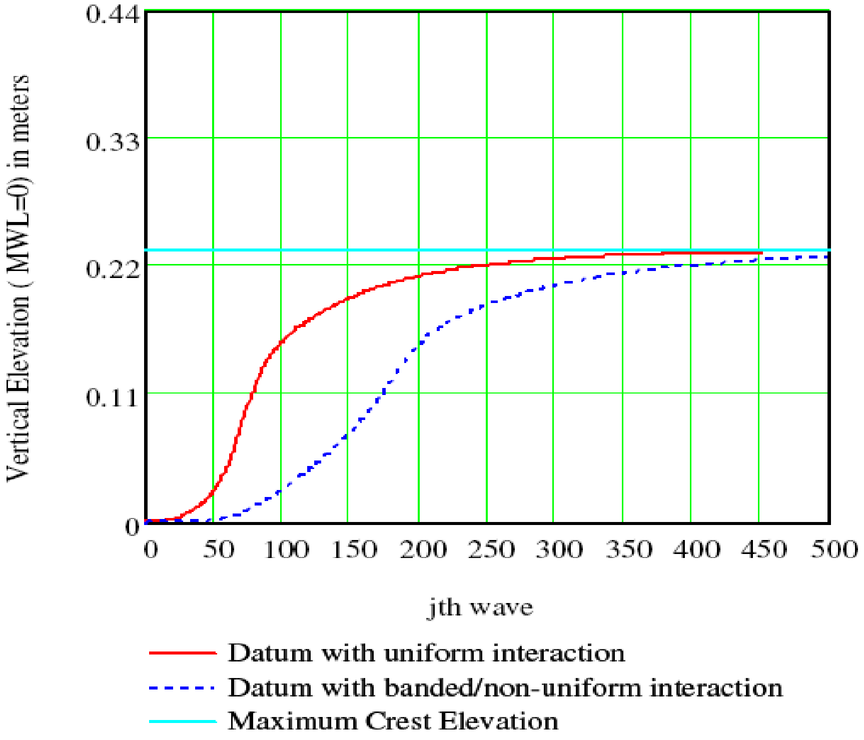

Figure 5.4: Baseline/Datum for the Elevation of the jth wave

This is done by defining a baseline Y(j,x,t) for every j which is a function of position and time, using the discriminatory function f(j,q) to represent varied degrees of (non-uniform) interaction associated with different wave bands in the spectrum.

$$Y(j,x,t) = \sum_{q=1}^{j} f(j,q) * gg(q,x,t) \qquad (5.3)$$

In equation 5.3 above, gg(q, x, t) is the surface profile of frequency component q. By summing up to j in equation 4.3, it is implied that all frequencies higher than j are shorter than j so that j does not ride on them. This means that they do not interact with j and therefore do not affect the effective elevation of j which is measured from the elevation of its carrier-wave defined by the base-line/datum given by equation 5.3.

Therefore assuming z is a vertical elevation measured from the MWL, an effective elevation Z_j (see figure 5.4) is defined for j thus:

$$Z_j = z - Y(j, x, t) \qquad (5.4)$$

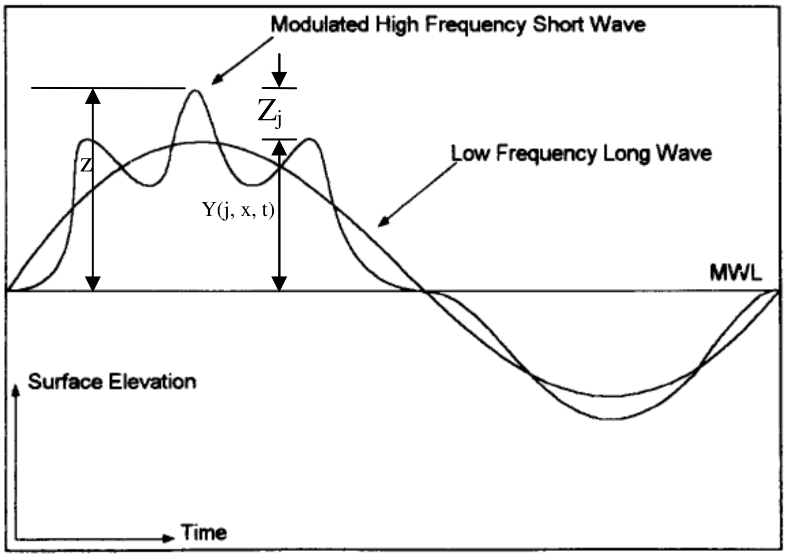

Figure 5.5: wave-rider scheme

So for every j component, there is a corresponding z(j) elevation determined by the degree of interaction between j and each q within the spectrum, which is based on the relative frequencies of j and q. The new model is thus implemented by simply replacing the elevation term, y in the e^{kz} term in linear theory (equation 2.35) with the new elevation given by equation 5.4 for each j wave component (Further details in Appendix A7).

5.2 Validation of Method

To check the usefulness of the new method, results are compared with Wheeler stretching, as well as laboratory measurements of Skjelbreia et al, 1991 (as cited by Stansberg et al, 2006) and second-order predictions reported by Stansberg et al, 2006. Dependence on spectral frequency cut-off is also checked.

5.2.1 Sensitivity to Spectral cut-off

Sensitivity of the method to spectral cut-off frequency was investigated and reasonable stability was achieved at 3.9 times the peak-frequency.

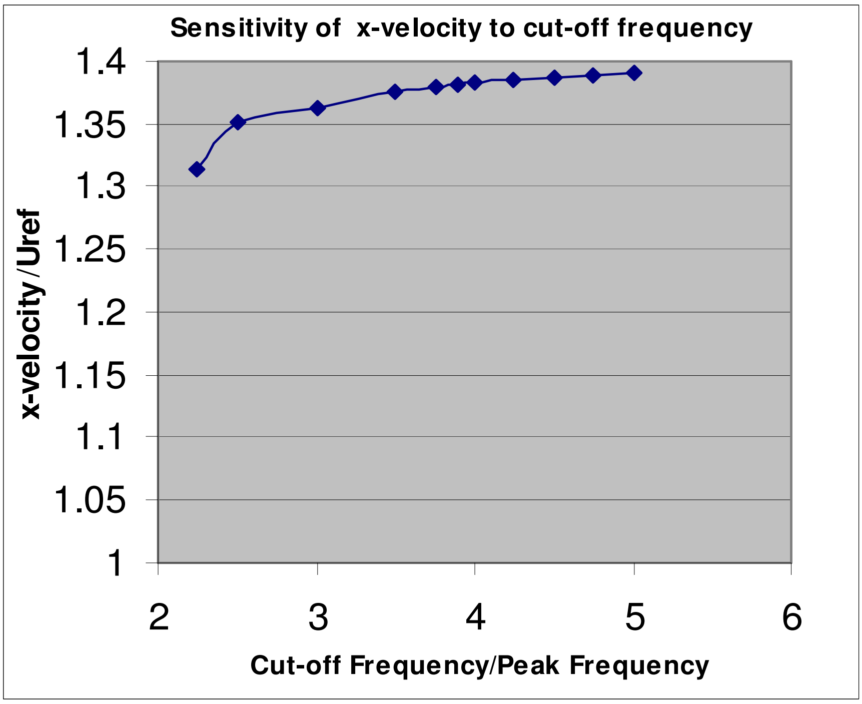

Figure 5.6: Sensitivity of horizontal particle velocity to spectral frequency cut-off (Uref is velocity at MWL)

5.2.2 Comparison with Published Results

It has been possible to synthesize a time series which is reasonably similar to those reported in Stansberg et al (2006). Figure 5.7 shows the time History of water surface elevation calculated in the present study (analytical) and the measurement of Skjelbriea (1991) reported in Stansberg et al, 2006.

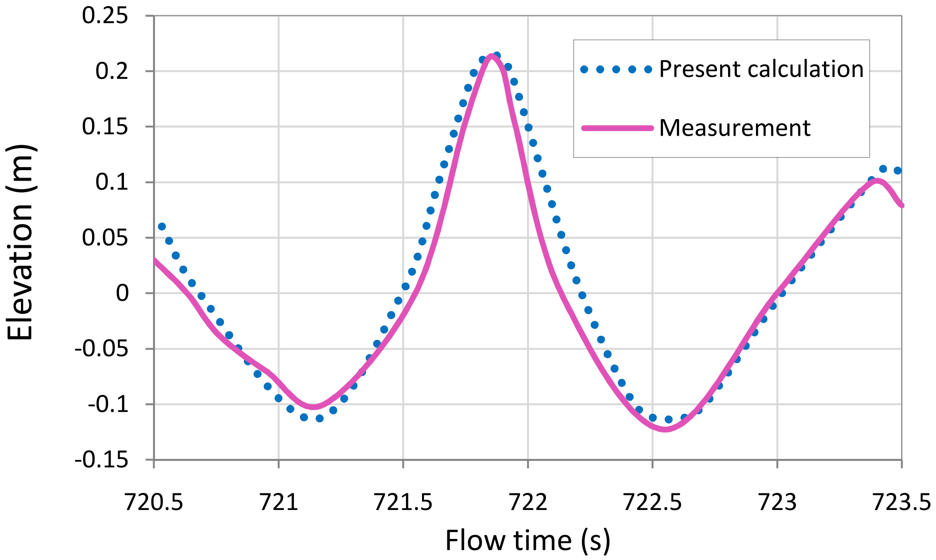

Figure 5.7: Surface elevation time series of calculated (analytical) and measured (experiment of Skjelbriea, 1991) extreme wave.

The extreme wave event was measured in experiments by Skjelbreia et al, 1991 and reported in Stansberg et al, 2006. The present analytical crest height and local period of the extreme wave is in very good agreement with the measurement while the elevation of the trough is under predicted in the analytical wave. Although it can be seen that the analytical wave is slightly more rounded in comparison with the measured wave, the difference is more important in wave impact events where impact force is essentially dependent on the rate of change of added mass which itself is determined by wave front-steepness. From a local period of about 1.5s, a local steepness, ak (a = max crest height, k is based on zero-crossing wave-length about the extreme crest) of ak=0.3938 is estimated for the analytical wave. This is very close to the measured wave's value of ak=0.395 reported by Stansberg et al (2006) and represents a difference of only 0.3%. Moreover, the comparisons in section 5.3.2 (figures 5.11 and 5.13) of measured kinematics and the non-linear form of the present method as well as in section 5.5.1 (figure 5.16) of viscous flow and linear wave-rider results for the traditional extreme wave, indicates that this difference is of very little consequence in the present method's ability to predict particle kinematics. To further confirm that the analytical wave used in the present calculation is a reasonable representation of that measured by Skjelbrei et al (1991) and calculated by Stansberg et al (2006), the present linear theory predictions of horizontal particle velocity is compared with the linear theory prediction of horizontal particle velocity calculated by Stansberg et al (2006) for the wave measured by Skjelbrei et al (1991).

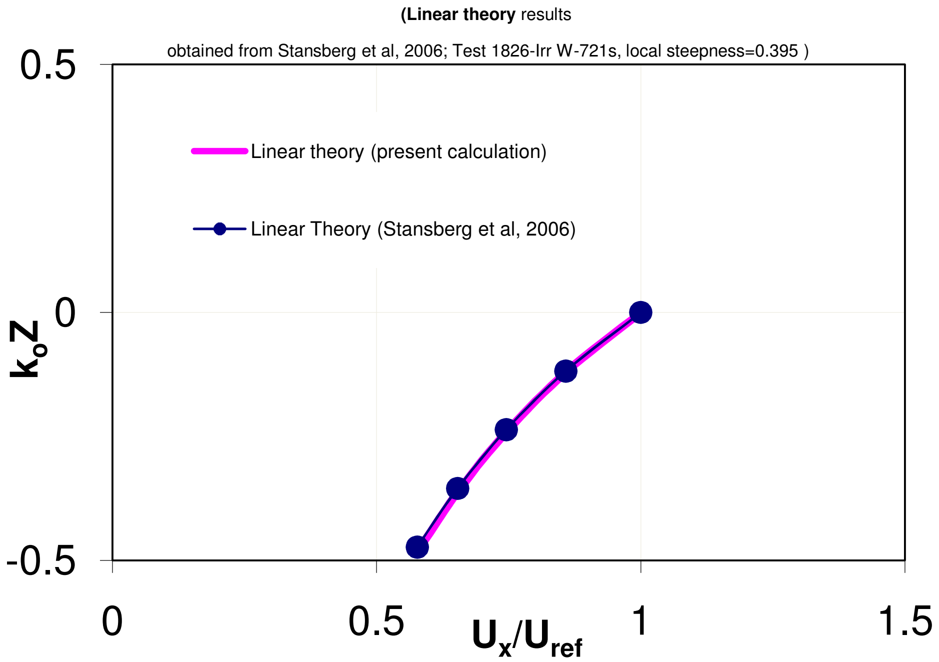

Figure 5.8: Calibration of present wave with that of Stansberg et al, 2006 (and by extension Skjelbrei et al (1991))

Apparently, the linear theory prediction for the wave measured by Skjelbrei et al (1991) is in very good agreement with the linear theory prediction of the present calculation. This shows that the wave used in the present calculation is indeed a good representation of the measured one. Based on all the above comparison of the analytical and measured wave, it is reasonable to conclude that the present calculation is indeed consistent with the measurement and it is therefore appropriate to compare kinematics results of the new method with the measured values of Skjelbrei et al (1991).

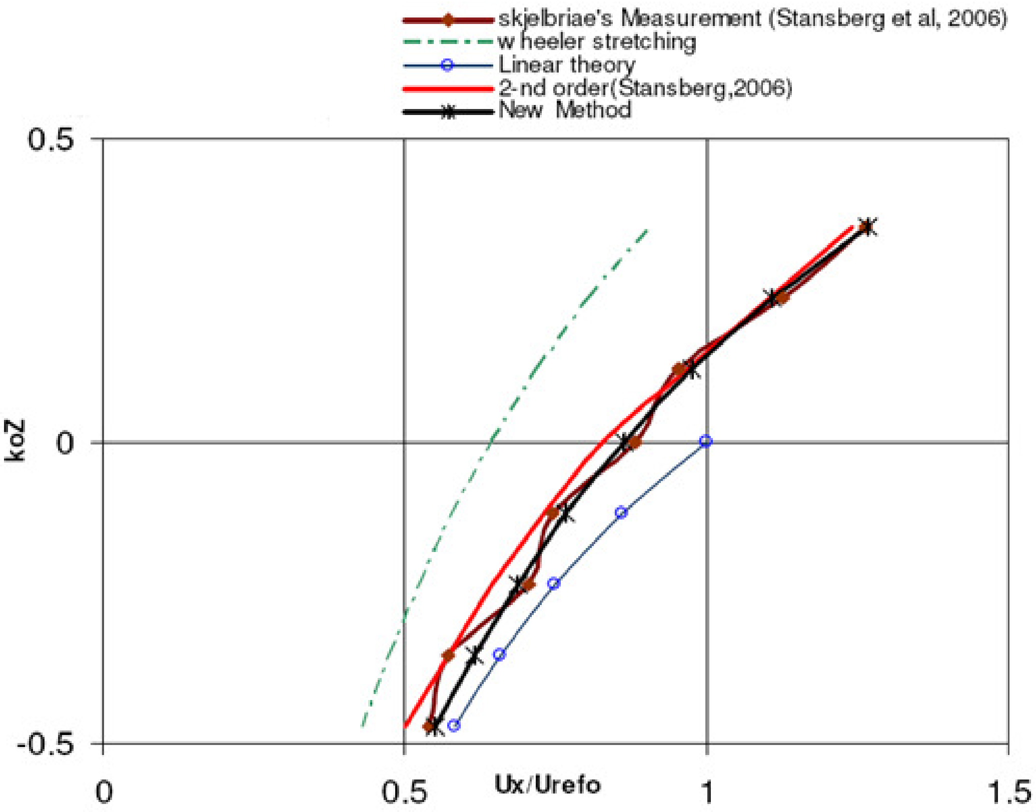

Figure 5.9: **Non-dimensionalized Velocity Profile under extreme crest (2nd order and measurement here refers to velocities reported by Stansberg et al, 2006)**

It is obvious in fig 5.9 that the new method definitely gives better results than Wheelers method as well as linear extrapolation. It can be seen that predictions of the new method are even closer to laboratory measurements than Stansberg's 2nd order results in the region below and above MWL. The degree of agreement between results of the new method with measurements of Skjelbriea (1991) reported by Stansberg et al (2006) is surprisingly good. This is especially so in the region above MWL which has been the region posing the most challenge. It can also be seen that in the region below MWL, results of the new method seems to follow a path that is an average of the scatter of points on the curve of measured results. This means that the experimental fluctuations experienced in the lab are smoothened-out in the new method which suggests that the results of the new method are even more reliable than laboratory measurements because of experimental uncertainties.

It is important to note that the ak=0.395 steepness of the ‘test wave’ used here is quite high. Therefore the wave is non-linear and any kinematics model which gives reasonable results at this order of steepness is a very useful tool considering the importance of crest top kinematics where maximum velocities are normally expected and ironically, experimental data is hard to obtain especially because of the difficulty associated with intermittent water surface and placing measuring devices in this region. Although good agreement has been achieved, it is useful to bear in mind that the validation has been on the basis of a single measurement. It will be useful to compare results of the new method with more measured results. Since the method is purely rational (except the assumption of long-waves being those that are at least 2 times longer than a given short -wave) and does not contain any empirical tuning to fit measurement, it is expected that once the surface elevation (and by extension the component amplitudes and frequencies) are known the new method will produce consistent results.

5.3 Nonlinear wave-rider

So far, the wave-rider method presented has been based on a linear theory representation of particle velocity and has produced results consistent with measurements of Skjelbriea (1991) as cited by Stansberg et al (2006) and second order prediction. However, full-scale measurements of Farmer (2002) have since shown crest velocities that are much larger than second order theory would suggest. Baldock et al (1996) and Grue et al (2004) have also recorded crest velocities that are larger than linear theory and much larger than second-order predictions, in very steep waves (non-breaking). It is thus desirable to extend the initial wave-rider method (section 5.1) to a nonlinear form of particle velocity with the aim of establishing how results of such an approach compares with the results of Baldock et al (1996).

5.3.1 Non-Linear Approach to Particle Kinematics.

Similar to the approach adopted by Walker et al, 2005 (described in section 2.6.2.3), a non-linear expression for particle velocity based on the combination of a linear description of the wave and its Hilbert transform, can be written (see Appendix A7). Higher order effects are accounted for by using similar Stokes-type correction used in the non-linear expression for elevation but modified for velocity. These terms are analogous to Stokes coefficients which are expressed in terms of hyperbolic functions of kd, the only difference being that the wave-number k is replaced by celerity. So for our case where we use zero-crossing period to define k, the correction terms are defined in terms of the inverse of zero crossing celerity i.e $kd \equiv d/c_z$ (where c_z is zero crossing celerity).By doing this, we obtain a non-linear expression for velocity. However, another problem analogous to that of "high frequency contamination" in linear theory arises. This is obvious as velocities given by this approach are considerably larger than experiments.

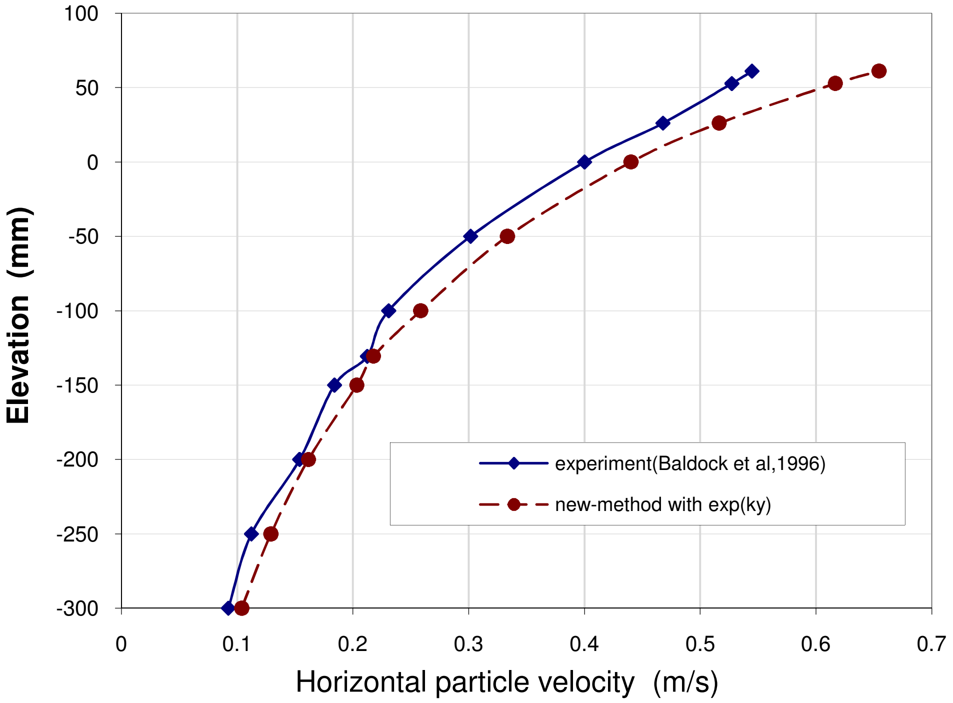

Figure 5.10: Predicted non-linear horizontal velocity without including the simplistic "wave-rider" interaction (section 4.1).

This "frequency-contamination" problem is resolved by applying the "wave-rider" technique described in section 5.1.

5.3.2 Validation of the Non-Linear Approach

In this section, horizontal particle velocity result obtained by the method described in 5.3.1 (non-linear wave-rider) is compared with measurements reported by Baldock et al (1996). Baldock et al (1996) measured horizontal particle velocity at the focus point of a focused wave-group to obtain kinematics of an extreme event.

First, time series of the extreme event is presented where the dotted represents the extreme wave measured in the experiment of Baldock et al, 1996.

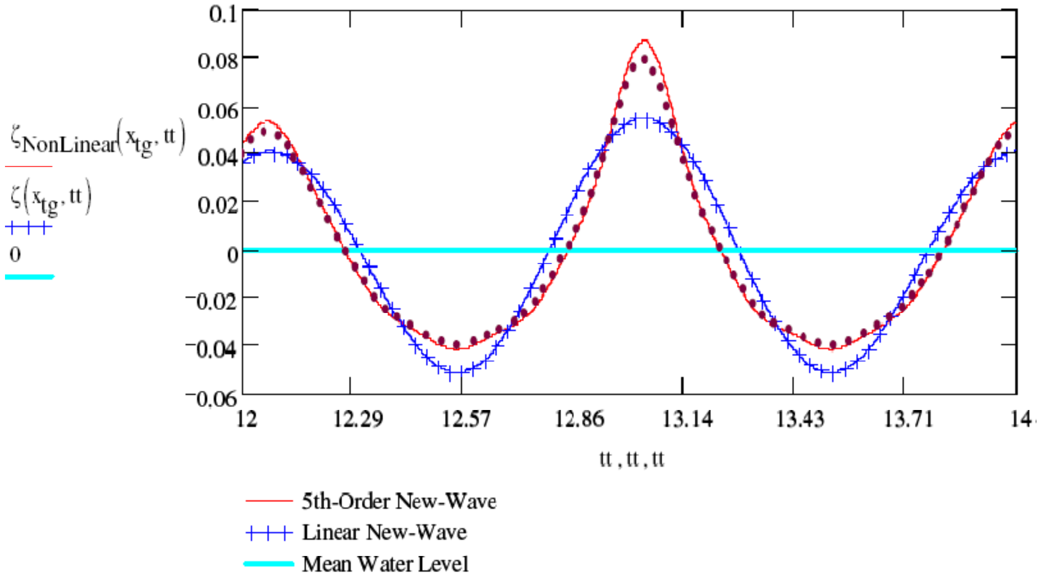

Figure 5.11: Comparison of theoretical and measured crest elevation

Although the fifth-order new-wave used in the present calculation over-predicts the crest elevation, it is a reasonable representation of the measurement. This can be seen in the remarkably good level of agreement between the linear theory velocities calculated in this work and those calculated by Baldock et al, 1996.

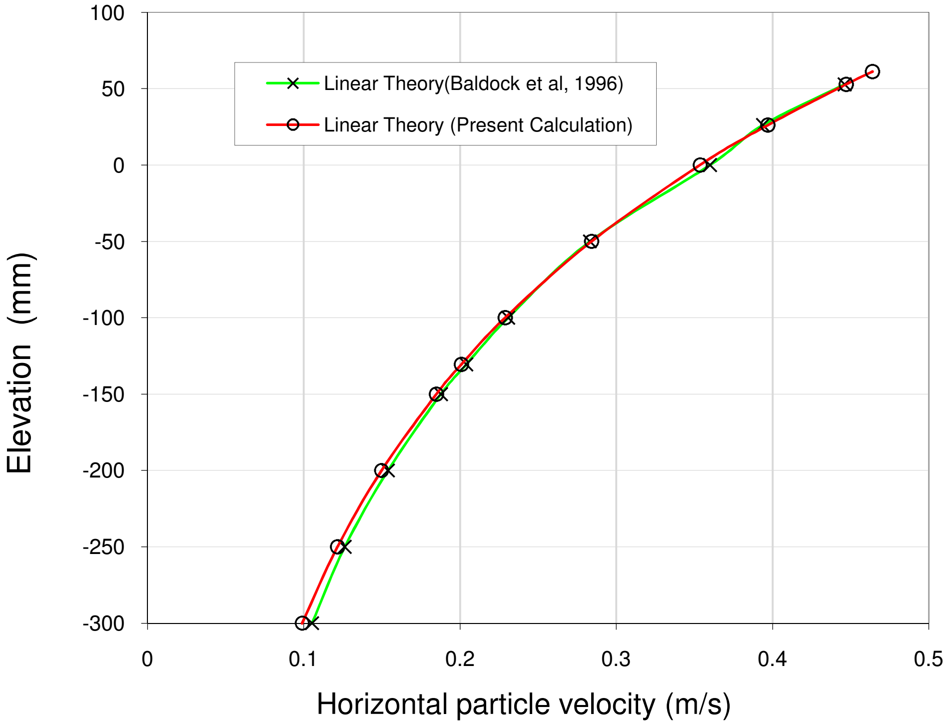

Figure 5.12: Comparison of linear theory particle velocity obtained in the present calculation and equivalent linear theory particle velocity obtained by Baldock et al, 1996.

In fig 5.13 below, horizontal particle velocity result of the non-linear method is compared with the most extreme crest (case D, A=55mm) in Baldock et al (1996). There is a surprisingly good agreement between results of the new-method and the experiment of Baldock et al. This is especially so up to 50mm below the MWL (about 68% of maximum crest elevation).

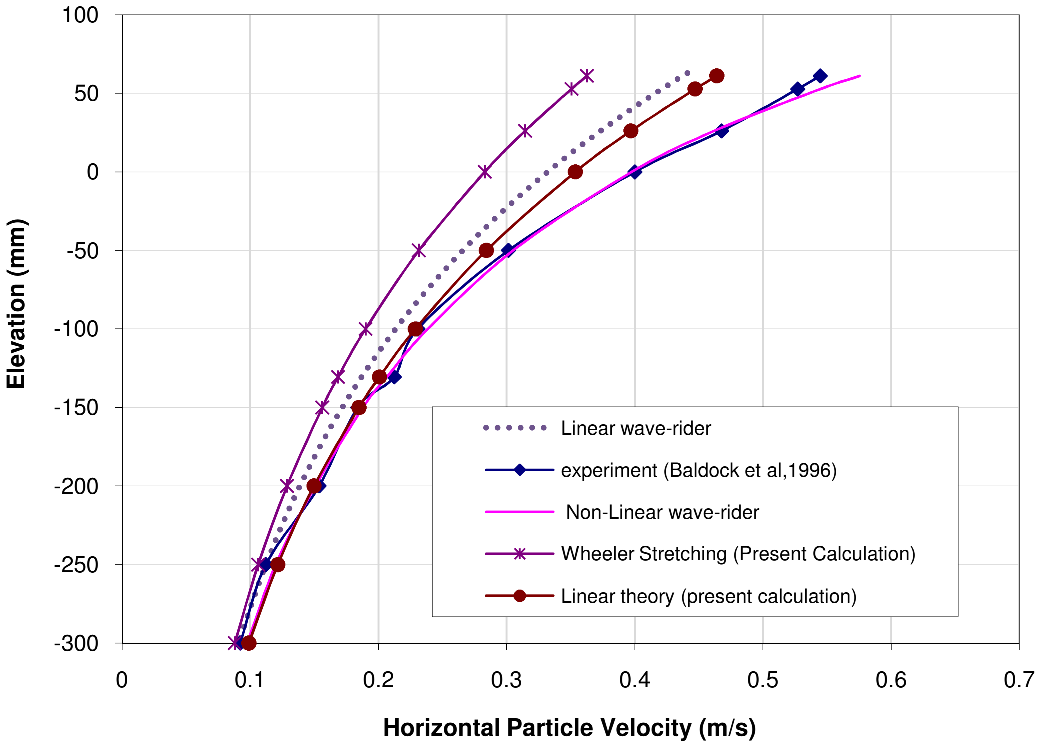

Figure 5.13: Horizontal particle velocity results of the non-linear wave-rider method compared to other results in literature

From 50mm above MWL and upwards (near the water surface), the new method seems to slightly over-predict measured velocities. As can be seen in the region below 50mm above MWL, the new method seems to follow a path which averages the scatter in the points on the curve of measured velocities. It can therefore be argued that the seeming over-prediction near the free-surface (from 50mm above MWL) is really a result of scatter in measured velocities and it may actually be that laboratory measurements have not been able to capture the full magnitude of velocities near the free-surface. This is understandable, considering the challenges of water-surface intermittency and difficulty in obtaining measurements near the free-surface. It is therefore reasonable to say that the nonlinear form of the new method is a good representation of particle velocities at all elevations under the crest especially in the region above MWL which for reasons earlier stated, has traditionally been the most challenging region in which to obtain reliable particle kinematics. By definition, the linear form of the new method can only give results that are less or at most, equal to strictly linear theory results. As can be seen in figure 5.13, measured and nonlinear "*wave-rider*" velocities are larger than linear theory predictions above mean water level. This implies that linear "*wave-rider*" predictions especially in the region above mean water level will be less than the measuremts of Baldock et al (1996). Considering that the linear "*wave-rider*" method had been validated with measurements of Skjelbriea et al, 1996 (as cited in Stansberg et al, 2006) one is faced with the question of which experimental result is more reliable. This predicament had been earlier noted in section 2.7.2 (table 2.1) of this work and is something to be investigated in the future.

Overall, comparison of results of the non-linear wave-rider method with those of Baldock et al (1996) and by extension, those of Grue et al (2004), has shown a good agreement with the measurements and significant improvement over existing stretching methods.

5.4 Comparison of Observed Kinematics

It is attempted here to compare results of the wave-rider method to the particle velocities obtained from the Fluent simulations in Chapter 3. The wave-rider results are also compared with particle velocities obtained from linear theory (superposition), the 2nd order formulation of Dean and Sharma, 1981 (as implemented in Kim, 2008) and the simplified analytical model of Grue et al

(2004). Furthermore, an attempt is made to explain the discrepancy between the analytical and Fluent simulation results, in terms of a surface current (section 5.5.1, figures 5.16 and 5.17) and wave-wave interaction (section 5.2.1).

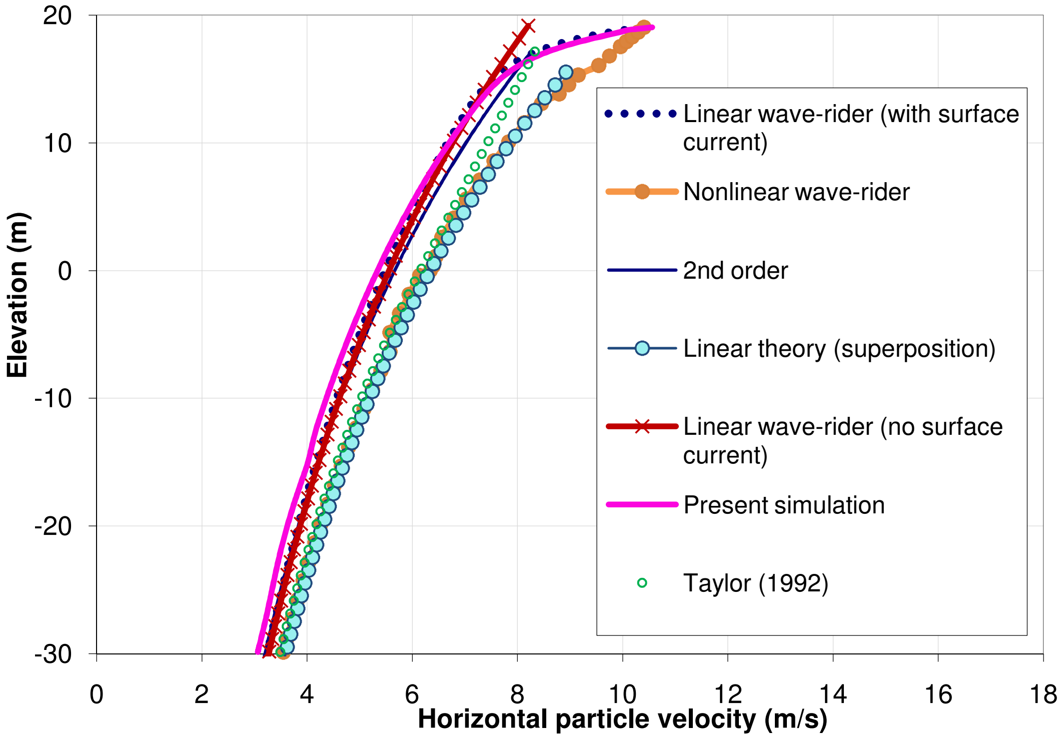

Figure 5.14: Horizontal particle velocity under extreme crest of most probable highest wave (surface current discussed in section 5.5.1)

Taking the simulation result as the correct one, the simplified analytical models are found to largely over-predict the horizontal particle velocities under the extreme crest of the most probable highest wave in the sea-state Hs=17.67m and Tz=13.4s. Only the wave-rider and 2nd order results (Dean and Sharma, 1981 cited in Kim, 2008) are in reasonable agreement although under-predicting at the very crest top. In the case of the most probable steepest wave investigated, only Grue's simplified method, linear theory (superposition) and the non-linear wave-rider method presented in section 5.3, gave results that were close to the Fluent simulation although the results were significantly less than the Fluent simulation results in the region around the free surface. In this region, none of the methods was able to match simulations and this is not surprising since the wave is just breaking.

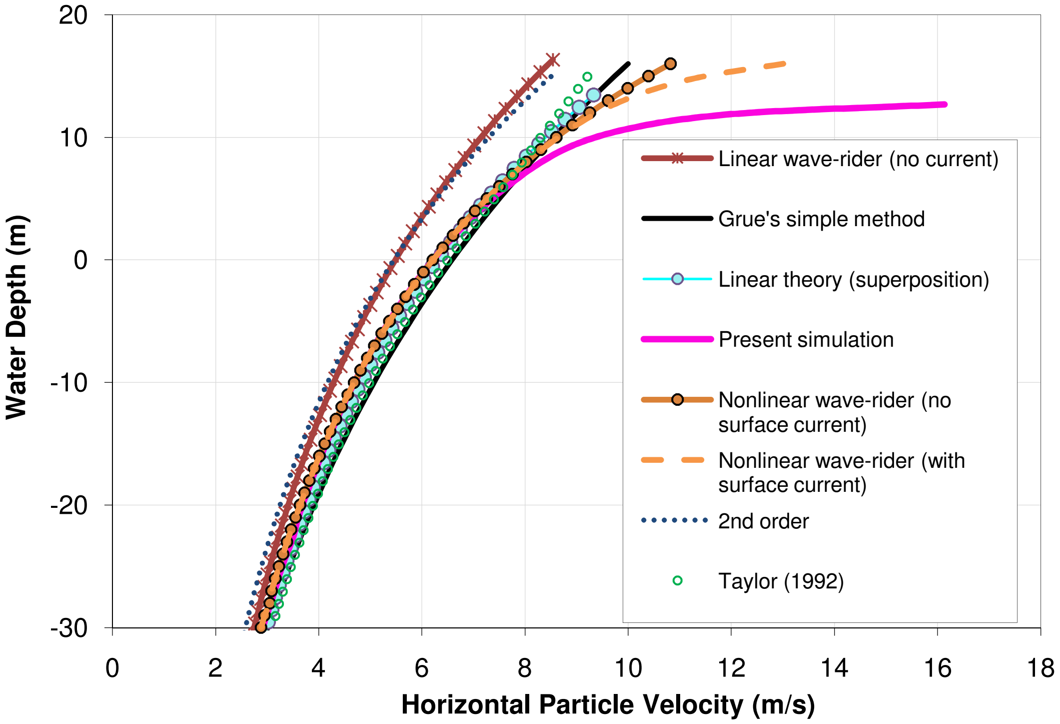

Figure 5.15: Horizontal particle velocity under extreme crest of most probable steepest wave (surface current discussed in section 5.5.1)

5.5 Some Theoretical rationale for the Observed Kinematics

The unusual behaviour of the kinematics of the extreme waves investigated is very interesting and it will be useful to have some understanding of why the kinematics are as observed. In this section, an attempt is made to explain the kinematics in terms of a surface current and simple wave-wave interaction. Although these do not constitute a comprehensive explanation of the phenomenon, they give useful indication at least in a qualitative sense, as to how and why this unusual behaviour arise.

5.5.1 Surface current

As shown in 5.4 above, there appears to be an extra current in the region close to the free surface which decays very rapidly with depth and is not accounted for by the wave-rider method or the 2nd order prediction. A conjecture is that this extra current is related to that noted in Longuet-Higgins (1986) where it was shown that the current is directly proportional to the amount δm by which the mean water level is lifted up due to vertical asymmetry and inversely proportional to the phase velocity of the wave. In the present case under investigation, it is assumed that δm is the average of the difference between the linear and nonlinear crest to trough height of the extreme event and that the current decays with depth according to e^{30kz}, where z is the depth and k is the notional wave-number obtained from the trough-to-trough length about the extreme event. By adding the so obtained current to the wave-rider predictions, values that are very close to the Fluent simulation in Chapter 3 is obtained. Note that the selection of e^{30kz} is purely empirical.

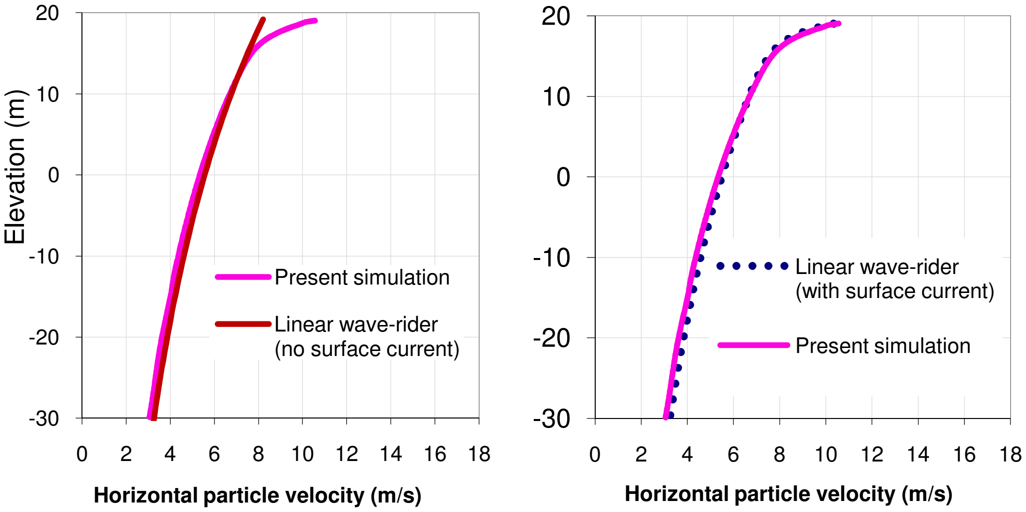

Figure 5.16: Inclusion of surface current in theoretical prediction of most probable highest wave Horizontal particle velocity.

A similar attempt with the most probable steepest wave showed some improvement but even with the addition of a surface current, the adapted 5th order new-wave approach which gave results closest to simulations still could not predict the very high velocities seen in the simulations.

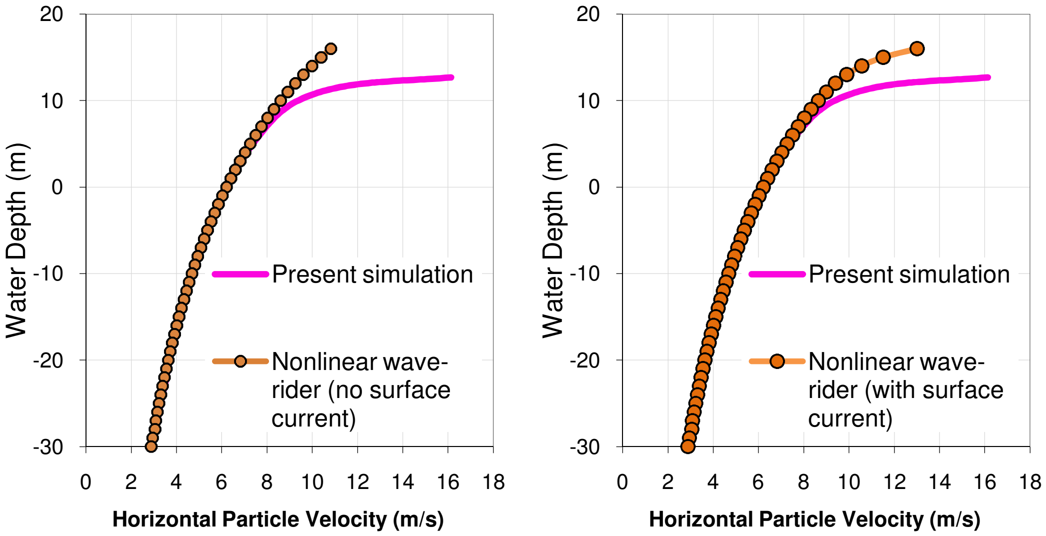

Figure 5.17: Inclusion of surface current in theoretical prediction of most probable steepest wave Horizontal particle velocity.

Notice that in contrast to the simulated highest wave velocity shown in figure 5.14, the nonlinear wave-rider is in good agreement with the steepest wave (breaking) kinematics in figure 5.17. At the moment, it is not clear why the linear and nonlinear wave-rider methods are only in agreement with the kinematics of the highest wave and steepest wave, respectively. This may be related to the dilemma of two disparate schools of horizontal particle velocity results highlighted in section 2.7.2 (table 2.1). Another thing to be observed in figure 5.17 is the crest of the simulated wave being lower than the 5th order new-wave prediction. Although the reason for this is also unclear, this has been noted previously where a plausible explanation was given that the high velocity stream of air above the wave crest is causing ‘positive-forcing’ of the wave crest and thus damping the crest height since the air-stream is in the same direction as the wave (Philips and Banner, 1974). However in the simulation, there is no fast moving wind so the effect of air above the water, if any, may be different.

Whereas the inclusion of a surface current improves the kinematics seen in the Fluent simulations, the failure of the surface current assumption in the most probable steepest wave case suggests that much more than that, there are other fundamental mechanisms at play which have not been taken into account by any of the present analytical models. This is understandable since the wave is just on the verge of breaking and severe wave-wave interactions cannot be ruled out. It is therefore useful to explore the relative effects of wave-wave interaction on the kinematics of the alternate extreme waves under investigation. It is pertinent to note that the concept of wave-wave interaction explored in the following section is in the context of weak non-linearity whereas wave-breaking is a strongly non-linear phenomenon (Rainey, 2007). Therefore the conclusions in the following discussion are only in a qualitative sense.

5.5.2 Wave-wave interaction

Unlike small and moderate waves, extreme waves are nonlinear and the interaction of spectral components is inevitable especially in the focusing of components to produce an extreme event. This interaction may be in the form of bound waves or tertiary waves resulting from third order resonant interaction (Gibson and Swan, 2006, Longuet-Higgins, 1961, Longuet-Higgins and Philips, 1962 etc).

5.5.2.1 Bound waves

The interaction is in the form of tertiary modes, phase-locked to the underlying components and is represented by the higher order terms in the perturbation expansion. Analytically, this is given by the long wave-short wave interaction of Longuet-Higgins and Stewart (1960) as a wave with amplitude equal to the amplitude of a short wave multiplied by the slope (ak) of the longer wave interacting with it.

Figure 5.18 shows the ratio of the slopes of the steepest wave spectral components to those of the highest wave spectral components. By definition, the higher-frequency Fourier components of the most probable steepest wave are steeper than those of the most probable highest wave although the reverse is the case for the lower-frequency components.

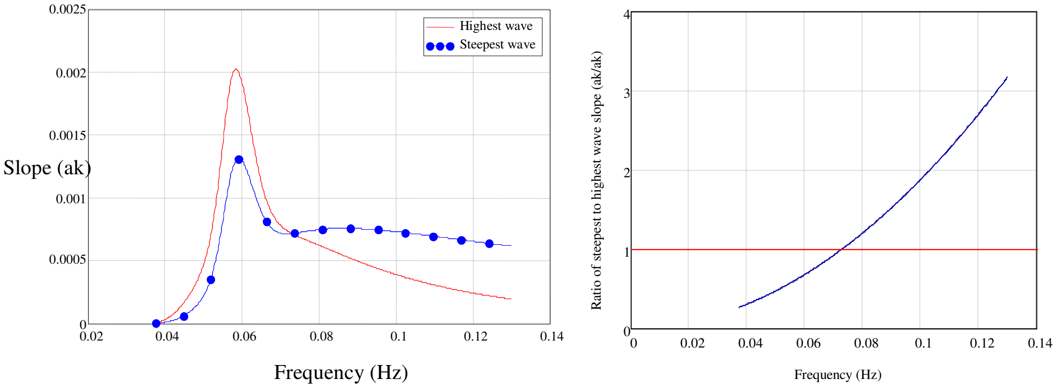

Figure 5.18: Slopes of the steepest wave and highest wave spectral components

The implication for a short wave interacting with a spectrum is that interaction with the lower frequencies of the steepest wave spectrum will result in bound waves that are smaller than the equivalent case of the highest wave spectrum. In contrast, interaction with the tail of the spectrum where slope (ak) is higher in the steepest wave than in the highest wave will result in higher bound waves. This means that the highest wave becomes higher (spectral peak frequency is in the low-frequency region). In contrast, the steepest wave crest is made steeper due to the high frequency interaction effect but is not as high as the highest wave.

This corresponds to the transfer of energy to the tail of the spectrum noted by Gibson and Swan (2006). However, the present discussion is in the context of the relative magnitude of this transfer with regard to the most probable steepest and highest wave spectra which are equivalent in terms of over-all energy, the only difference being the distribution of this energy in the initial spectra.

5.5.2.2 Resonant Interactions

Unlike in bound waves, resonant interactions result in both amplitude and phase changes. The implication is that the forced mode (due to resonant interaction) is not bound to the underlying component but is freely propagating (Gibson and Swan, 2006). Longuet-Higgins (1961) gives the amplitude of this tertiary wave resulting from the resonant interaction of two tertiary waves 1 (lower frequency) and 2 (higher frequency) at third order, in the form:

$$\boldsymbol{\zeta(t) = \frac{1}{2} a_1 k_1 a_2 k_2 a_1 \omega_1 t F(\xi)} \qquad \mathbf{5.5}$$

where $\zeta(t)$ is the amplitude of the forced/tertiary wave as a function of time, a is the amplitude , k is wave-number, ω is frequency and F is a function that depends on ξ where $\xi = \frac{\omega_2 - \omega_1}{\omega_1}$.

It turns out that the magnitude of the tertiary wave is dependent on the slopes (*ak*) of the two interacting primary waves and interestingly, the particle velocity contribution of the long primary wave ($a_1\omega_1$). It can thus be expected that in the steepest wave spectrum where $a_1\omega_1$ in the tail of the spectrum is larger than in the equivalent highest wave spectrum, the tertiary waves resulting from resonant interaction, will be relatively larger.

Resonant interactions also result in changes to the phase of the primary waves. Longuet-Higgins and Philips (1962) gives this phase change Δc_2 in a wave 2, due to its interaction with a longer and parallel wave 1 to third order, as a change in the phase velocity of wave 2 written as:

$$\boldsymbol{\Delta c_2 = a_1^2 k_1 \omega_1} \qquad \mathbf{5.6}$$

Assuming a constant rate of change of phase, a resulting change in frequency which represents the frequency of the forced mode can be written in line with Tanaka et al (2002) as:

$$\boldsymbol{\Delta\omega_2 = \Delta\mathrm{c}\, k_2} \qquad \mathbf{5.7}$$

This implies that:

$$\boldsymbol{\Delta\omega_2 = a_1 k_1 a_1 \omega_1\, k_2} \qquad \mathbf{5.8}$$

The frequency of the forced mode is dependent on the slope and particle velocity contribution of the primary long wave as well as the wave-number of the short wave interacting. It is obvious that this effect will be stronger in the tail of the spectrum and since the steepest wave has more energy in this region (a_1k_1 *and* $a_1\omega_1$ are greater) than in the equivalent highest wave, $\Delta\omega_2$ will be larger in the steepest wave. Figure 8.6 shows the ratio of $\Delta\omega_2$ in the steepest wave to that in the highest wave.

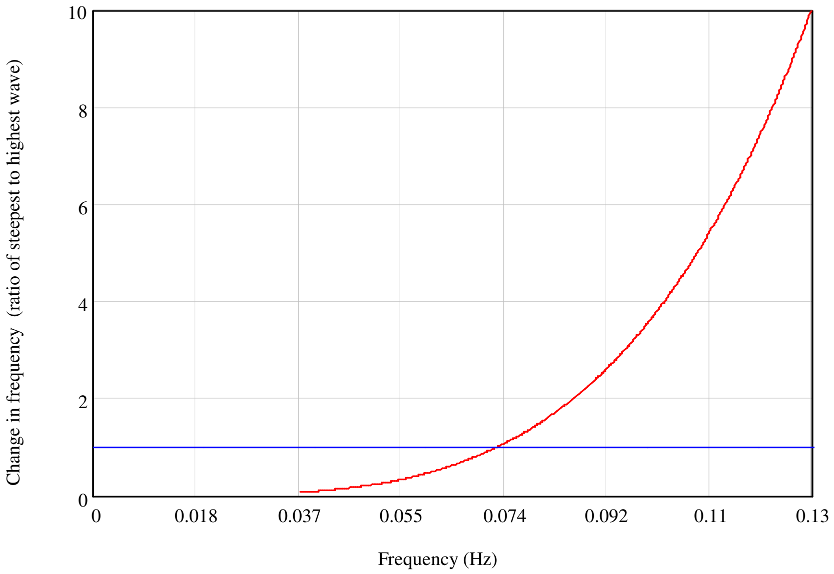

Figure 5.19: Relative (steepest to highest wave) resonant interaction in terms of change in the frequency of the spectral components.

The simple two wave resonant interaction shows that the frequency of the free wave generated as a result of interaction of a high frequency component with the lowest frequencies in the steepest wave spectrum can be as low as 6% of that in the equivalent highest wave spectrum. However, they are about equal when the long wave is about 1.25 of peak spectral frequency and for frequencies higher than this, $\Delta\omega_2$ increases exponentially to about a maximum of ten times the highest wave value at tail end of the steepest wave spectrum.

Since particle velocity is essentially amplitude multiplied by frequency and the tail of the steepest wave spectrum have higher amplitudes, it follows that the higher particle velocities will be seen in the most probable steepest wave than in the equivalent most probable highest wave. As a result, the steepest wave will be more severe due to wave-wave interaction, despite not being as high as the highest wave.

Similarly, the freely propagating tertiary waves which are higher in the steepest wave spectrum than in the highest wave spectrum, will be steeper due to a combination of high amplitudes and high frequencies. The implication on the overall wave-shape is that the steepest wave will not necessarily result in higher waves rather, it will lead to very high steepness localized at the wave crest and if the sea-state is sufficiently high will go on to break. The figure below compares the most probable steepest wave and highest (scaled to be equivalent) that are breaking in the indicated sea-states.

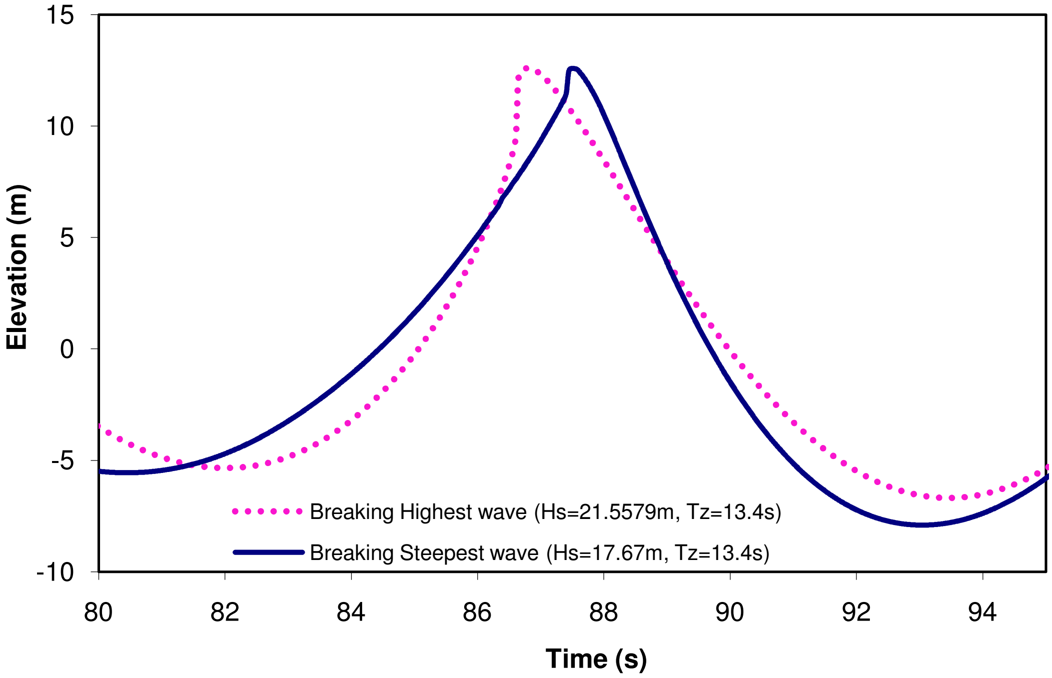

Figure 5.20: Comparison of the temporal shape of a breaking highest (traditional extreme) wave with a breaking steepest (alternative extreme) wave.

It is obvious that the breaking highest wave is steeper in the usual sense of the word but the steepness in the steepest wave seems to be a localized (perhaps high frequency) sharpening of the crest of the type described earlier. This is further illustrated in the snap-shot of the two waves at breaking shown in figure 5.21.

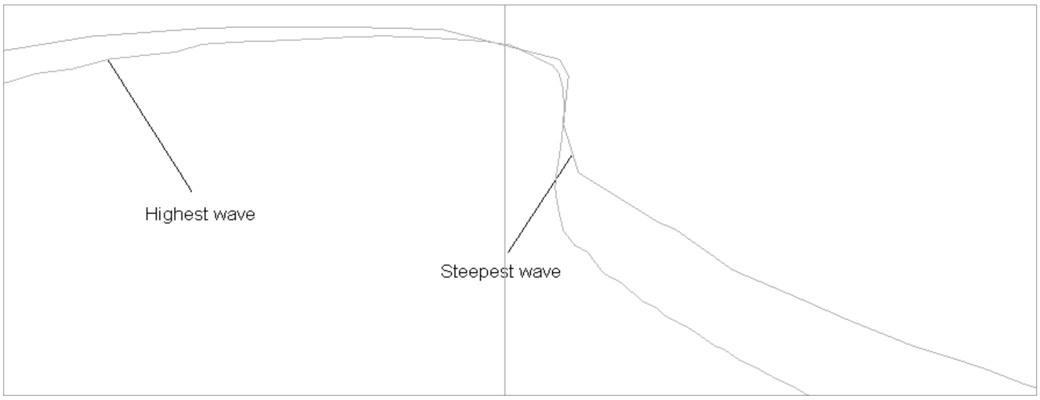

Figure 5.21: Comparison of the spacial shape of a breaking highest (traditional extreme at 76.2s: H_s=21.56m, T_z=13.4s) wave with a breaking steepest (alternative extreme at 87.5s: H_s=17.67m, T_z=13.4s at 87.5s) wave. The traditional extreme has been scaled down to match the alternative extreme.

Although both waves are breaking, the nature of the event/mechanism leading up to each one is different. Apparently, the breaking highest wave above will be more severe than the steepest wave but given a most probable highest wave in the same sea-state as the steepest wave and appropriate sea-state such as is in figure 8.7 above, the steepest wave will be more severe as has been shown in Chapter 3.

6 Implications of Observed Kinematics

Having demonstrated the viability of the developed analytical kinematics models and established the nature of the kinematics in extreme waves using a fully non-linear viscous flow solver; a demonstration of the influence of this observed kinematics on loading and by extension response, will be attempted in this section. A robust nor comprehensive time-domain modelling of the loads and resulting structural response is not intended rather, a comparative (highest versus steepest wave) analysis will be done for various components of the loading and structural response algorithm/procedure with the focus on the relative influence of the highest and steepest waves at each stage.

6.1 Implications on a fixed structure

In order to better illustrate the implications of the observed particle kinematics, it is useful to look at the Morison equation.

$$F = 0.5 C_d \rho D |U| U + C_m \rho A \frac{\partial U}{\partial t} \qquad 6.1$$

Obviously, the Morison force is dependent on particle velocities and accelerations which underscore the need for an understanding of the kinematics of extreme waves.

6.1.1 Implication of convective acceleration

Notice that in equation 6.1 which is the usual form used in routine analysis, the convective component of particle acceleration is ignored. As mentioned earlier, the convective component is of the same order of magnitude as the local component of acceleration in extreme waves. Therefore, total (local plus convective) acceleration is used in the present study. In practice, convective acceleration is not very important for fixed structures since in steep waves where convective acceleration is usually considerable, inertial forces on slender bodies are much lower than drag and slam forces. Even in large-volume structures which are usually in the form of vertical caissons, convective acceleration may be ignored since the main wave-load is a horizontal inertial load and it has been shown that convective acceleration in this direction is negligible. Indeed, API RP 2A-LRFD (C.3.2.10) argues that convective acceleration is negligible due to flow separation in a member's wake and recommends that it should be ignored. This was in the context of slender bodies subject to horizontal wave-loading. Although there has been a long running debate about this, results of the present work (figure 3.19) shows that even in the absence of flow obstruction, convective horizontal particle acceleration is negligible in breaking and non-breaking waves. This suggests that the "flow-separation" argument in API RP 2A-LRFD (C.3.2.10) may not adequately explain the virtual absence of convective acceleration in the horizontal direction. In the vertical direction, convective acceleration is quite considerable as shown in figure 3.17 where convective acceleration is opposite in direction but similar in magnitude compared to the local acceleration. Thus, the API recommendation to ignore convective acceleration seems appropriate for vertical members but not necessarily valid for horizontal members.

6.1.2 Relative significance of the steepest and highest wave.

To illustrate the implications of the kinematics observed in the steepest and highest waves, a hypothetical slender vertical surface piercing cylinder with diameter D=1m, drag coefficient C_d =1 and added-mass coefficient C_m =1; is subjected to both kinds of extreme waves and the resulting drag and inertial loads investigated. In the following analysis, the maximum particle kinematics along the water column at the position of maximum kinematics (x=253m for steepest wave and x=135m for highest wave) is used to calculate the max induced load and is shown in figure 6.1.

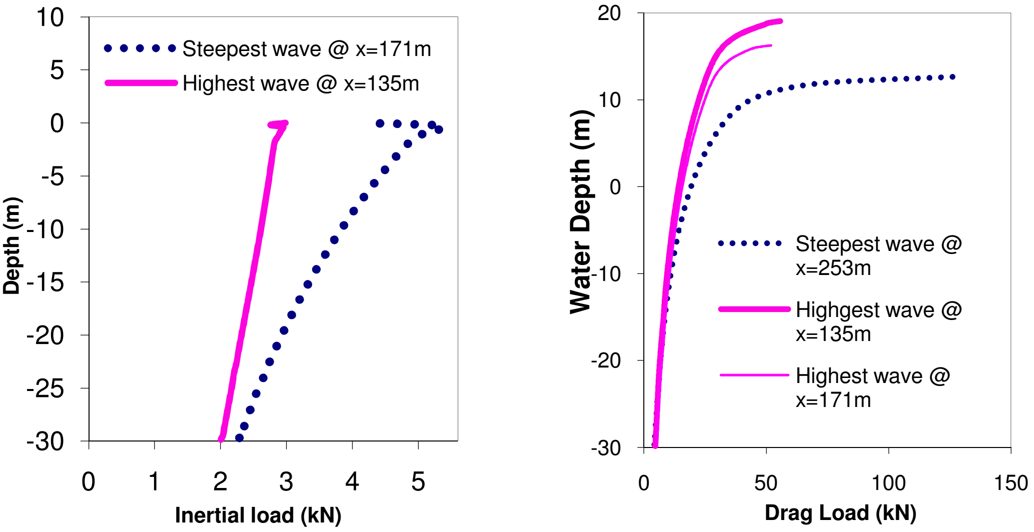

Figure 6.1: Maximum horizontal loads (H_s=17.67m, T_z=13.4s, JONSWAP peakedness parameter=2).

In the light of the fact that not much attention has been given to this alternative extreme (most probable steepest) wave, it is remarkable that the load induced by it is generally greater than that induced by the traditional extreme (most probable highest wave). In terms of the global horizontal force (Morison equation) exerted by the two extreme waves down to a depth of 30m (below which differences in kinematics is very small), the steepest wave's pressure is greater by 111.95 kN/m^2 which is about 2.6%. More interesting is that the maximum pressure exerted (near the crest top) by the steepest wave is about 2.6 times that exerted by the highest wave. This suggests that panels in this region should ideally be designed to withstand about 3 times the load it would be designed for using the traditional new-wave as a design wave. Since the load varies with height and the steepest wave is not as high as the highest, a more rigorous comparison of the severity of both extreme waves will be on the basis of their consequent overturning moment. With the assumption that the bottom-fixed structure is stiffness dominated, the overturning-moment at various points along the height/length of the structure is calculated and presented in figure 6.2.

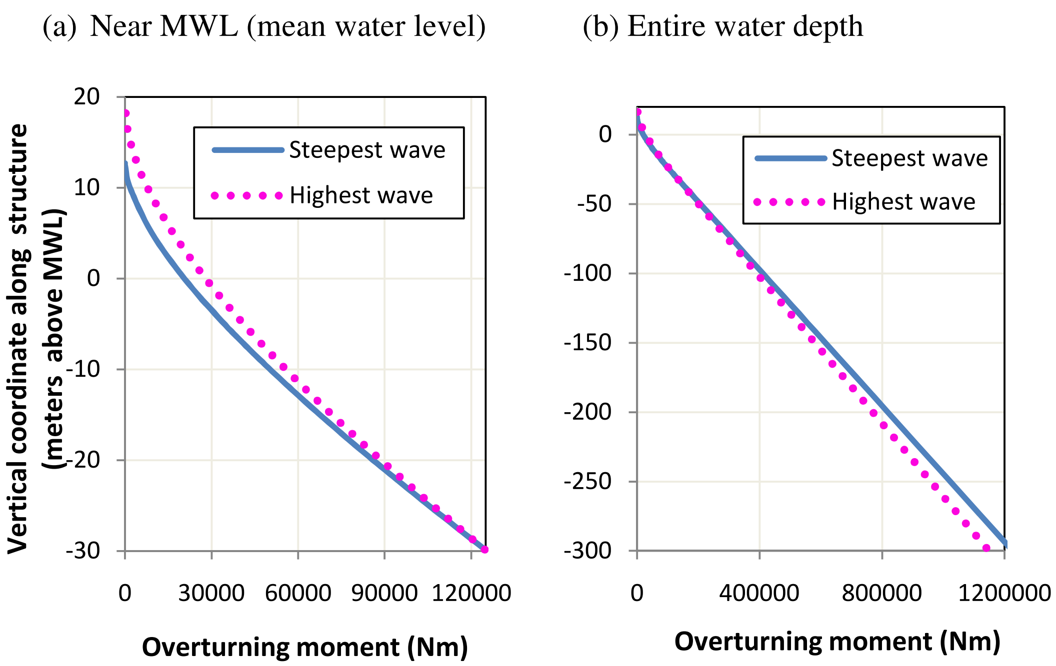

(a) Near MWL (mean water level) (b) Entire water depth

Figure 6.2: Variation of extreme wave-induced bending moment along the bottom-fixed structure (Hs=17.67m, Tz=13.4s, JONSWAP peakedness parameter=2).

It can be seen that although the steepest wave is not as high and its lever arm is shorter, the loads exerted in the region of the crest is so severe that the consequent bending moment at most points (far below MWL) on the structure, is higher than those due to the highest wave. Ironically, bending moments due to the highest wave is larger around MWL. The implication is that in terms of global bending, the design of a bottom-fixed mono-cylindrical structure such as is analysed herein will be governed by the traditional extreme wave in the region around MWL whereas bending stresses in parts of the structure well below MWL and the over-all overturning moment at the sea-bed will due to the alternative extreme wave. Thus, design for such a mono-cylindrical structure is not just a simple matter of selecting a single design wave rather; such a structure should be designed to withstand several load cases defined by the traditional as well as the alternative extreme wave.

In practice, many offshore structures have multiple legs and the plan distribution of the high particle kinematics also becomes important. Thus, the high particle kinematics in steep waves may only affect part of the structure at a time and result in less important global forces although dominating local forces.

6.2 Implication on a floating structure

Although, impact loads and Hull-girder bending responses were recorded in the extensive investigation of Xu (2006), the underlying kinematics of the extreme waves were not measured. Since the kinematics are undoubtedly non-linear but yet unclear, it became difficult to demonstrate the relative effects of the alternate extreme waves by a purely theoretical means. Apparently, the kinematics needed to be established as a foundation for a rational theoretical simulation. As a result, this work has focused on kinematics and in this section; it is aimed to theoretically demonstrate (albeit simplistically) the relative implications of the observed kinematics in the context of wave-loads exerted on a simple rectangular barge at the instant of the extreme event.

6.2.1 Strip theory Fundamentals

Since the focus is on the relative severity of the alternate extreme waves (rather than an absolute magnitude), it is expected that in conjunction with the water particle kinematics obtained from the viscous flow simulations in Chapter 3, a simple linear strip theory calculation will suffice in giving an indication of the relative magnitudes of the loads induced by the traditional and alternative extreme waves. At this point, it is useful to note that the non-linearities inherent in hull-girder response to extreme waves are mostly related to kinematics (here obtained from a fully nonlinear simulation) and the variation of the instantaneous immersed area of hull section which affects the rate of change of added-mass. Based on the non-linear external hydrodynamic load *(*equation *6.2)* given by Xia et al (1998), it can be seen that this effect of change of added mass is relevant to the slamming $\frac{\partial \bar{\mathrm{m}}}{\partial \bar{\mathrm{z}}}(\frac{\mathrm{D}\bar{\mathrm{z}}}{\mathrm{Dt}})^2$ effect. Therefore, if slamming and memory effects are neglected as in the usual quasi-static wave loading, the use of linear strip theory with fully non-linear kinematics seems a reasonable approach at zero forward-speed for the comparative analysis of wave-loads induced by alternate extreme waves.

$$\mathrm{z(x,t)} = -\bar{m}\frac{\mathrm{D^2\bar{z}}}{\mathrm{Dt^2}} + \mathrm{U}\frac{\partial \bar{\mathrm{m}}}{\partial \mathrm{x}}\frac{\mathrm{D\bar{z}}}{\mathrm{Dt}} - \frac{\partial \bar{\mathrm{m}}}{\partial \bar{\mathrm{z}}}(\frac{\mathrm{D\bar{z}}}{\mathrm{Dt}})^2 - \frac{\mathrm{Dq_J}}{\mathrm{Dt}} + \rho g S \qquad 6.2$$

$\bar{m}$ is added-mass, $\bar{z}$ is relative motion, U is forward speed, $\rho g S$ is the instantaneous buoyancy, $\frac{\mathrm{Dq_J}}{\mathrm{Dt}}$ represents memory effects and $\bar{m}\frac{\mathrm{D^2\bar{z}}}{\mathrm{Dt^2}}$ is the added-mass (a notional force added to account for disruption of flow by the immersed body).

In the strip theory, the hull is assumed slender-bodied so that it can be idealized as a series of cross-sectional slices or strips the dynamics of which can be represented by the classical equation of motion of a simple mechanical system.

$$F(t) = M\ddot{z}(t) + C\dot{z}(t) + Kz(t) \qquad 6.3$$

The right hand side of the equation being the resisting force with *M, C, K, z(t)* and over-dot representing mass (vessel displacement plus added masses) , damping (radiated waves), stiffness (water plane), time varying response (motion) and differentiation with respect to time respectively. This interaction is illustrated in Barltrop (1998) as shown in figure 6.3 with the assumption that the hull-girder is stiffness dominated.

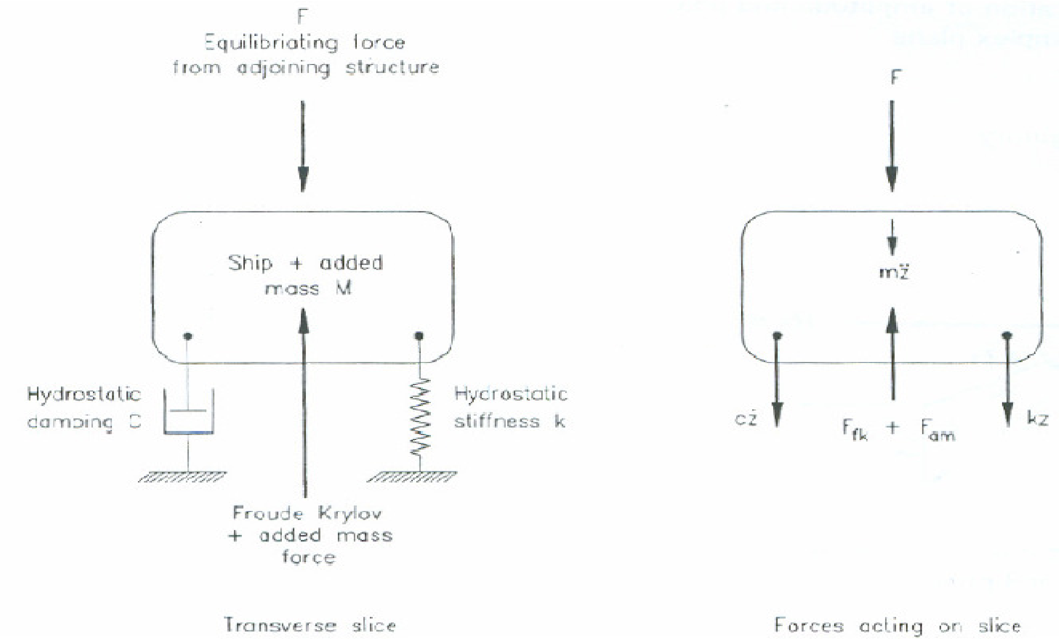

Figure 6.3: Net force per unit length of vessel, acting on each slice/strip.

On the left hand side of equation *6.3, F(t)* is the exciting force primarily composed of the Froude-Krylov force and added-mass force. Any net force from the balance between the exciting and resisting forces on each strip will be the contribution of the slice to the shear force at the section. Since the present focus is on loading, the following discussion will be restricted to the forcing term, *F(t)*.

6.2.2 Vertical exciting force

6.2.2.1 Froude-Krylov Force

As explained earlier, the Froude-Krylov force is the net pressure exerted by the undisturbed wave on the bottom of the hull. This is obtained from the viscous flow simulation in Chapter 3 by plotting the profile of total pressure (with hydrostatic pressure subtracted) under the extreme crest.

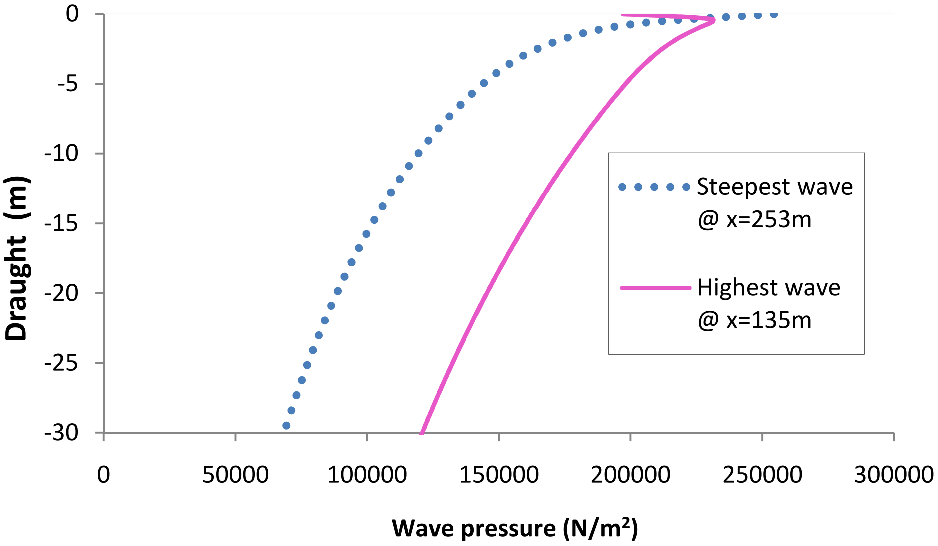

Figure 6.4: Undisturbed wave pressure under the extreme crest.

To facilitate calculation of vertical wave loads at 12m and 20m draughts, Froude-Krylov force is taken as the total pressures at these draughts and presented in table 6.1.

6.1: Total pressure in undisturbed wave (N/m^2)

Draught	*Highest wave*	*Steepest wave*
12m	169,910.1	111,432.7
20m	145,005.7	88,171.38

For the discussion on the significance of convective acceleration in section 6.2.4, the vertical profile of the relevant pressures are obtained from the viscous flow simulation in Chapter 3 and presented in figure 6.5.

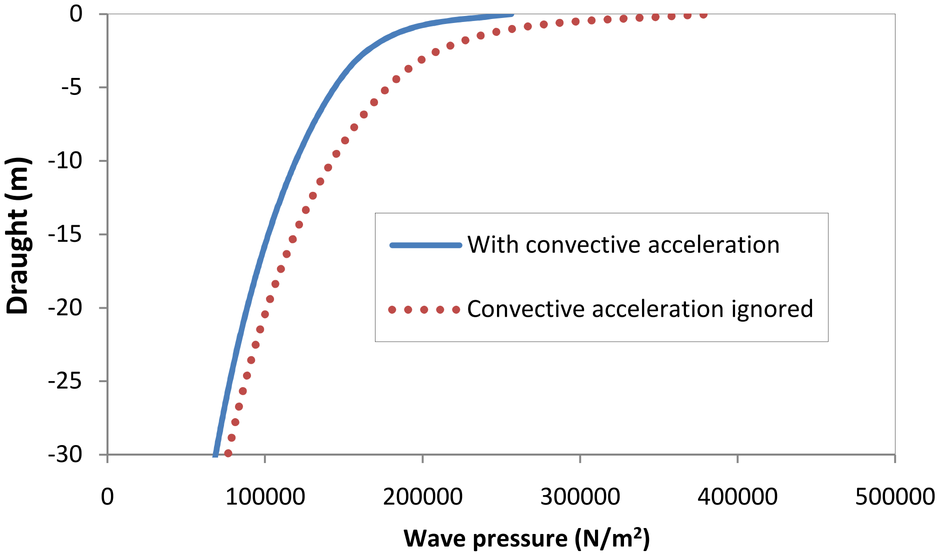

Figure 6.5: Undisturbed pressure under the extreme crest of the steepest wave.

To check the significance of convective acceleration in vertical wave loads at 12m and 20m draughts, Froude-Krylov forces at these draughts are taken as the pressures in figure 6.5 and presented in table 6.2.

Table 6.2: Calculated undisturbed pressure (N/m^2) in the steepest wave

Draught	*Total*	*Ignoring convective acceleration*
12m	111,432.7	131,405.45
20m	88,171.38	100,757.28

6.2.2.2 Added-mass force

The presence of the floating body will generally disrupt the flow in a wave-field. This is simplistically modelled as an additional mass of water trapped by the body and moving with the body. The effect is thus calculated as a force F_{am} required to accelerate this additional mass.

$F_{am} = a_3\ddot{x}_{fluid}$ (a_3 is the added mass and $\ddot{x}_{fluid}$ is the water particle acceleration)

6.2.3 Implication of Observed Kinematics on Quasi-static Vertical Wave-loading.

Assuming a simplistic rectangular wall-sided barge with D_m=27m, B=45m, L=245m, the vertical loads induced by the alternate extreme waves is obtained below for draughts of 12m and 20m, at the instant of the extreme event. The added-mass in units of kg/m^2 is obtained as $a_3 = \rho(\frac{\pi}{8})BC_c$ with C_c read from Grim's , 1959 chart (cited in Bergdahl, 2005).

Table 6.3: Added-mass per unit length of hull (based on Grim, 1959 as cited in Bergdahl, 2005) in sea-state H_s=17.67m, T_z=13.4s, JONSWAP peakedness parameter =2.

Draught (m)	*Traditional extreme wave (kg/m^2)*	*Alternative Extreme wave (kg/m^2)*
12m	16 581.6	15 523.2
20m	16 228.8	15 876

To facilitate comparison of the two extreme waves, they are treated as regular waves with period equivalent to the trough-to-trough period about the extreme event. Based on this period, frequency and wave-number (linear dispersion) is defined and used in the strip theory calculations done for only the instant of the extreme event.

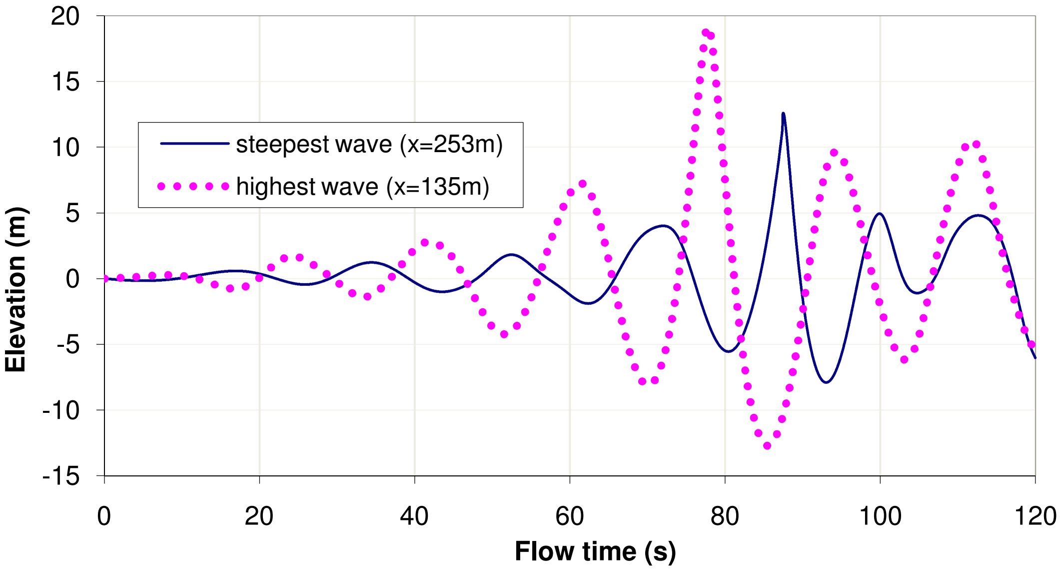

Figure 6.6: Time history of the alternate extreme waves (H_s=17.67m, T_z=13.4s, JONSWAP peakedness parameter=2)

From the time history in figure 6.4, trough-to-trough periods of 12.6s and 15.4s are extracted about the extreme event for the alternative (steepest) and traditional (NewWave / highest) extreme waves respectively. Thus the notional wave-numbers are:

$$K_s = \frac{4\pi^2}{gT^2} = \frac{4\pi^2}{g12.6^2} = 0.025\ \frac{1}{m} \qquad \text{for the alternative extreme (steepest) wave}$$

$$K_h = \frac{4\pi^2}{gT^2} = \frac{4\pi^2}{g15.4^2} = 0.017\ \frac{1}{m} \qquad \text{for the traditional extreme (highest) wave}$$

Water particle acceleration is obtained from the viscous flow simulation in Chapter 3 (figure 3.14) and Froude-Krylov forces from table 6.1.

6.2.3.1 Traditional extreme wave at 12m draft.

$F_{KR}+F_{am} = 169{,}910.1\ \frac{N}{m^2} + a_3\ddot{x}_{fluid} = 169{,}910.1\ \frac{N}{m^2} + \left[16581.6\frac{kg}{m^2} *\right.$

$-2.58353ms2 = (169{,}910.1\ -\ 42{,}839.061)\ Nm2\ = 127{,}071.039\ Nm2$

6.2.3.2 Alternative extreme wave at 12m draft

$F_{KR}+F_{am} = 111{,}432.7\ \frac{N}{m^2} + a_3\ddot{x}_{fluid} = 111{,}432.7\ \frac{N}{m^2} + \left[15523.2\frac{kg}{m^2} *\right.$

$-2.2286ms2 = (111{,}432.7 - 34595.0)\ Nm2 = 76{,}837.7\ Nm2$

6.2.3.3 Traditional extreme wave at 20m draft.

$F_{KR}+F_{am} = 145{,}005.7\ \frac{N}{m^2} + a_3\ddot{x}_{fluid} = 145{,}005.7\ \frac{N}{m^2} + 16228\frac{kg}{m^2} *$

$\left(-2.30371\frac{m}{s^2}\right) = (145{,}005.7\ \frac{N}{m^2} - 37{,}384)\frac{N}{m^2}\ = 107{,}621.7\frac{N}{m^2}$

6.2.3.4 Alternative extreme wave at 20m draft

$F_{KR}+F_{am} = 88{,}171.38\frac{N}{m^2} + a_3\ddot{x}_{fluid} = 88{,}171.38\ \frac{N}{m^2} + 15876\frac{kg}{m^2} *$

$\left(-1.69568\frac{m}{s^2}\right) = (88{,}171.38\text{- }26{,}920.61568)\frac{N}{m^2}\ = 61{,}250.76\frac{N}{m^2}$

6.2.4 Comparison of Vertical Exciting Forces

Although the alternative extreme wave has the most severe particle kinematics, this is largely near the free surface and severity of water particle acceleration reduces more rapidly with depth than in the traditional extreme wave. Therefore at the drafts calculated, added-mass force which counteracts the Froude-Krylov force in partially submerged bodies is less in the alternative extreme wave. Notwithstanding, the total exciting vertical force on the bottom is dominated by the Froude-Krylov force. As a result the traditional extreme wave (which is higher than the alternative extreme) is more severe in terms of the usual vertical wave-load on the bottom of a ship-shaped structure in deep water.

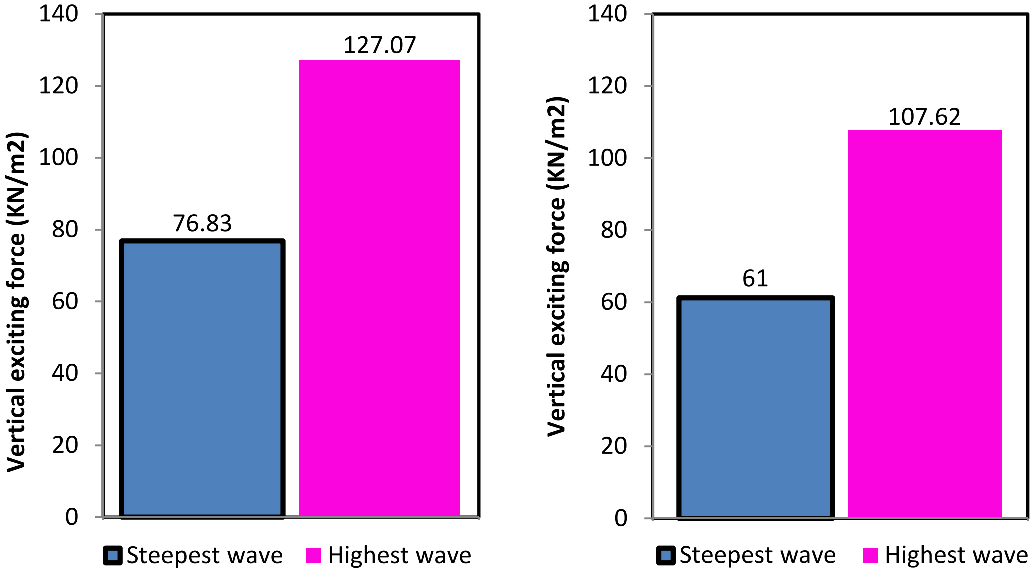
(a) 12m draught

(b) 20m draught

Figure 6.7: Average vertical exciting force per unit area of bottom plating (H$_s$=17.67m, T$_z$=13.4s, JONSWAP peakedness parameter=2)

Generally, the vertical inertial load due to the traditional extreme wave is almost twice those of the alternative extreme wave. The implication is that in terms of global vertical response, the traditional extreme wave is a more appropriate extreme for design.

6.2.5 Effect of Convective Acceleration

When convective acceleration is treated consistently in the Froude-Krylov and added-mass forces, inclusion of convective acceleration or otherwise has negligible effect on the overall vertical wave-loading on partially submerged bodies. This is understandable since in this situation, Froude-Krylov force and added-mass force act in opposite directions which means that the loading is based on the relative (rather than absolute) magnitudes of the two components. Therefore when acceleration is treated consistently in both components, inclusion of convective acceleration or otherwise will affect the two load components to the same relative extent thereby resulting in no net effect.

In practice (conventional strip theory), temporal and convective acceleration are implicit in the Froude-Krylov force (obtained directly from pressure integration) whereas it is usual to obtain added-mass force which is more explicitly dependent on acceleration in the strip theory, by multiplying added-mass with particle acceleration so that the neglect of convective acceleration will normally affect only the added-mass force. The result is that in a ship-shaped marine structure for example (partially submerged) where Froude-Krylov force and added-mass force are in opposition, ignoring convective acceleration in the added-mass force will result in slightly higher upward forces on the bottom of the structure when the wave-crest is passing. To illustrate this, the simplistic linear diffraction/strip theory calculation done for the alternative extreme wave in 6.2.3 is repeated here for two cases:

1) When convective acceleration is neglected (local acceleration)
2) When convective acceleration is included (total acceleration).

6.2.5.1 Local acceleration.

At 12m draught :

$F_{KR}+F_{am} = 111{,}432.7\frac{N}{m^2} + a_3\ddot{x}_{fluid} = 111{,}432.75\frac{N}{m^2} + \Big[15523.2\frac{kg}{m^2} *$

$-3.525975ms2$ = ($111{,}432.7$– 54,734.415) $Nm2$ = 56,698.285 $Nm2$

At 20m draught:

$F_{KR}+F_{am} = 88{,}171.38\frac{N}{m^2} + a_3\ddot{x}_{fluid} = 88{,}171.38\ \frac{N}{m^2} + 15876\frac{kg}{m^2} *$

$\left(-2.3758\frac{m}{s^2}\right) = (88{,}171.38 - 37{,}718.2)\frac{N}{m^2} = 50{,}999.18\frac{N}{m^2}$

6.2.5.2 Total acceleration.

At 12m draught :

$F_{KR}+F_{am} = 111{,}432.7\frac{N}{m^2} + a_3\ddot{x}_{fluid} = 111{,}432.7\frac{N}{m^2} + \Big[15523.2\frac{kg}{m^2} *$

$\left(-2.2286\frac{m}{s^2}\right)\Big] = (111{,}432.7 - 34{,}595.0)\frac{N}{m^2} = 76{,}837.7\frac{N}{m^2}$

At 20m draught:

$$F_{KR}+F_{am} = 88{,}171.38\frac{N}{m^2} + a_3\ddot{x}_{fluid}$$

$$= 88{,}171.38\frac{N}{m^2} + 15876\frac{kg}{m^2} * \left(-1.69568\frac{m}{s^2}\right) = (88{,}171.38 - 26{,}920.61568\ )\ \frac{N}{m^2}$$

$$= 61{,}250.76\ \frac{N}{m^2}$$

6.2.5.3 *Comparison of resulting loads.*

Results of the above calculation in 6.2.5.2 are summarized below in figure 6.8. It is found that at a draught of 20m (in the specific case above), the load under the bottom of hull calculated with the real (total) water particle acceleration is about 17% higher than that obtained with the apparent (local/temporal) acceleration. At 12m draught, this increases to 26% and is in line with the fact that wave-loads are higher at shallower draughts.

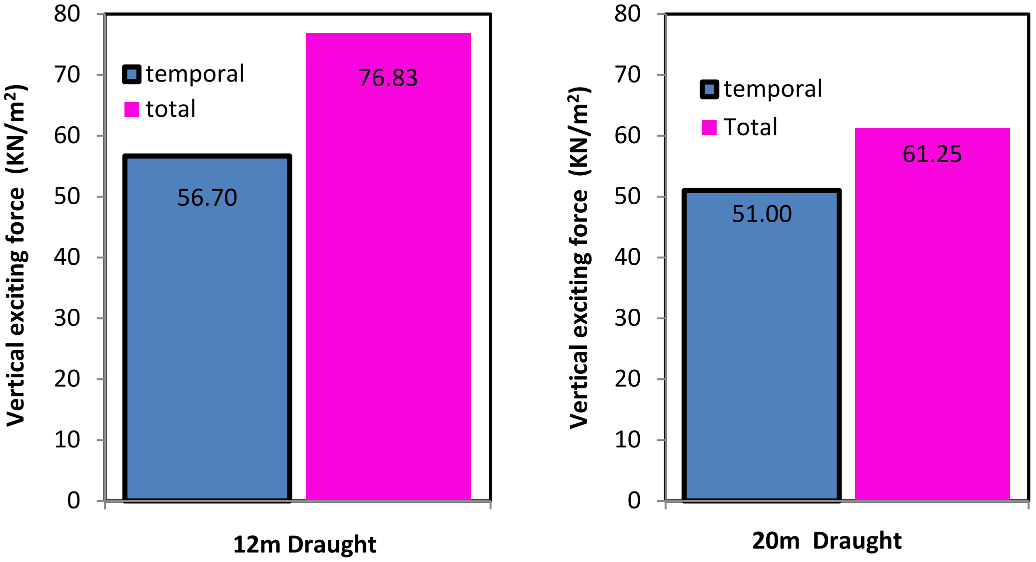

Figure 6.8: Difference in the vertical Loads based on apparent (local) and real (total) water particle acceleration.

Although the above analysis is somewhat simplistic, it is reasonable to conclude that the use of only the local/temporal particle acceleration will result in under-estimation of vertical wave-loads on floating (large partially submerged) structures.

For example, quasi-static wave-loads in conventional strip theory (e.g equation *6.2*) is essentially based on an exciting force given as the product of the mass (structural, m and added, $\tilde{m}$) and the second derivative of the relative motion (structure's rigid body, *w* less water surface motion, ζ).This pre-supposes that vertical particle acceleration $\dot{W}$, may be given simply as the apparent (local or temporal) acceleration with the convective contribution neglected:

$$\dot{W} = \frac{\partial W}{\partial t} = \frac{\partial}{\partial t}\left(\frac{\partial \zeta}{\partial t}\right) \qquad \mathbf{6.10}$$

In the light of the observation that the convective contribution is not negligible in extreme waves, it is desirable to include the effect of convective acceleration in the the strip theory. Some authors (e.g Xia et al, 1998) have used the substantive derivative in calculating the acceleration in the added-mass force. In this work, it is proposed to simply include an additional added-mass force, F in the forcing term of the conventional strip theory where only a temporal/local acceleration had been used.

$$\mathbf{F} = \tilde{\mathbf{m}}\left(\mathbf{U}\frac{\partial W}{\partial x} + W\frac{\partial W}{\partial Z}\right) \qquad \mathbf{6.11}$$

This is with the assumption that the convective acceleration is implicit in the Froude-Krylov force which has been obtained directly from a good pressure integration.

6.2.6 Transient Wave-loading.

For transient/impulsive responses (which may be more relevant for the local structure and fatigue life of local details), the steepness of the alternative extreme wave suggests a rapid rate of change of added-mass and therefore higher and localized impulsive loads. This is seen by representing the load as the rate of change of momentum of the water.

$$\frac{\mathbf{dmv}}{\mathbf{dt}} = \mathbf{m}\frac{\partial \mathbf{v}}{\partial \mathbf{t}} + \mathbf{v}\frac{\partial \mathbf{m}}{\partial \mathbf{t}} \qquad \mathbf{6.12}$$

Where v is the relative velocity between water and structure and m is the added-mass. Unlike the vertical rigid-body velocity (e.g combined heave-pitch temporal variation) whose effect on vertical loading may be considerable, horizontal rigid-body velocity of a ship-shaped structure (e.g roll, sway and yaw temporal variation) may be neglected in the face of a sudden appearance of an extreme and perhaps breaking beam wave (rogue beam sea). For the convenience of avoiding the calculation of vessel motions, transient wave-loading is examined here in the context of horizontal loading in beam sea with rigid body motions ignored. In such a situation, v is simply the horizontal water particle velocity and m is the added-mass in sway. At the instant of the extreme wave event, the crest is just passing and the $\frac{\partial \mathrm{v}}{\partial t}$ term tends to zero so that the impact load on the side shell is essentially v $\frac{\partial m}{\partial t}$. The rate of change of horizontal added-mass calculated with $m = \rho\left(\frac{\pi}{8}\right)T(t)C_c$ where *T(t)* is the instantaneous draft calculated as if there is no vertical motion and is thus obtained from surface elevation time-history obtained in Chapter 3.

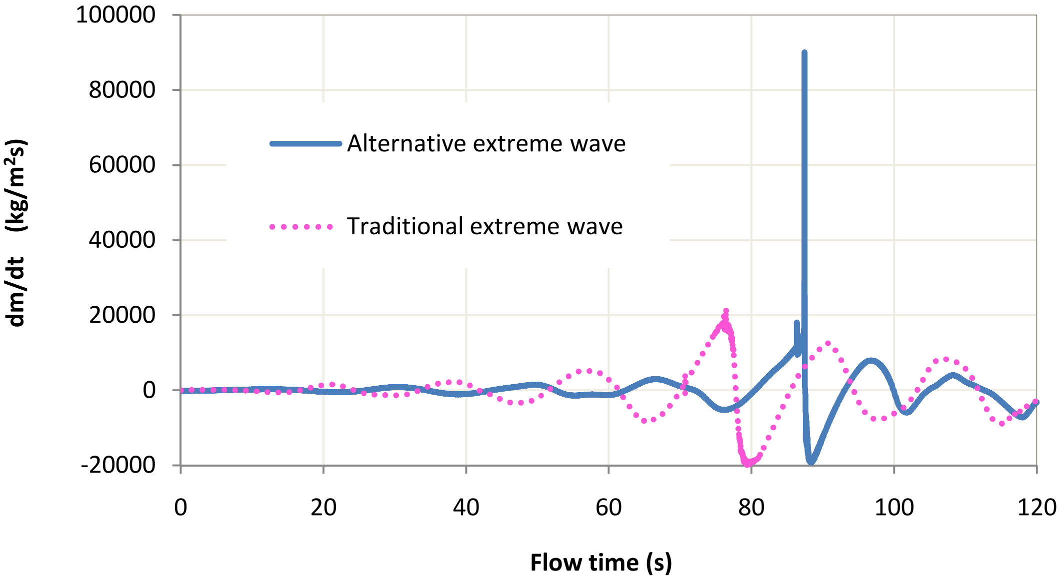

Figure 6.8: Time history of the rate of change in horizontal added-mass $\frac{dm}{dt}$ (H_s=17.67m, T_z=13.4s, JONSWAP peakedness parameter=2)

The time-history of $\frac{dm}{dt}$ in figure 6.7 suggests that the impact force exerted by the alternative extreme wave is several times more than that due to the traditional extreme wave and the well known (Smith, 2007) pressure spike in wave-impact events can be seen. This spike will be even higher if the time-history of v is applied and is evidenced by the fact that free-surface *v* compared at the instant of the extreme event is about 43% higher in the steepest wave as was shown in chapter 3.

However time-history of v at various depths (v varies with depth) are not available in order to calculate v $\frac{\partial m}{\partial t}$. Therefore, let it suffice to use depth profile of v recorded at the instant of the extreme event, in which case a depth profile of the peak impact load is obtained as shown in figure 6.8.

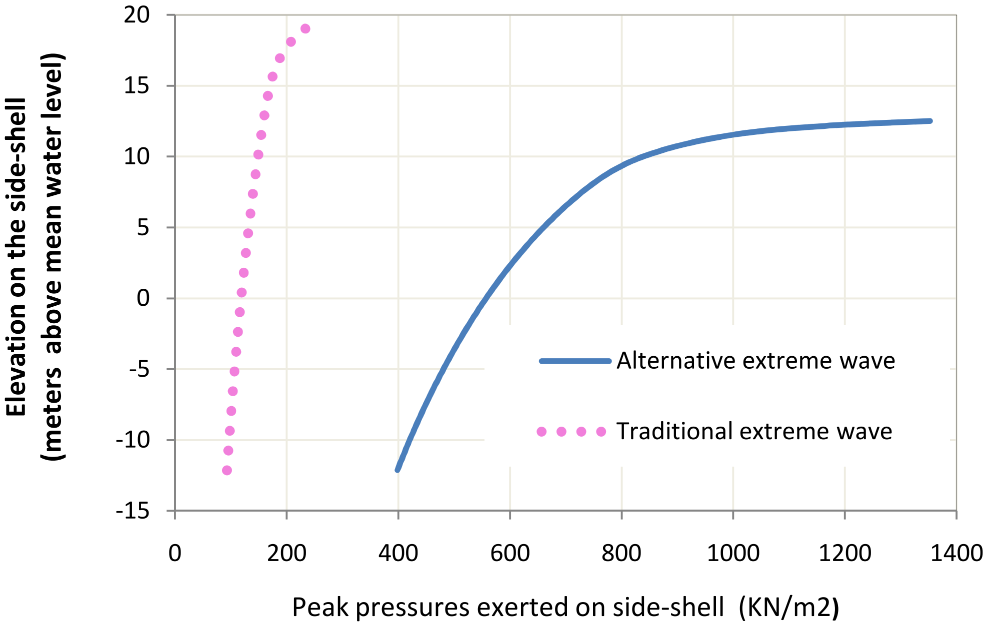

Figure 6.9: Peak horizontal impact pressure exerted on side-shell in beam seas (H_s=17.67m, T_z=13.4s, JONSWAP peakedness parameter=2) with rigid-body motions ignored.

It is interesting to see in figure 6.8 that the peak pressure exerted by the alternative extreme wave on a hypothetical side-shell is several times more than in the traditional extreme wave. Although the inclusion of vessel motions can alter these impact pressures, it was suggested in section 6.2.3 that these motions are much less in the alternative waves. Therefore it is expected that vessel motions will not have a major impact on the pressures induced by the alternative extreme wave which is up to five times more severe than that of the traditional extreme wave at the free surface. This leads to the reasonable conjecture that a ship designed with the traditional extreme wave as the design-wave while being able to survive ‘all’ weather in head-seas may in beam seas, sustain heavy impact loads and this in part might explain a number of observed sizeable holes in the side shell of ships.

7. Scale Effects of Surface Tension in Viscous Flow Simulations

Although surface tension force is usually negligible relative to the large scales of realistic ocean waves whose surface may be hundreds of meters long, its effect can be expected to be important in steep, very high curvature waves used in scaled down laboratory investigations of extreme wave effects on marine structures. This therefore raises the question: to what extent do model-scale waves accurately represent full-scale waves? In line with this, it is useful to have a rational estimate of the smallest scale, or more precisely the smallest absolute size, at which tests may be conducted to ensure that in the investigation of extreme wave impact load on marine structures for example, model waves are not unrealistically modified by the effect of surface tension.

7.1 Surface-tension effects in theory and experiments

It was shown in section 2.3 that the effect of surface tension in a wave is included in the Navier-stokes equation by adding an extra pressure acting normal to and against the surface:

$$\boldsymbol{\Delta P = \gamma\left(\frac{1}{r_1} + \frac{1}{r_2}\right)} \qquad \mathbf{7.1}$$

γ is surface tension coefficient and r_1, r_2 represents the radius of curvature of the surface in the vertical and horizontal planes. In 2-dimensions, there is only one plane so that the equation becomes:

$$\Delta P = \frac{\gamma}{r} \qquad 7.2$$

If a model wave is scaled by the length-scale L, surface tension will scale according to L^2. Also, if we substitute R=1/r (surface curvature) in the equation, we can plot ΔP as a function of length-scale and surface curvature. Note that increasing surface curvature in a wave represents approach to breaking/over-turning. Figure 7.1 is a contour plot of ΔP in unit of N/m^2.

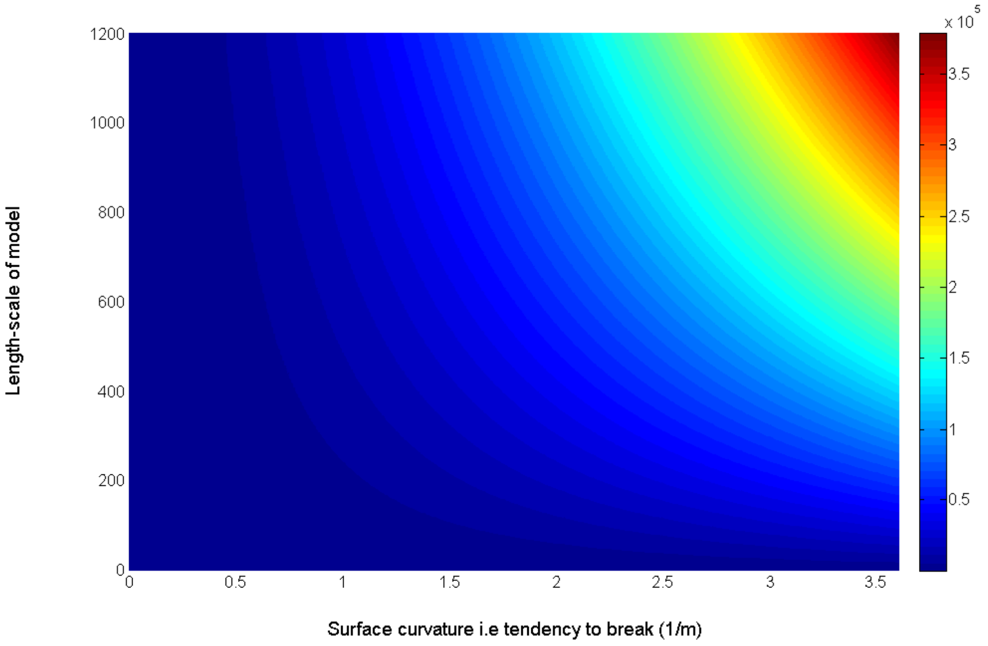

Figure 7.1: Contour plot of ΔP (notional effect of surface tension in scaled-down extreme waves)

In the figure 7.1 above, length scale represents the ratio of full to model scale i.e high value implies a small model. The figure above indicates that ΔP in a wave on the verge of breaking (high surface curvature) will be very small if the model is very large (low length-scale). Similarly, ΔP will be very small in a wave that is far from breaking even if the model is very small. ΔP only becomes considerable when the model is small and the wave is (near)breaking.

7.1.1 Surface tension in linear wave theory

Using the simple linear theory relationships of wave-length and dispersion:

$L = \frac{2\pi}{k}$ and $\omega = \sqrt{gk + \frac{\sigma}{\rho} k^3}$ where L = wave-length, k = wave-number, g = gravity acceleration, ω = frequency, ρ = water density and σ = capillary force given in N/m, the interesting influence of surface tension on a simple sinusoidal wave can be demonstrated.

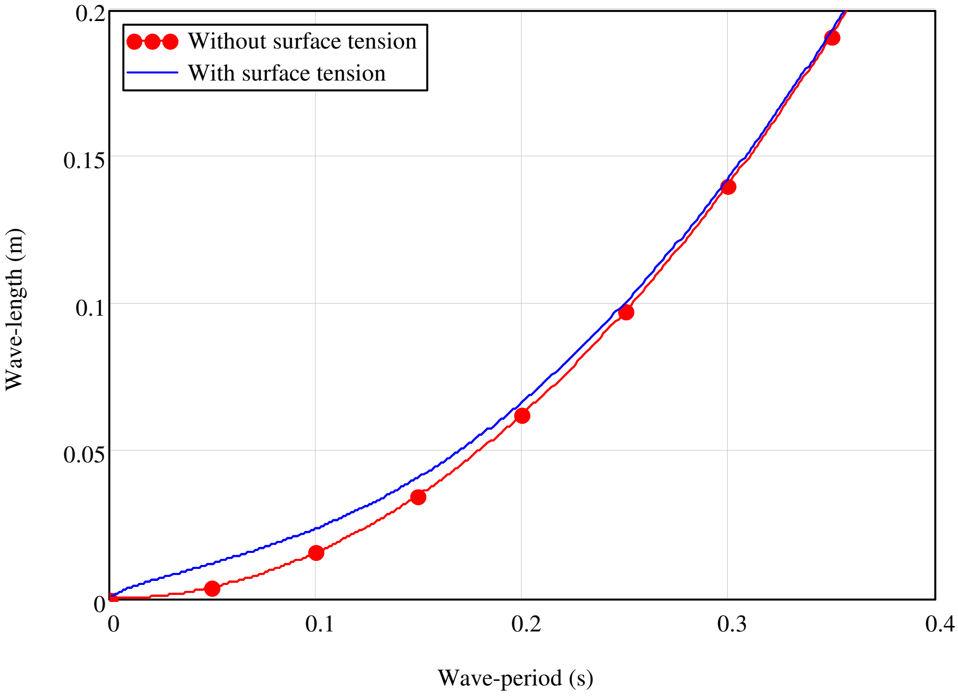

Figure 7.2: Effect of surface tension as predicted by linear theory

Figure 7.2 suggests that surface-tension effects set-in at wave-periods of 0.3s and less. It indicates that when the waves are very small surface-tension tends to elongate the wave thereby reducing its steepness. In the higher curvatures of non-linear wave crests, the effect of surface tension might be expected to reduce the curvature and hence the wave-slope and thus suppress breaking. Effects of surface tension are investigated in this chapter.

7.1.2 Previous work

A large number of investigations have been reported on the subject of surface tension effects in water waves. Therefore an exhaustive review of these is not intended; rather a few of the works dealing with breaking waves which are close to the present topic will be highlighted. One of such works is the numerical and physical lab measurements of Tulin et al (2001) which demonstrated the suppression of the spout of a breaking wave by surface tension. Interestingly, Debiane and Kharif (1996) have also shown how a wave that is weakly influenced by surface tension can turn out to be steeper than a pure gravity wave. This seems to bring into question the conventional assumption that the effect of surface tension is always to suppress wave steepness. Apart from the above, many other experiments (Cox, 1958; Chang et al, 1978; Yermakov et al, 1986; Ebuchi et al, 1987; Perlin et al, 1993; Zhang, 1995 etc) and numerical (Longuet-Higgins, 1995; Crapper, 1970; Ruvinsky et al, 1991; Mui and Dommermuth, 1995; Song and Sirviente, 2003; Iafrati and Campana, 2003 and 2005 etc) investigations have been carried out. However, these works have been mainly concerned with the effect of surface tension on the process of breaking and more specifically, the generation of capillary waves on gravity waves.

7.1.3 Present work

Using a wave-tank implemented in the commercial Navier-Stokes solver – Fluent, it is sought here to understand the effect of surface tension in the context of what minimum laboratory sea-state should be adopted in the investigation of deep-water breaking waves to ensure that the model wave is a reasonable representation of the full-scale wave. The wave-tank used is described in Chapter 3 where the kinematics of alternative extreme wave (most probable steepest wave of Xu and Barltrop, 2005) and its difference from the traditional extreme wave (most probable highest wave of Tromans et al, 1991), is also explored. In section 7.2 , model and full scale results are compared for a traditional extreme wave in a full-scale sea state with H_s=21.56m and T_z=13.4s where the H_s value is such that the wave is just on the verge of breaking at the point of the extreme event. In section 7.3, model and full scale results are also compared for the alternative extreme wave in a full-scale sea state with H_s=17.67m and T_z=13.4s where the wave is also on the verge of breaking.

From full scale where the effect of surface tension is negligible, the scale is gradually reduced (gradually increasing the effect of surface tension) in steps of 1:40 to a scale of 1:800 with the intent to see the laboratory scale H_s-T_z combination at which the shape and kinematics of the model extreme wave begins to significantly diverge from those of the full scale wave.

7.2 Traditional Extreme wave

In this section, results are presented for the most probable highest wave (full-scale sea-state: H_s=21.56m and T_z=13.4s) generated by focusing the individual crest at a so called "focus position" according to Tromans et al, 1991.

7.2.1 Influence of Surface tension on wave shape

Figure 7.3 shows the time history of full-scale and model scale water surface elevation measured at a position 115m (downstream of the wave-maker) where the wave is just breaking (surface is vertical).

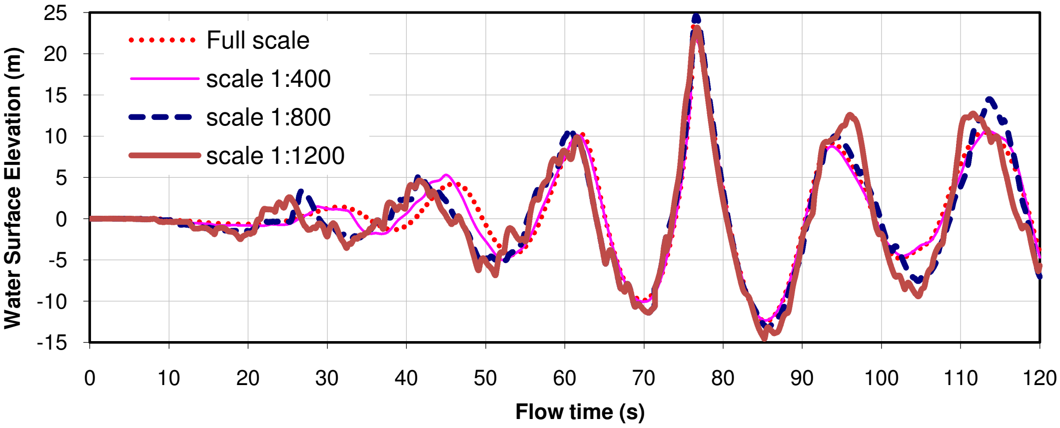

Figure 7.3: Time history of water surface elevation (traditional extreme wave: full-scale H_s=21.5579m, T_z=13.4s, JONSWAP peakedness parameter=2)

It can be seen that at the times far away from the extreme event, the smaller waves are considerably modified by the increasing effect of surface tension. This means that apart from the suppressing effect of surface tension on the spout developing at the extreme crest, there will also be a modification of the shape due to the fact that the shorter waves which focus to form the extreme crest have been modified by surface tension before focusing.

In the extreme crest which is the region of interest, the modification is not at first visible but a closer examination shows a clear modification of the wave's crest shape.

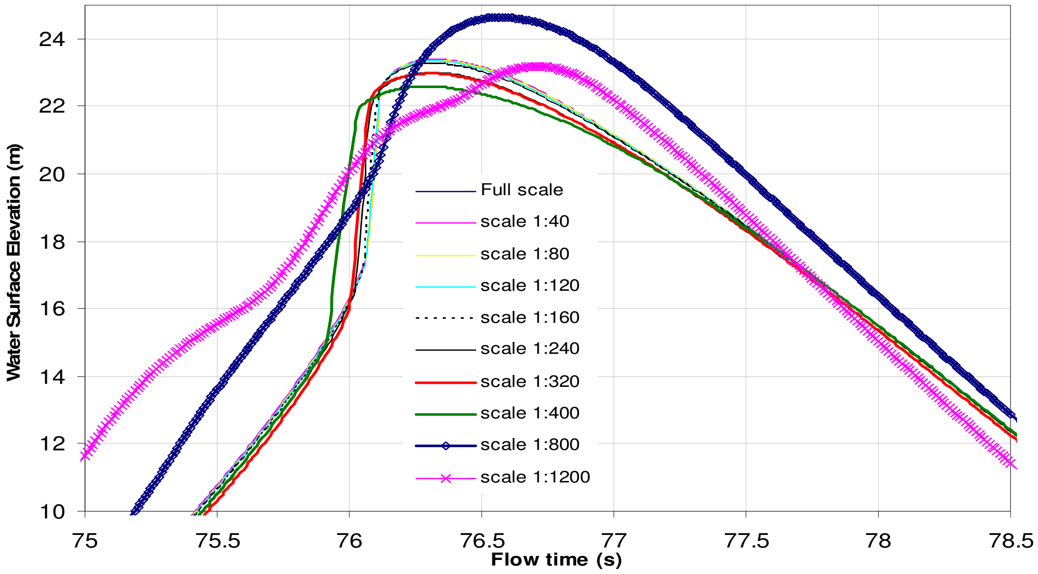

Figure 7.4: Closer view of the crest of scaled waves (traditional extreme wave: full-scale Hs=21.5579m, Tz=13.4s, JONSWAP peakedness parameter=2)

In figure 7.4, it can be seen that at scales 1:400 (H_s=53.89mm) and less, modelled waves are significantly different from the full scale wave with scale 1:800 (H_s=26.95mm) and less being so different that the wave is far from breaking. At scales 1:320 (H_s=67.37mm) and 1:240 (H_s=89.82mm) the difference is less but is still visible. However, H_s=179.65mm (scale 1:120) and larger give a crest that is very close to the full scale shape.

7.2.2 Influence of Surface tension on Particle velocity

In the preceding section, the comparison of model and full scale wave has been somewhat qualitative and a quantitative comparison is now attempted in this section. Figure 7.5 below shows the difference between model and full scale resultant particle velocity (magnitude) occurring in the crest of the simulated waves. The difference is shown as a percentage of the full-scale value with a positive value indicating increase and negative value indicating a reduction relative to full-scale. The first curve represents maximum velocity in the wave, measured at the point in time (76.2s) when the full-scale wave was just breaking (the scaled waves did not break at the same point as the full-scale wave). The other curve represents maximum velocity measured at the point in time and space where each wave is just breaking, irrespective of when or where this occurred in the tank. This was done by animating the whole sequence and stepping in time and space to find when and where breaking occurred.

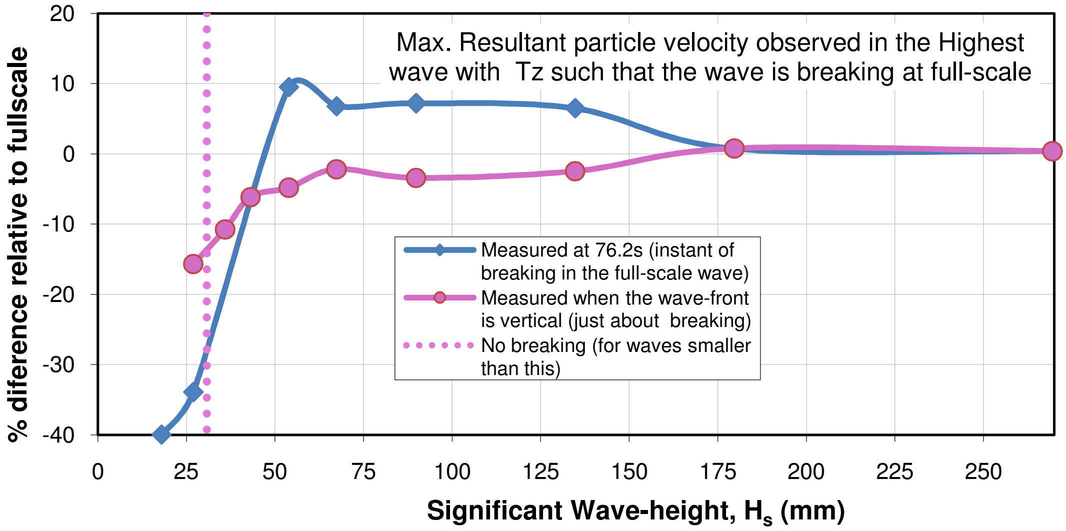

Figure 7.5: Deviation of particle velocity in the model-scale traditional extreme waves (full-scale: H_s=21.5579m, T_z=13.4s ,JONSWAP peakedness parameter=2)

The simulations suggest that below H_s=179.65mm (T_Z=1.22s), the model wave begins to significantly diverge (celerities and the spacio-temporal point of breaking changes) from the full-scale wave. Curiously, maximum particle velocities measured in the model waves ($43mm \leq H_S \leq 179.65$mm) at the instant of full-scale wave-breaking (76.2s) were found to be higher than those measured at the point when/where each model wave was breaking. This suggests that maximum kinematics for waves of this size, may occur well before breaking and therefore maximum induced load does not necessarily occur at the point of breaking. For model waves less than H_s=43mm, the observed particle velocities were higher at the point of breaking as one would expect. Also interesting is that there was no breaking in model waves below H_s=30.80mm.

7.3 Alternative Extreme wave

In chapter 3, it was shown that an alternative extreme wave exists which can be a breaker in a sufficiently high sea-state despite being about 25% less in height than the traditional extreme wave (most probable highest) which may not be breaking and is less severe in the same sea-state. Therefore, it is expected that the results obtained in section 7.2 above on the basis of the most probable highest wave cannot be generalized. Following from this, the alternative extreme wave in the sea-state with H_s=17.67m and T_z=13.4s is investigated in this section as done for the traditional extreme wave (H_s=21.57m and T_z=13.4s) in section 7.2 above.

7.3.1 Influence of Surface tension on wave shape

Figure 7.6 shows the time history of full-scale and model scale water surface elevation measured at a position 253m (downstream of the wave-maker) where the wave is just breaking (surface is vertical).

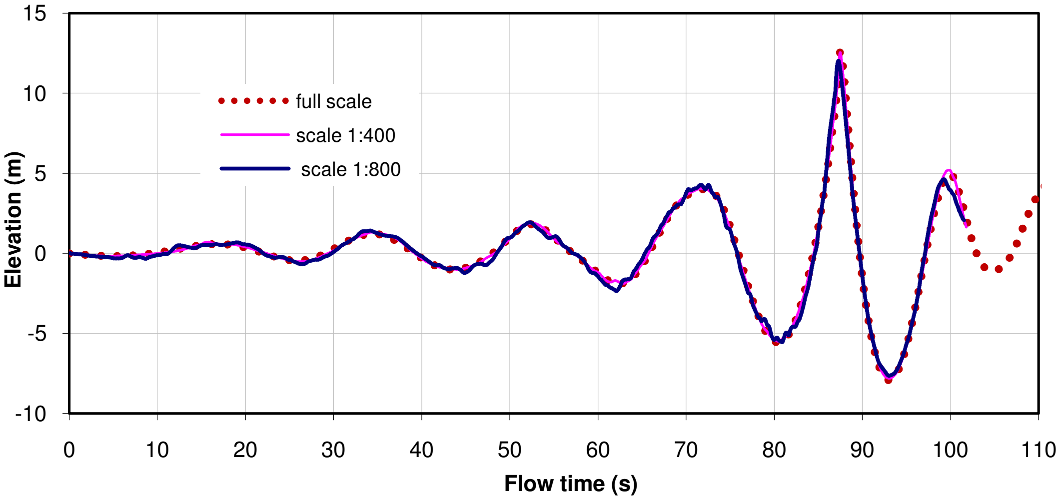

Figure 7.6: Time history of water surface elevation (alternative extreme wave: full-scale H_s=17.67m, T_z=13.4s , JONSWAP peakedness parameter=2)

Unlike the traditional extreme wave in section 7.2 where increasing surface tension seems to introduce some high frequency oscillations and higher phase speed in the region away from the extreme crest, this surface tension effect is virtually absent in the alternative extreme wave although slightly visible in the most extreme case of surface tension simulated - scale 1:800 (H_s=22.09mm, T_z= 0.474s).

Figure 7.7 is a close-up of the extreme crest which is the region of interest and shows an interesting difference in the shape of the wave crest introduced by increasing surface tension.

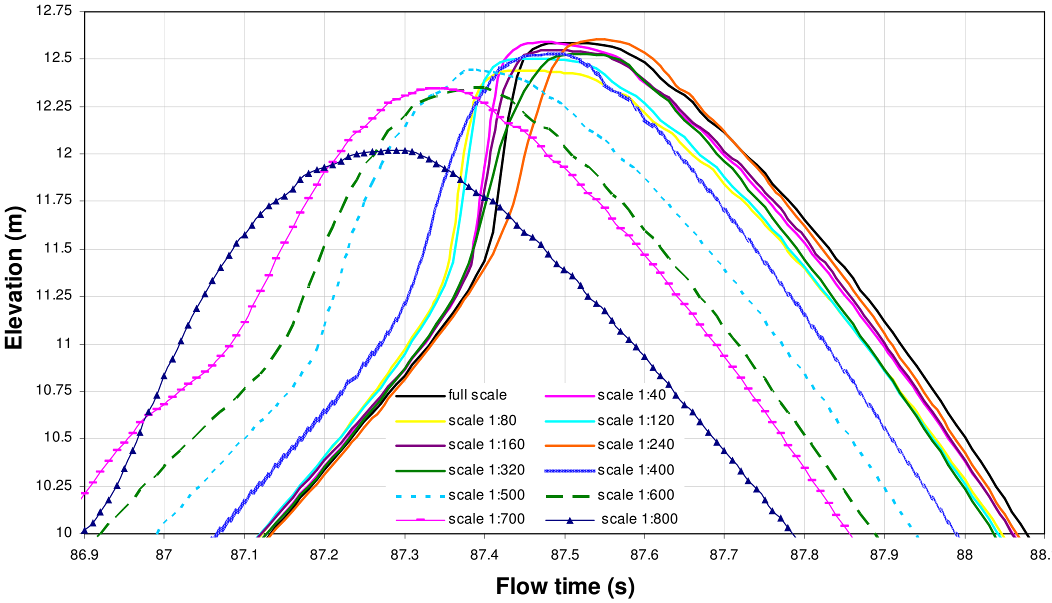

Figure 7.7: **Closer view of the crest of scaled waves (alternative extreme wave: full-scale Hs=17.67m, Tz=13.4s, JONSWAP peakedness parameter=2)**

Although the scale 1:40 wave (H_s=441.75mm, T_z= 2.12s) in figure 7.7 seems to arrive 0.01s earlier than the full-scale wave, it appears to be the closest to the shape of the full-scale crest. The departure from the shape of the full-scale crest is even more obvious at scales 1:400 (H_s=44.18mm, T_z= 0.67s) and less, with scale 1:800 (H_s=22.09mm, T_z= 0.474s) being so different that the wave is far from breaking. In fact, it was found that below H_s=55.22mm (T_z=0.75s), surface tension was so strong that the breaking wave-front was reduced to a series of large ripples and no breaking occurred throughout the simulation.

7.3.2 Influence of Surface tension on Particle velocity

Although the qualitative comparison of model and full scale waves in 7.3.1 above is useful, a quantitative comparison is more objective and easier to understand. Such a quantitative comparison is presented here as done in section 7.2 for the traditional extreme wave. Figure 7.8 shows the difference between model and full scale maximum dynamic pressure and resultant particle velocity (magnitude) occurring in the crest of the simulated waves. The difference is shown as a percentage of the full-scale value with a positive value indicating increase and negative value indicating a reduction relative to full-scale. As in section 7.2, the first curve represents maximum velocity in the wave, measured at the point in time (76.2s) when the full-scale wave was just breaking (the scaled waves did not break at the same point as the full-scale wave). The other curve represents maximum velocity measured at the point in time and space where each wave is just breaking, irrespective of when or where this occurred in the tank. This was done by animating the whole sequence and stepping in time and space to find when and where breaking occurred.

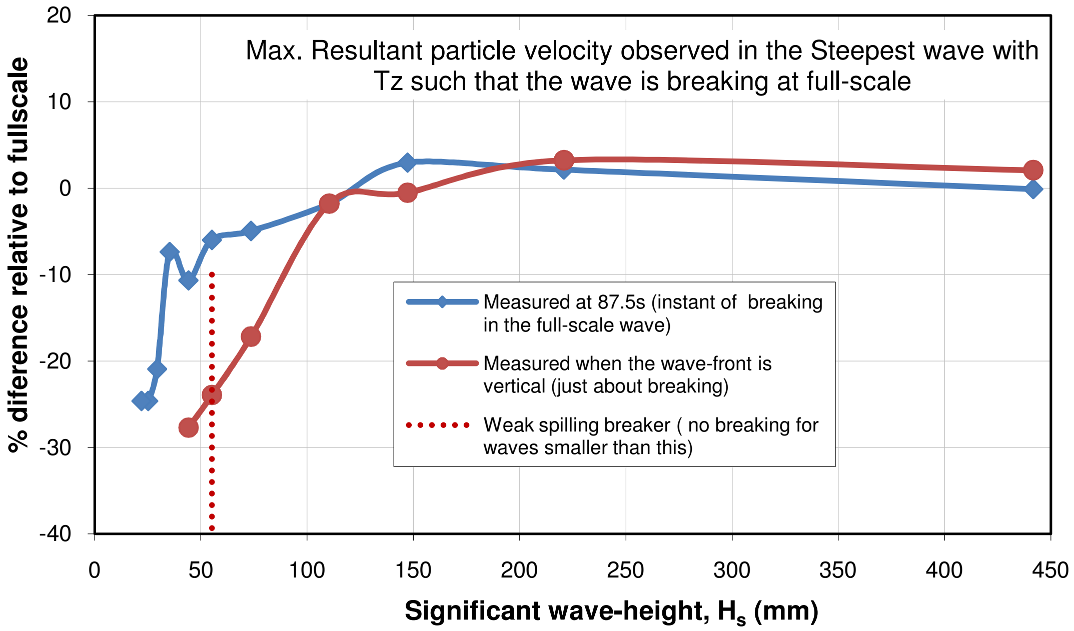

Figure 7.8: Deviation of particle velocity in the model-scale alternative extreme waves (full-scale: H_s=17.67m, T_z=13.4s, JONSWAP peakedness parameter=2).

Although the degree of divergence from full-scale values fluctuates slightly about full-scale right from H_s=441mm and less, by assuming a tolerance of ±3%, a critical sea-state: H_s=110.44mm (T_z=1.06s) is defined below which the model wave is no longer an acceptable representation of the full-scale wave. While particle velocities in the scaled waves above H_s=147.25mm (T_z=1.22s) are more than particle velocities in the full scale wave, the reverse is the case for scaled waves below H_s=147.25mm (T_z=1.22s). This is similar to the behaviour observed in the traditional extreme wave where scaling down initially exacerbates kinematics and by extension, breaking.

It can also be seen that below H_s=200mm, particle velocities measured at the point of breaking are less (contrary to expectations) than those measured at 76.2s where the wave was not breaking. In other words, maximum particle velocities occur well before breaking in the scaled alternative extreme waves less than H_s=200mm. Recall that this behaviour was also observed in the traditional extreme wave where it was found that in small scale waves, maximum particle velocities did not always occur at the point of breaking. Therefore at such small scales, it is very difficult in the laboratory to determine the maximum load exerted on a drag-dominated structure since there is no way of telling when or where the maximum kinematics occur. This problem is even more complicated for wave-impact/slap situations since exerted loads also depends on wave-slope (related to $\frac{\partial m}{\partial t}$ in equation *6.12*) rather than kinematics alone. Recall from equation 6.10 that wave-impact load is essentially given by $v\frac{\partial m}{\partial t}$. Therefore, to obtain the maximum impact load, the structure being tested has to be placed at the point where $\frac{\partial m}{\partial t}$ (slope) and $\mathbf{v}$ are maximum. Unfortunately, the two maxima are not co-incident so that maximum impact load will not necessarily occur at the point of maximum slope or maximum kinematics.

7.4 Discussion

The reversal of the effect of increasing surface tension observed in the alternative extreme wave in section 7.3 suggests that contrary to what is expected, reducing scale may not necessarily result in suppression of spout formation, at least in breaking waves generated by focusing wave fronts. Rather, breaking can initially (large length scales) be exacerbated by reducing scale from full-scale down to a certain threshold (somewhere around H_s=220mm for the alternative extreme wave studied here). In practice, this is of little relevance because the exacerbation only results in the wave breaking slightly earlier but does not affect the particle kinematics at breaking which is more relevant from a loading point of view.

Traditional Extreme **Alternative Extreme**

(a) H_s=21.56m, T_z=13.4s (at 76.2s) (d)H_s=17.67m, T_z=13.4s (at 87.5s)

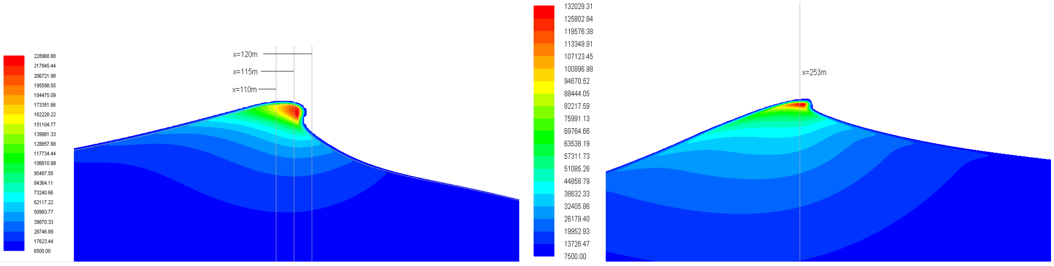

(b) H_s=0.0539m, T_z=0.67s (at 75.15s) (e) H_s=0.22088m, T_z=1.5s (at 87.5s)

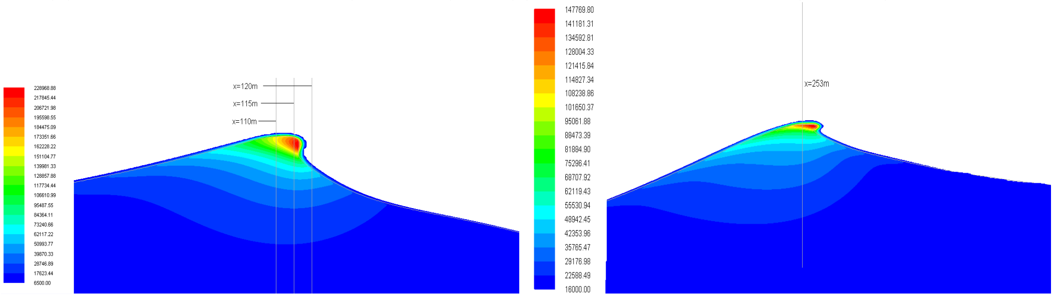

(c) H_s=0.02695m, T_z=0.47s (at 76.2s) (f) H_s=0.02209m, T_z= 0.47s (at 87.5s)

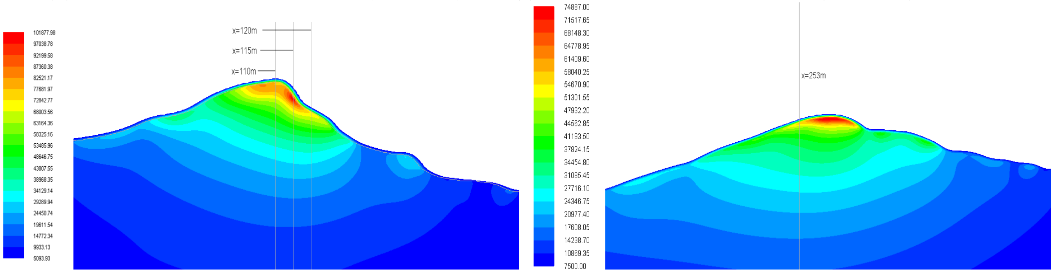

Figure 7.9: Contour of dynamic pressure at the time of full-scale breaking for the most probable highest (traditional extreme, Hs=21.56m, Tz=13.4s) and steepest waves (alternative extreme, **H_s=17.67m, T_z=13.4s,** JONSWAP peakedness parameter=2).

At scales larger than the identified threshold, it appears that surface tension is not high enough to suppress the breaking spout/jet but is just sufficient to keep the free-surface from breaking-up. This may mean that the pressure distribution in the wave crest is such that the crest top is able to sustain higher particle velocities without breaking so that the spout/jet is more pronounced. This is consistent with the observation of Debiane and Kharif (1996) that rather than suppressing steepness, surface tension (provided it is not too high i.e weak surface tension) will actually enhance the steepness of a wave and by extension exacerbate the spout/jet of a breaking wave subject to an intermediate amount of surface tension. At the smaller scales, surface tension gets larger than gravity and the pressure in the wave, such that the flow is dominated by surface tension and therefore breaking is suppressed. This is also in line with the observation of Grue (2002) that very high frequency effects present at moderate scales could not be reproduced when the scale became too small. Ironically, this effect was not observed in the breaking traditional extreme wave rather kinematics and vigour of the spout were monotonously suppressed as the wave became smaller.

To illustrate the suppressing effect of surface tension on breaking, snap-shots of the extreme wave crest is presented in Figure 7.11 in intervals of 0.36s. It can be seen that the crest gradually increases in steepness and reaches a maximum slope at about 78.17s-78.85s after which the slope reduces without the crest actually overturning. In other words, the wave reached a breaking point but the effect of surface tension suppressed any developing spout and prevented it from breaking.

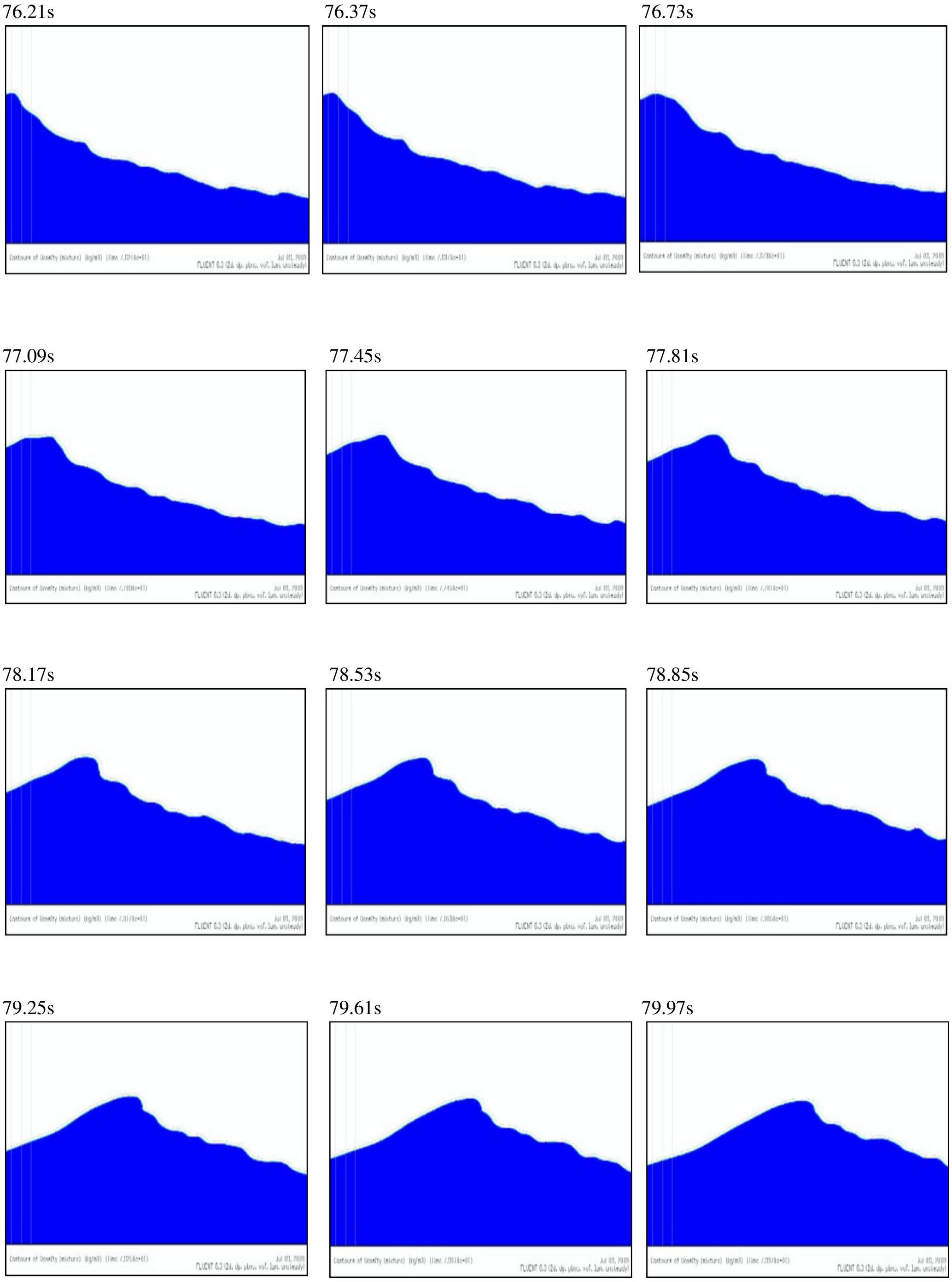

76.21s

76.37s

76.73s

77.09s

77.45s

77.81s

78.17s

78.53s

78.85s

79.25s

79.61s

79.97s

Figure 7.10: Suppression of the crest of an otherwise (full-scale) breaking wave by very severe surface tension (H_s=0.0269474m, T_z=0.4738s, JONSWAP peakedness parameter=2) . Notice how the crest grows to become vertical and then reduces in front steepness all without developing a spout.

7.4.1 Simple theoretical notion of surface-tension effect.

In section 7.1 (equation 7.2), it was shown that the effect of surface tension is represented in 2-dimensions as a pressure: $\Delta \mathrm{P} = \frac{\gamma \mathrm{L}^2}{r}$, where γ is the surface-tension coefficient, L is a length-based scaling-down factor and *r* is the radius of curvature of the surface. Using this representation of surface-tension, a simplistic but useful explanation of the observations in 7.4 above can be given in terms of the inter-play of forces/pressures in the wave crest. In such a simplistic theoretical notion of the scale effects of surface tension, three situations are of interest:

1) **When model waves are very large (L→1.0) and are far from breaking (r is very large but u is very small)**

In this situation, $\Delta \mathrm{P} = \frac{\gamma \mathrm{L}^2}{r}$ is very small since $\gamma \mathrm{L}^2$ is small and r is large. Also, $\frac{1}{2}\rho u^2$ will be very small since *u* is small.

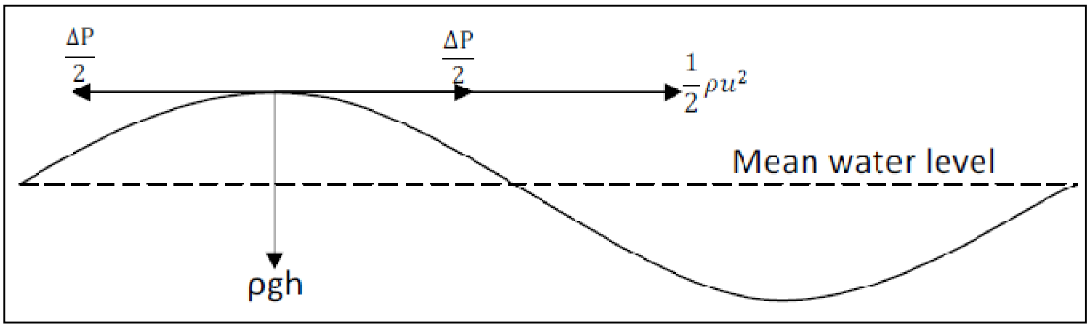

Figure 7.11: Idealization of forces in the crest of a non-breaking wave.

As a result, the dominating force will be ρgh. In other words, the wave is gravity dominated.

2) When model waves are very small (L is very large) and are breaking (r is very small but u is very large).

In this situation, $\Delta P = \frac{\gamma L^2}{r} \rightarrow \infty$ since γL^2 will be very large and r, very (infinitely) small.

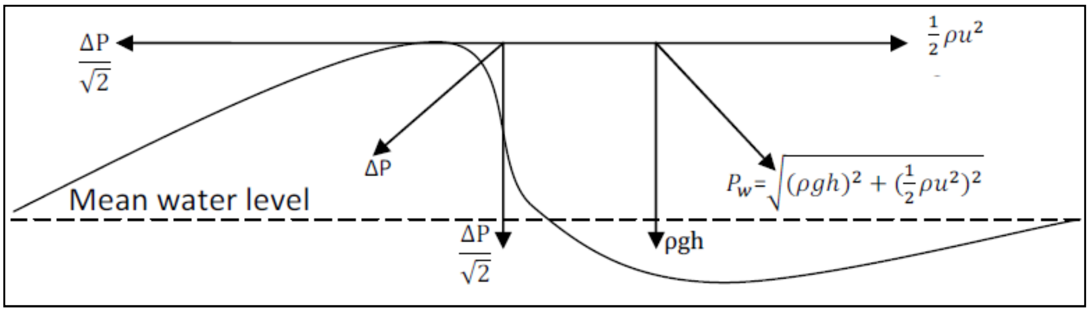

Figure 7.12: Idealization of forces in the crest of a breaking wave.

However, P_w is quite finite and $\Delta P \ggg P_w$. The implication is that the flow is dominated by surface-tension and the developing spout is suppressed.

3) When model waves are of intermediate length-scale (L is large but not too large) and are breaking (r is very small but u is very large).

While r may be small in this situation, γL^2 may not be large enough for $\Delta P = \frac{\gamma L^2}{r}$ to tend to infinity**.** Therefore when L is such that ΔP is close to P_w in a breaking wave, the surface curvature implies a “sharp corner” and a concentration of pressure in the wave on the corner. With slight increment of L (at very large values of L where $\Delta P \ggg P_w$, the spout is suppressed) and by extension ΔP , the degree of this concentration should also increase. This is because the system is in some kind of equilibrium ($\Delta P \approx P_w$) so that increase in ΔP would result in additional reaction pressure force from the water. This additional reaction force is only appreciable because $\Delta P \approx P_w$ but would be negligible when either of ΔP and P_w is dominant (i.e $\Delta P \gg P_w \; or \; \Delta P \ll P_w$). Thus at intermediate model scales, it is expected that this extra pressure will exacerbate crest particle velocity and the formation of a spout, rather than suppressing it.

7.4.2 Defining a minimum threshold

The results presented in sections 7.2 and 7.3 above indicate that for the specific cases investigated , the properties of the model wave begins to diverge significantly from those of the full-scale wave at about H_s=110.44mm (T_z=1.06s) and H_s=179.65mm (T_z=1.22s) for the most probable steepest and highest waves respectively . These may be considered the minimum acceptable model scale sea-states for representing the $\frac{1}{13}$ and $\frac{1}{16}$ significant steepness sea states that were investigated.

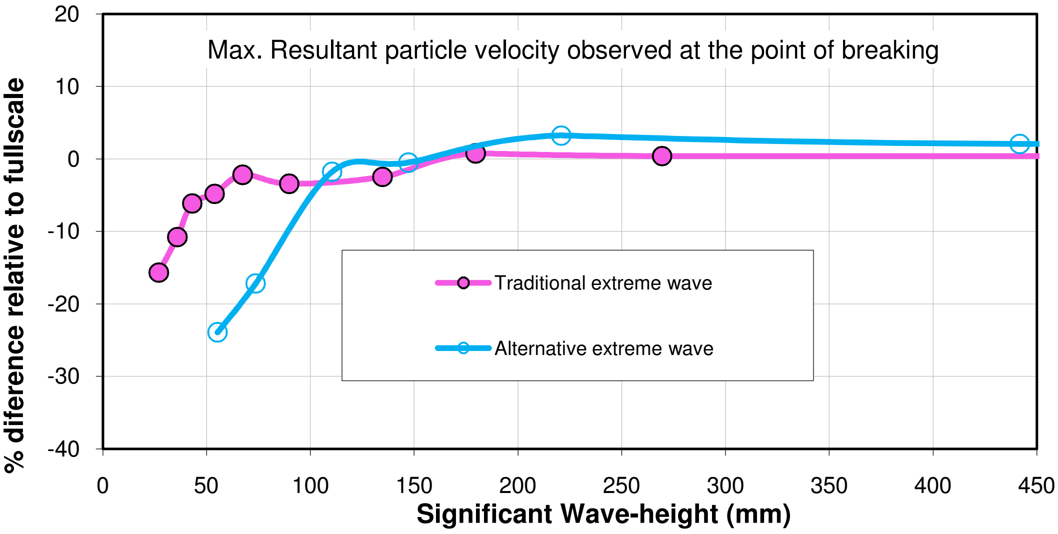

Figure 7.13: Comparison of the deviation (from full-scale values) of model traditional and alternative extreme wave particle velocity resultants (full-scale: H_s=17.67m, T_z=13.4s, JONSWAP peakedness parameter = 2). The curves suddenly stop at the lower Hs (≤ 50mm) since the waves do not break at such small scales.

In the present context, minimum acceptable model scale refers to the smallest scale a wave may be modelled without the effects of surface-tension becoming so considerable that the model scale wave is considerably different from the full-scale wave. It is important to emphasise that the values quoted above are for the extreme case of breaking in deep-water.

A more useful way of presenting this concept of a limiting absolute wave-height will be in terms of realistic laboratory sea-states. Thus, for a range of typical laboratory sea-states (characterized by H_s and T_z) a threshold of laboratory scale H_s and T_z combinations can be defined beyond which surface tension effects become considerable and as a result unacceptable.

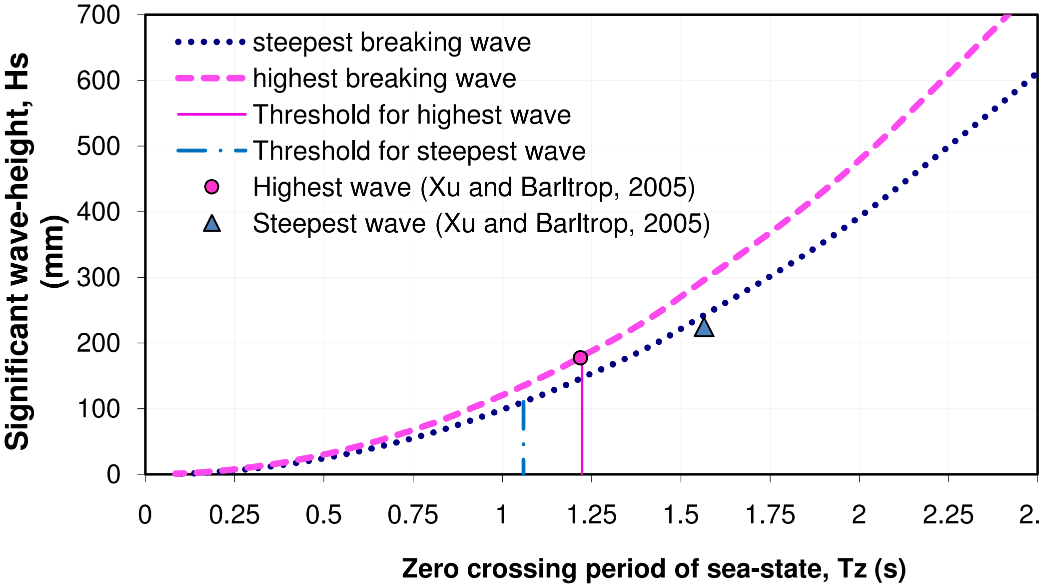

Figure 7.14: Proposed minimum model sea-state for breaking wave experiments

The two curves shown in figure 7.15 above represent various H_s–T_z combinations in which breaking occurs for the traditional new-wave (Tromans et al, 1991) and the alternative new-wave (Xu and Barltrop, 2005) respectively. Above these curves, breaking tends to occur before the wave is focused and therefore does not constitute an extreme case. One is more interested in the region on and below the curves. The two vertical lines represent the threshold of surface tension effect: to the right of the lines, surface tension has negligible impact but to the left of the lines surface tension effect is considerable and a most probable extreme (highest or steepest) wave tested in this region will most likely be a poor representation of the full-scale wave. Therefore in model tests of breaking wave impact on an FPSO for example, one needs to ensure that the sea-state used in the laboratory remains to the right of the vertical lines in figure 7.15 above.

7.5 Effect of turbulence in very small models

The preceding results have been obtained in the context of laminar flow since it was shown in 3.5.1 that turbulence is negligible. However, this was based on full-scale surface-tension effects and as shown in this chapter, surface tension considerably modifies the flow at very small length-scales. It is thus useful to check whether the effect of turbulence modelling is indeed negligible at the smaller laboratory scales where surface-tension effect is considerable. This is attempted by comparing 1:800 scale water-surface elevation time-history obtained with a turbulence model (realizable k-ε) and without a turbulence model (laminar) at the position (x=120m) where maximum surface elevation was recorded.

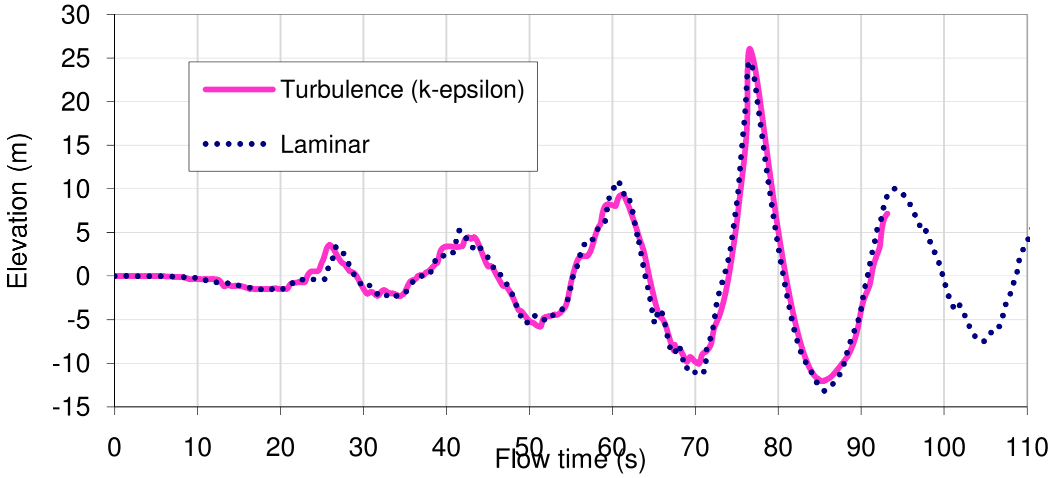

Figure 7.15: Comparison of Laminar Vs turbulent (k-ε) flow surface elevation time history at model scale 1:800 (scaled up to match full-scale Hs=21.56m, Tz=13.4s, JONSWAP peakedness parameter=2) for a wave that was at the verge of over-turning when modelled at full-scale.

Figure 7.17 shows the crest horizontal particle velocity measured at the instant when surface elevation was maximum at the position x=120m where the time history of figure 7.16 was recorded. While the surface elevation time-history seems quite similar, the observed particle velocities seem to suggest a considerable difference between laminar and turbulent (realizable k-epsilon) flow result.

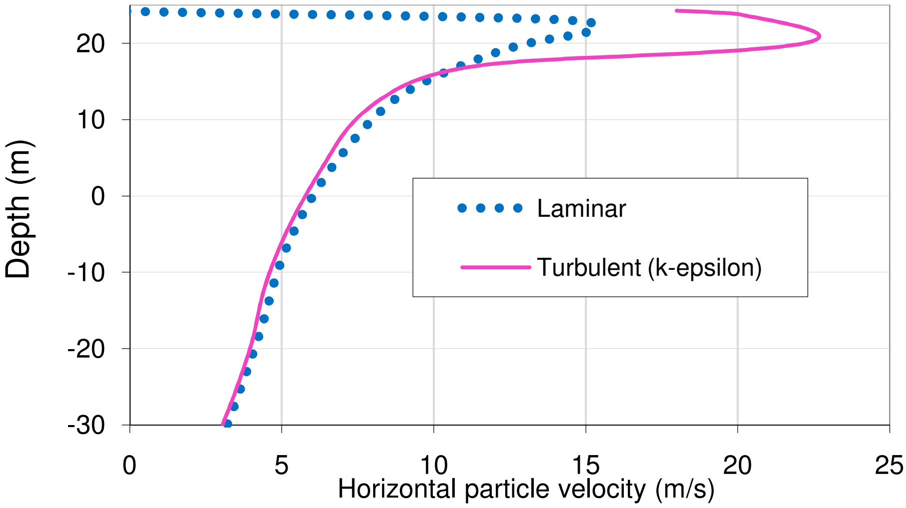

Figure 7.16: Comparison of Laminar Vs turbulent (k-ε) flow particle velocity at model scale 1:800 (scaled up to match full-scale H_s=21.56m, T_z=13.4s JONSWAP peakedness parameter=2) measured at x=120m and t=76.55s.

However, it was found that the introduction of turbulence modelling resulted in the wave breaking slightly earlier than in the laminar flow simulation.

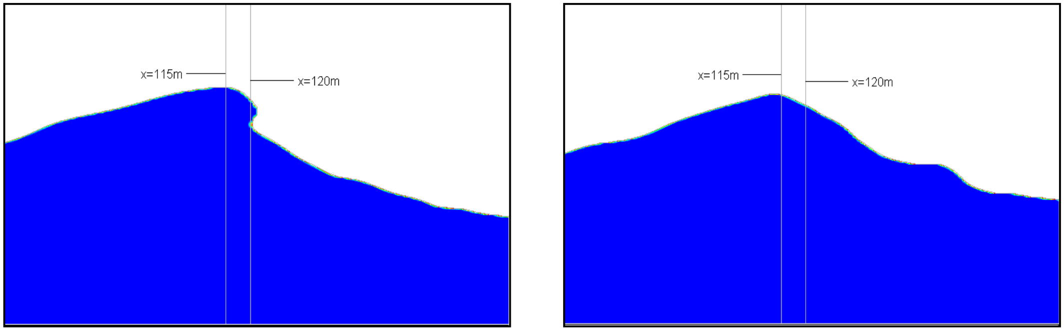
(a)Turbulent (realisable k-epsilon) (b) Laminar

Figure 7.17: Shape of crest at 76.55s

Therefore comparison of kinematics at a fixed position (x=120m as done in figure 7.17) measured at the shown instant (76.55s) is misleading since the wave obtained with a turbulent model is breaking but the laminar result is not breaking at the instant. From the view point of wave-loading, one is more interested in the kinematics at breaking rather than the position where breaking occurs. Figure 7.19 shows the two cases (turbulent and laminar) at their respective times of maximum front-steepness.

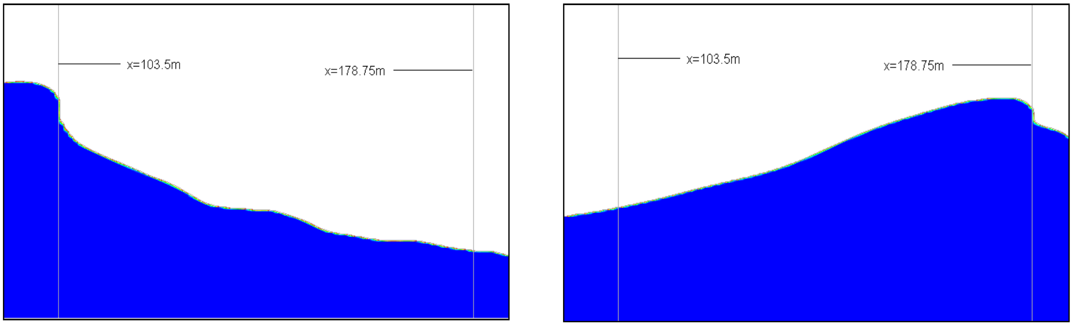
(a)Turbulent (realisable k-epsilon) (b) Laminar

Figure 7.18: Shape of crest at the time (75.74s for turbulent, 79.35s for laminar) and position (x=103.5m for turbulent, x=178.75m for laminar) where wave was just about breaking.

Therefore a more appropriate comparison of the laminar and turbulent flow simulations will be on the basis of kinematics measured at the point of breaking (which occurs at different spacio-temporal points) in the two simulations. In figure 7.20 below, horizontal particle velocities under the crest at the point in time and space where the water surface is virtually vertical and is just about breaking are presented for the laminar flow (vertical surface occurs at x=178.75m and t=79.35s) and turbulent flow (vertical surface occurs at x=103.5m and t=75.74s) simulations.

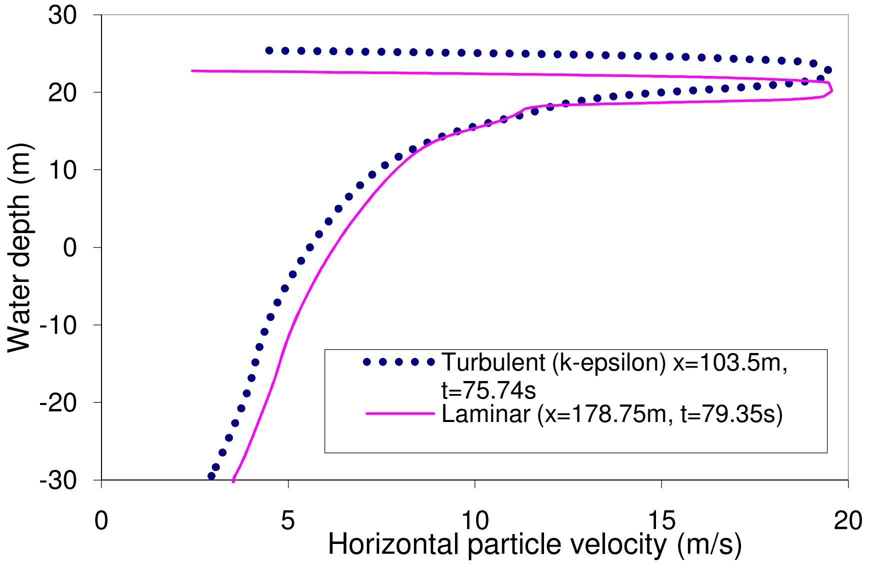

Figure 7.19: Particle velocity obtained from turbulent (k-ε) and laminar flow simulations at model scale 1:800 (scaled up to match full-scale H_s=21.56m, T_z=13.4s, JONSWAP peakedness parameter=2). Results have been recorded at the time and position where the water surface was just vertical in both simulations.

While turbulence modelling seems to change the position and vigour of breaking, the difference in terms of the particle velocities measured at the actual point in time and space where front steepness was maximum (water surface just vertical) is relatively small, as can be seen in figure 7.20. Therefore, on the basis of water surface elevation and horizontal particle velocity of such a small wave (H_s=27mm, T_z=0.47s), it seems reasonable to conclude that the effect of turbulence (at least in the sense of k-e modelling and extreme-wave kinematics) at small length-scales can be neglected and therefore, a laminar flow simulation is sufficient for the present purpose. Moreover, it is important to note that RANS turbulence modelling as done here does not have a theoretically robust basis. Indeed, the various RANS turbulence models are empirically tuned to diverse considerations and therefore produce varied results. Therefore, it is difficult to make definite inferences from them. It is better to look at such results in a qualitative sense and since the results are not very different, it is reasonable to use the threshold obtained from the laminar flow simulations which is more theoretically robust and perhaps more reliable .

7.6 Concluding Remarks

The effect of turbulence has not been very apparent in this work. With the benefit of hindsight, it would be desirable for future studies to use an LES rather than a RANS formulation of turbulence modelling with the hope of picking-up some of the flow details that are averaged-out in RANS. It is important to point out that due to the added “eddy viscosity” one would expect turbulent flow simulations to give lower particle velocity results. However, it was observed in section 3.5.1 that viscosity had very little (if any) effect on the kinematics of even a breaking wave. Furthermore, since the suggested threshold is based on relative rather than absolute magnitudes of full and model scale kinematics, it is reasonable to expect that turbulence (at least in the sense of k-epsilon modelling) will have a negligible impact on the suggested threshold. The implication of this suggested minimum threshold becomes evident when we consider that linear theory (figure 7.2) predicts surface-tension effects to become significant at wave-periods of 0.3s and less. Whereas, the present results shown in figure 7.15 indicates a higher threshold of T_z=1.06s (steepest wave) and T_z=1.22s (highest wave). This is not surprising since the linear theory threshold is in the context of non-breaking regular waves while the threshold suggested in section 7.4.2 is based on irregular breaking waves.

In the light of the present work, it seems that while the most probable steepest wave (H_s=224mm, T_z=1.57s) generated in a physical tank by Xu and Barltrop (2005) is much larger than the suggested threshold, their most probable highest wave (H_s=177.5mm, T_z=1.22s) is just on the threshold leaving no margin of safety in terms of surface tension effects (at least in the sense of the threshold suggested here). It therefore seems desirable to have used a slightly larger wave (slightly higher H_s and T_z) in generating the breaking highest wave of Xu and Barltrop (2005). However, it is important to note that the suggested threshold is indicative rather than absolute and waves within the vicinity of the threshold may well be suitable. Notwithstanding, it is more desirable to use waves that are larger than the threshold by a comfortable margin.

8. Conclusions.

There has long been a feeling amongst sailors that front steepness in waves indicates a higher vigour and thus bigger damaging power compared with high waves of moderate front steepness. However, the statistics of “most probable extreme value” (e.g Tromans et al, 1991) indicates that the steepest wave that is most likely to be encountered in a sea-state will be considerably lower than the highest wave that is most likely to occur in the same sea-state. This has raised the question of how the kinematics of the so called most probable highest wave (traditional extreme/ NewWave) and by extension induced loads, compare with those of the steepest wave (alternative extreme) that is most likely to occur in the same sea-state given that perturbation theory of waves seems to suggest that kinematics depend on wave-height. The present work has attempted to investigate the relative severity of these alternate extremes. Kinematics and loads due to the traditional (NewWave) and alternative extreme waves were investigated using a numerical wave-tank implemented in a commercial Navier-Stokes solver and validated with time-history of water-surface elevation from experiment and the so-called fifth order new-wave theory (Walker et al, 2005). An interesting difference between the kinematics and exerted loads of the two extremes was observed. It was further attempted to develop simple theoretical methods to predict the water particle kinematics of large waves which were observed in the Navier-Stokes simulations. First, a simplified model which is based on a simple modification to linear theory and second order accurate, was developed. Based on a similar idea and a simplified way of including higher order effects, the method was further extended to a non-linear form.

The usefulness of the developed methods was then tested by comparing their predictions of horizontal particle velocity in the extreme wave with published results and velocities observed in the Navier-Stokes simulation. Furthermore, the implications of the observed kinematics on the loading of a hypothetical fixed slender structure and a hypothetical floating ship-shaped structure are respectively demonstrated (albeit simplistically) and recommendations are given for floating and fixed structures in extreme seas. Using the same Navier-Stokes wave-tank used to investigate kinematics, the effect of surface tension on a breaking traditional wave (NewWave) as well as a breaking alternative extreme wave is also explored, culminating in the recommendation of a minimum laboratory-scale sea-state for investigating breaking wave effects on marine structures.

8.1 Contributions of the present work

This work has been a conglomeration of a series of small investigations on diverse aspects of extreme waves and extreme wave-loading on marine structures. At the core of these is an attempt to provide a new perspective to the problem of extreme wave-loading. This work has therefore contributed to the understanding of extreme-waves in the following ways:

1. **Better understanding of the kinematics of an alternative extreme wave**: Although the majority of extreme wave investigations have focused on the traditional NewWave, there have been a few published deep-water investigations on the importance of wave-shape. Using a viscous-flow model, the present work has added to the understanding of extreme waves by identifying the kinematics in the alternate extreme waves defined in terms of height and front-steepness respectively.

2. **Better understanding of the effect of the alternate extreme waves on various types of structures:** By applying the identified kinematics to rate of change of momentum, Morison equation and strip/linear diffraction theory, better understanding of the dramatic difference in the forces exerted by the alternate extreme waves has been realized. On the basis of the obtained forces, it is shown that the relative importance of the alternate extreme waves is dependent on the type of structure (floating or fixed, mono-cylinder or multi-leg etc) and loading type (vertical or horizontal, drag or inertial, impact or quasi-static) in question. This work can therefore serve as a guide for determining the appropriate wave (or combination of waves), critical to the performance of a given marine structure.

3. **Guidance on the effect of convective acceleration in extreme waves:** There has long been a debate about the significance of convective acceleration in wave-loading. For example, the conventional strip theory

implicitly assumes that convective acceleration is negligible. Similarly, API RP 2A-LRFD (C.3.2.10) recommends that convective acceleration be neglected. While this recommendation may be valid for most fixed structures in practice, the present work has shown that it is not necessarily applicable to a typical floating (partially submerged) structure. It has been shown that the neglect of convective acceleration can result in under-estimation of the wave-load on the bottom of a floating (partially submerged) structure in extreme waves .

4. **Guidance on alleviating surface tension effects:** In the investigation of breaking waves, the effect of surface-tension on small (model-scale) waves have been long recognized but there has been very little or definitive guidance on how small a focused extreme wave can be before surface-tension effects become significant. The readily available guidance is based on regular wave dispersion relation (figure 7.2) which suggests that surface-tension effect set-in at wave periods of 0.3s and less. This cannot be applied to irregular waves and it has been shown in Chapter 7 that in breaking waves (generated by focusing), the effect of surface tension is quite considerable even in waves that are much larger than the dispersion relation will seem to suggest. By comparing extreme particle velocities and surface elevation observed in viscous-flow simulation at various model scales with those observed in a full-scale wave simulated in the same way, separate laboratory sea-states (characterized by T_z and H_s) have been identified as

reasonable thresholds for the traditional and alternative extreme waves respectively, below which a laboratory wave will be a poor representation of the equivalent full-scale breaking wave.

5. **New simple method for resolving the problem of high frequency contamination:** Although several sophisticated non-linear wave models exist, simpler methods are desirable and several of such methods which essentially seek to remedy the problem of high frequency contamination inherent in the linear wave theory, are in existence. However, these methods are known to give unsatisfactory results especially in the crest of steep waves. In this work, the problem of frequency contamination is resolved by allowing the spectral components of a random wave-field to "ride-over one another" in a systematic and rational way.

6. **Adaptation of the 5th order New-wave theory to wave kinematics:** The 5th order new-wave theory of Walker et al (2005), which deals with water surface elevation has been modified and developed into a method for calculating more non-linear particle kinematics.

8.2 Kinematics of the Alternative extreme wave

Using the new-wave theory, it has been shown that an alternative extreme wave can be defined in terms of maximized slope to give the steepest wave that is most likely to occur in a sea-state by working in terms of wave slope rather than amplitudes (crest-heights) as done in the traditional extreme wave characterized by height. This alternative extreme has not been given much consideration in the context of a realistic broad-banded random wave spectrum.

In the investigation of the alternative extreme wave which was breaking, it was observed that the convective parts of particle acceleration were of similar magnitude compared to the local/temporal component and acted in opposing direction so that the neglect of the convective term could result in over-estimation of total acceleration by several times. The implication is that diffraction force which opposes Froude-Krylov force in partially submerged bodies, is larger when convective acceleration is ignored (but implicit in the Froude-Krylov force obtained directly by pressure integration) so that the calculated net vertical force is significantly less than the more realistic value obtained by considering the total acceleration which includes the convective acceleration. Therefore in line with the conclusion of Jensen et al (2006) with respect to a steep wave which is not breaking, results of the present study indicates that the full material time derivative: $\frac{Dv}{Dt} = \frac{\partial v}{\partial t} + \left(u\frac{\partial v}{\partial x} + v\frac{\partial v}{\partial y}\right)$ rather than the more convenient local time derivative $\frac{\partial v}{\partial t}$, should be used to define vertical water particle accelerations in simulating inertial wave-loads in extreme waves. This is in situations where the Froude-Krylov force has been obtained directly from pressure integration otherwise, treating acceleration consistently in the added mass as well as the Froude-Krylov force give vertical wave-loads that are independent of whether convective acceleration was considered or not. There has long been a debate about this effect of convective acceleration. For example, API RP 2A-LRFD (C.3.2.10) has recommended that convective acceleration be neglected. This was in the context of slender bodies subject to horizontal wave-loading. In practice, this can also be applied to majority of large volume fixed structures like caissons where the main load acting is in the horizontal direction and convection acceleration has been shown in chapter 3 to be negligible in this direction. In contrast, vertical convective acceleration is shown in Chapter 3 to be quite considerable. Therefore the API recommendation to ignore convective acceleration may be valid for fixed structures in practice but not necessarily applicable to a typical floating (partially submerged) structure like an FPSO. This is understandable as API RP 2A-LRFD is for fixed structures.

It was also observed that although the steepest wave is not as high as the traditional new-wave, it gave particle velocities and accelerations that were greater than those of the traditional new-wave (see e.g figures 3.13, 3.16 and 3.18). This is consistent with the measured impact forces reported in literature (e.g Xu et al, 2008(1); Xu and Barltrop, 2008(2) and 2005; Xu, 2005; Kjeldsen et al, 1979 and 1986 etc) which suggest that height alone is not sufficient to characterize an extreme wave rather front steepness also needs to be taken into account.

8.3 Wave-rider Kinematics

A method which is similar to stretching and extrapolation in its simplicity is developed based on a simplified form of wave-wave interaction which is robust to 2nd order. The method is based on the assumption that each wave component in a spectrum is riding on all other waves longer than itself. To check the usefulness of the new method, horizontal particle velocity results are compared with experimental measurements and theoretical computations of Skjelbriea et al (1991) and Stansberg et al (2006). Results of the new method show a good level of agreement with the results of Skjelbriea et al (1991) and 2nd order results of Stansberg et al (2006).

Although the linear form of wave-rider is in agreement with some experimental results in literature (e.g Skjelbriea et al, 1991; Stansberg et al, 2006 and Clauss et al, 2007), these results which were used to validate the method are at odds with some other results in literature (e.g Baldock et al, 1996; Farmer, 2002 and Grue, 2004). The former set of results indicate that extreme wave kinematics are appropriately modelled by second-order accuracy and therefore linear theory grossly over-predict velocities above mean water level whereas the later set of results show velocities that are larger than linear theory predictions and therefore more nonlinear than second-order results. It therefore became imperative to extend the linear form of the wave-rider method to a higher order.

Using the higher order approach of Walker et al (2005) which describes surface elevation, the basic form of the wave-rider method described earlier is extended to a higher order by including higher order terms. Results of the extended (non-linear) form of wave-rider are compared with those of Baldock et al (1996) and by extension, those of Grue et al (2004) who reported their results to be in very good agreement with those of Baldock et al (1996). These comparisons show a good agreement with the measurements and significant improvement over conventional stretching methods. Results of the new method have also been compared with simulations results obtained in this work and varying degrees of reasonable agreement was observed.

8.4 Scale effects of surface tension in viscous flow

Using the commercial Navier-Stokes solver- Fluent, two special cases of extreme waves are investigated with the aim of determining the length scale at which the effect of surface tension becomes sufficient to introduce significant departure from the equivalent full scale wave.

It has been found that an absolute size of wave in the laboratory exists where surface tension effects are negligible such that models of these waves are a good representation of full-scale extreme waves. Beyond (less than) this size of laboratory wave, the reduction of scale initially exacerbates the breaking process when the scale and by extension surface tension, has not reached a certain threshold. Once the scale is sufficiently low so that surface tension reaches the threshold, the flow is then dominated by surface tension and the formation of a breaking jet/spout begins to be suppressed. It was also found that in laboratory scale sea-states less than H_s=179.65mm, T_z=1.22s (traditional extreme wave) and H_s=200mm, T_z=1.43s (alternative extreme wave); higher particle velocities occurred well before breaking. This suggests that in laboratory waves of such sizes, maximum loading does not necessarily occur at the point when/where the wave is breaking. Therefore, loads obtained by placing a structure at the point in the tank where the model wave is observed to break may not be the correct extreme load. For higher kinematics to occur at the point of breaking, the size of the model wave needs to be increased (sea-state needs to be scaled up).

Based on the above observations, a threshold has been identified in a range of sea-states, for the two special cases of extreme waves (figure 7.14). This represents the point where the properties of the model wave begins to diverge significantly from those of the full-scale wave and gives an estimate of the minimum size a breaking wave may be tested in the laboratory without the effects of surface tension becoming so considerable that the model scale wave becomes a significantly poor representation of the full-scale wave.

8.5 Challenges

Since this work is focused on waves, the grids used for the simulations have had to be very fine in order to get a reasonable resolution of the water surface elevation. This has meant that a grid size of about 360,000 2-dimensional cells have been used. Therefore, one of the major challenges encountered in the course of this work has been the enormous computational time required for the viscous-flow CFD (computational fluid dynamics) simulations. This is even more so considering that hundreds of runs had to be done to acquire as much data as presented in Chapters 3 and 7 about alternative extreme wave's kinematics and scale effects of surface tension, respectively.

Extensive use of the University of Strathclyde's Engineering super-computing facility has been made, without which it may have been impossible to conduct as much simulations. However, the benefit of increased computational speed was not fully realised because of the extensive use of UDFs (user defined functions). As earlier explained, a UDF is a user written code that specifies inputs based on calculations that are not inherent in the CFD solver. Due to the architecture of the super-computing machine used (UDF is compiled for every node), the use of more nodes meant that more time was spent in accessing UDFs on all the various nodes which ultimately slowed down the simulations. This was so much that there was very little difference in simulation time using as much as 8 nodes and 2 nodes. In the end, majority of the simulations were done with only 2 nodes and the only benefit of the super-computing machine then, was that several simulations (each on 2 nodes) could be run simultaneously. However, this was also limited by the size of the machine and number of Fluent licences on the machine. In effect, only about 10 nodes were available for use at most times. This meant that only about 5 simulations at best, could be carried out simultaneously and each such run lasted about 10 days.

8.6 Future Work

Given the time frame and resources available for this work, only a very limited portion of the problem of full and model scale extreme wave kinematics and its impact on marine structures has been studied. More detailed investigation of the problem will be quite useful and it will be very interesting to see results of further studies in the following areas:

1. Repeat the work in chapter 7 (establish minimum threshold sea-state for minimizing surface-tension effects in the laboratory) using LES.
2. Investigate the effect of wind and more generally, the air-stream above the extreme crest of the traditional and alternative extreme waves.
3. Validate the wave-rider method in chapter 5 with more kinematics measurement and investigate ways of making the method more accurate.
4. Investigate why as indicated in section 2.7.2 (table 2.1), there seems to be two schools of published horizontal particle velocity measurements.
5. Investigate the effect of directional spreading on the relative severity of the kinematics of the traditional and alternative extreme waves.

REFERENCES

American Petroleum Institute. 1993. Recommended practice for planning, designing and constructing fixed offshore platforms – Load and resistance factor design (API RP 2A-LRFD). Reaffirmed 2003.

Baldock T.E., Swan C., Taylor P.H. 1996. A laboratory study of non-linear surface waves on water. *Phil. Trans. R. Soc. Lond.* **Ser. A 354,** p649-676.

Barltrop, N.D.P. 1998. *Floating structures: A guide for the design and analysis*. Oilfield Publications, Incorporated.

Barltrop, N.D.P. and Adams, A.J. 1991. *Dynamics of fixed marine structures, 3rd Edition*. Butterworth-Heinemann Ltd, Oxford.

Baarholm R. 2001. Theoretical and experimental studies of wave impact underneath decks of offshore platforms. PhD Thesis, Norwegian University of Science and Technology (NTNU), Trondheim, Norway.

Baarholm, R and O. Faltinsen. 2004. Wave impact underneath horizontal decks. J. Mar Sci Technol, 9, 1-13.

Baarholm, R, O.M. Faltinsen and K. Herfjord. 2001. Water impact on decks of floating platforms. Proc. 8th Int. Symp. on Practical Design of Ships and other Floating Structures (PRADS2001). Elsevier, Oxford.

Bea, R. G.; Xu, T.; Stear, J. and Ramos, R. 1999. Wave forces on decks of offshore platforms. Journal of waterway, port, coastal, and ocean engineering, 125 (**3**) p136-144.

Bergdahl, L. 2005. *Wave-induced loads and ship motions*. Dept. of shipping & marine technology lecture notes, Chalmers University of technology, Goteborg, Sweden.

Blackmore, P.A. and Hewson, P.J. 1984. Experiments on full-scale wave impact pressures. *Coastal Engineering,* **8** , 331-346.

Buchner, B. 2002. Greenwater on ship-type offshore structures. PhD thesis, Delft University of technology.

Cassidy, M.J. 1991. *Non-linear Analysis of jack-up structures subjected to random waves*. University of Oxford Doctor of Philosophy thesis.

Causon, D., Qian, L. , Hu, Z. and Mingham, C. 2008. CFD Modeling of Wave Loads on Offshore Wave Energy Devices. *Proceedings of the 18th International Offshore And Polar Engineering Conference, Vancouver, Canada. Vol.* **3***,* p137-142

Causon D.; David Ingram, D.; Mingham, C; Zang, J; Hu, K and Zhou, J.G. 2000. Numerically Simulating Seawall Overtopping. Proc. 27th Intern. Conf. on Coastal Engineering, Sydney, Australia.

Chan, E. S. and Melville, W. K. 1988. Deep-Water Plunging Wave Pressures on a Vertical Plane Wall. Proc. R. Soc. Lond., A417, p95-131.

Chang, J.H., Wagner, R.N. and Yuen, H.C. 1978. Measurement of high frequency capillary waves on steep gravity waves. *J. Fluid Mech.,* **86**, p401-413

Choi, H. 2005. *Kinematics Measurements Of Regular, Irregular, And Rogue Waves By PIV/LDV*. PhD Dissertation, Texas A&M University, 2005.

Choi, H., Cox, D.T., Kim, M.H. and Ryu, S. 2001. Laboratory Investigation of Non-Linear Irregular Wave Kinematics. *Proc. Of the 4th International Symposium,* Waves 2001, San-Franscisco, **2**, p 1685-1694.

Clauss, G., Schmittner, C., and Stuck, R., 2005. Numerical Wave Tank-simulation of Extreme waves for the Investigation of Structural Responses. *Proc. Of the*

24th International Conference on Offshore Mechanics and Arctic Engineering, Halkidiki, Greece.

Clauss, G., Schmittner, C., and Klein,M. 2006. Generation of waves with predefined steepness. *Proc. Of the 25h International Conference on Offshore Mechanics and Arctic Engineering, Hamburg, Germany.*

Clauss, G., Schmittner, C., Stempinski, F., and Stuck, R. 2006. Computational and Experimental Simulation Of Non-breaking and breaking waves for the Investigation of Structural Loads and Motions. *Proc. Of the 25h International Conference on Offshore Mechanics and Arctic Engineering, Hamburg, Germany.*

Clauss, G.; Stempinski, F. and Klein, M. 2007. Experimental and Numerical Analysis of Steep Wave Groups. *Proc. Of 12th International Congress Of The International Maritime Association Of The Mediterreanean; Varna, Bulgaria.*

Cox, C.S. 1958. Measurements of slopes of high frequency wind waves. *J. Mar Res*, **16**, p 199-225

Crapper, G.D. 1970. Non-linear capillary waves generated by steep gravity waves. *Journal of Fluid Mechanics,* **40**, p149-159

Cuomo, G.; Tirindelli, M. and Allsop, W. 2007. Wave-in-deck loads on exposed jetties. Coastal Engineering, **54** , p 657–679.

Debiane, M. And Kharif, C. 1996. A new limiting form for steady periodic gravity waves with surface tension on deep water. *Phys. Fluid,* **8**, p 2780-82

Drake, K.R. 1997. Wave profiles associated with extreme loading in random waves. *Proceedings of the International conference on Design and Operation for abnormal condition, Glasgow, Scotland.*

Drake, K.R.2000. Transient design for green-water loading on bulk carriers. *Journal of marine science and technology,* **5**, 21-30.

Drake, K.R.2001. Wave profile characterization of green water loading events from model test data. *Applied ocean research*, **23**, 187-193.

Farmer, D. 2002. Wave Kinematics at high sea-states. *Journal of Atmospheric and Oceanic technology*, **19** (2), p 225-239.

Fenton, J.D. 1985. A fifth-order Stokes theory for steady waves. *Journal of Waterway, Port, Coastal and Ocean Engineering,* **111**, 216–234.

Ferziger, J.H. and Peric, M. 2002. Computational methods for fluid dynamics (p294-302). Springer-Verlag Berlin Heidelberg, Germany.

Fluent Inc. 2006. *Fluent 6.3 User's guide*. September, 2006.

Fonseca, N. and Guedes-Soares, C. 2005. Experimental investigation of the shipping of water on the bow of a containership. Journal of offshore mechanics and arctic engineering, 127(**4**), 322-330

Forristall, G.Z. 1986. Kinematics in the crest of storm waves. *Proc. ICCE*, pp. 208-222

Gibson, R.S. and Swan, C. 2006 . The evolution of large ocean waves: the role of local and rapid spectral changes. *Proc. R. Soc. Lond.* **A 463,** 21-48.

Greco, M. 2001. *A two-dimensional study of green-water loading.* Ph.D. thesis, Department of Marine Hydrodynamics, Faculty of Marine Technology, Norwegian University of Science and Technology, Trondheim, Norway.

Griffin, O.M. ,Skop, R.A., Keramidas, G.A , Swean, T.F., Wang, H.T. and Leipold, Y . 1988. Ocean and ship wake modification by a surface wake flow pattern. *Proc. 17th Symp. on Naval Hydrodynamics, The Hague, Netherlands,* pp17-36

Grue, J. 2002. On four highly non-linear phenomenon in wave theory and marine hydrodynamics. *Appl. Ocean Res.* **24**, p261-274

Grue, J., Clamond, D., Huseby, M. and Jensen, A. 2003. Kinematics of Extreme Waves In Deep Water. *Applied Ocean Research*, **25**, Issue 6, Pages 355-366.

Grue, J. and Jensen, A. 2006. Experimental velocities and accelerations in very steep wave events in deep water. *European Journal of Mechanics. B/Fluids,* **25**, pages 554-564.

Gudmestad, O.T. 1993. Measured and Predicted deep-water wave kinematics in Regular and Irregular Seas. *Mar. Struct.*, **6**, p1-73.

Hewitt, G.F. and Reeks, M.W. 2005. Prediction of turbulent flows (p238-241). Cambridge university press, New-york.

Iafrati, A. and Campana, E.F. 2005. Flow field fluctuation behind microbreakers: space-time behaviour and subsurface flow field. *J. Fluid Mech.*, **529**, p 311-347, 2005.

Iafrati, A. and Campana, E.F. 2003. A Domain Decomposition Approach to Compute Breaking Waves. *Int. Journal for Numerical Methods in Fluids,* **41**, p. 419-445.

Jensen, A., Clamond, D., Huseby, M. and Grue, J. 2006. On the local and convective accelerations in steep wave events. *Ocean Eng,* **34**, 426-435.

Kaplan P. 1992. Wave impact on offshore structures: re-examination and new interpretations. Proc. 24th Offshore Technology Conference, Houston, USA.

Kim, C.H. 2008. *Nonlinear Waves and offshore structures*. Advanced series in ocean engineering, World scientific publishing company .

Kırkgöz, M.S., 1991. Impact pressure of breaking waves on vertical and sloping walls. *Ocean Engineering* **18**, pp. 45–59.

Kjeldsen, S.P. 2000. Velocities in giant waves. *International Journal of Offshore and Polar Engineering*, **10** (3), p170-172.

Kjeldsen, S.P. and Myrhaug, D. 1979. Breaking waves in deep water and resulting wave forces. *Proceedings of the 11th Offshore Engineering Conference, Houston, Texas. Vol. 4,* p2515-2522.

Kjeldsen, S.P. , Torum, A. and Dean, R.G. 1986. Wave forces on vertical piles caused by 2 and 3 dimensional breaking waves. *Proc. 20th Int. Conf. Coastal Eng.* Taipei, *ASCE, New York,* p1929–1942.

Kleefsman, T. 2005. *Water Impact Loading On Offshore Structures: A Numerical Study*. PhD Thesis, Rijks Universiteit Groningen, 2005.

Kristiansen, T., Baarholm, R., Rortveit, G.J., Hansen, E.W and Stansberg, C.T. 2005. Kinematics In a Diffracted Wave Field: Particle Image Velocimetry (PIV) And Numerical Models. *Proc. of the 24rd International Conference on Offshore Mechanics and Arctic Engineering, Halkidiki, Greece.*

Longridge, J.K., Randall R.E. and Zhang J. 1996. Comparison of experimental irregular water wave elevation and kinematic data with new hybrid wave model predictions. *Ocean Eng,* **23,** pp. 277–307.

Longuet-Higgins, M.S. 1995. Parasitic capillary waves: a direct calculation. *J. Fluid Mech.,* **301**, p79-107

Longuet-Higgins MS. 1986. Eulerian and Lagrangian aspects of surface waves. *J Fluid Mech*; **173**:683–707.

Longuet-Higgins, M.S. 1962. M.S. Longuet-Higgins, Resonant interactions between two trains of gravity waves. *J. Fluid Mech.* **12**, p321–332

Longuet-Higgins, M.S. and Cokelet, E.D. 1978. The deformation of steep surface waves on water. II-Growth of normal mode instabilities. *Proc. Roy. Soc. Lond.* **A364**, 1-28.

Longuet-Higgins, M.S. and Phillips, O.M. 1962 Phase velocity effects in tertiary wave interactions. *Journal of Fluid Mechanics* **12**, p 333-336.

Longuet-Higgins M.S. and Steward R.W .1960. Changes in the form of short gravity waves on long waves and tidal currents. *J. Fluid Mech.,* **8,** pp. 565–583.

Mui, R.C.Y and Dommermuth, D.G. 1995. The vertical structure of parasitic capillary waves. *J. Fluids Eng,* **117**, p355-361

Nielsen, K.B. and Mayer, S. 2004. Numerical prediction of green water incidents, *Ocean Eng,* **31**, 363-399.

Ochi, M.K. and Tsai, C.-H. 1983 Prediction of Occurence of Breaking Waves in Deep Water. *J. Phys. Oceanogr.* **13**, 2008-2019

Peregrine, D.H.; Bredmose, H.; Bullock, G.; Obhrai, C.; Müller, G. and Wolters, G. 2004. Water wave impact on walls and the role of air, Proc. 29th Int. Conf. Coastal Engineerin, **Vol. 4**, World Scientific, Singapore, pp. 4005–4017.

Peregrine, D.H. 1995. Water-wave impact on walls and the associated hydrodynamic pressure filed. In *Wave-forces on inclined and vertical wall structures*, Committee on Waves and wave-forces of the Waterway, Port,Coastal and Ocean division of the American society of civil engineers, pp259-281.

measurements. *J. of Fluid Mech.,* **255**, p597-620.

Pham, X.P. 2007. Green water loading on high speed containerships. PhD thesis, Universities of Glasgow and Strathclyde, Glasgow, UK.

Philips, O.M and Banner, M.L. 1974. Wave breaking in the presence of wind drift and swell. *J. of Fluid Mech.*, **66 (4)**, p625-640.

Rainey, R. C. T. 2007. Weak or strong non-linearity: the vital issue. *J. Eng. Math.,* **58**, 229–249.

Perlin, M. , Lin, H. and Ting, C. 1993. On parasitic capillary waves generated by steep gravity waves: an experimental investigation with spatial and temporal

Rodenbusch G., Forristall G.Z. (1986). An empirical model for random directional wave kinematics near the free surface. *Proc. 18th Offshore Technology Conference,* Houston, OTC 5097, p137-146.

Ruvinsky, K.D., Feldstein, F.I. and Freidman, G.I. 1991. Numerical simulation of the quasi-stationary stage of ripple excitation by steep gravity-capillary waves. *Journal of Fluid Mechanics,* **230**, p339-353

Smith, C.B. 2006. *Extreme waves.* Joseph Henry Press, Washington D.C.

Smith, C.B. 2007. Extreme waves and ship design. *Proc. 10th Intn'l symp. On Practical design of ships & other floating structures.* Houston, Texas, U.S.A.

Sobey R.J. 1990. Wave theory predictions of crest kinematics, in: O.T. Torum, Gudmestad (Eds.), *Water Wave Kinematics, NATO ASI Series E: Applied Sciences*, vol. 178, Kluwer Academic Publishers, Dordrecht.

Song, C. and Sirviente, A.I. 2003. A numerical study of breaking waves. *Phy. Fluids,* **16**, p2649-2667.

Sparlat, P. R. and Allmaras, S. R. 1992. A one equation turbulence model for aerodynamic flows, *AIAA Paper, AIAA 92-0439.*

Srokosz, M.A. 1985. On the Probability of Wave Breaking in Deep Water. *J. Phys. Oceanogr.* **16**, 382-385

Stansberg, C.T., Gudmestad, O.T. & Haver, S.K. (2006). Kinematics Under Extreme Waves. *Proc. 25th International Conference on Offshore Mechanics and Arctic Engineering,* Hamburg, Germany.

Stansberg, C.T.; Baarholm, R. and Kristiansen, T. 2005. Extreme wave amplification and impact loads on offshore structures. Proc. 37th Offshore Technology Conference, 2-5 May 2005, Houston, Texas.

Stockwell, R.G.; Masinha, L. and Lowe, R.P. 1986. Localization of the complex spectrum: The S transform. *IEEE transactions on signal processing.* **44**, 998-1001.

Sulisz, W.; Wilde, P. and Wisniewski, M. 2005. Wave impact on elastically supported horizontal deck. Journal of Fluids and Structures 21 (2005) 305–319

Sutherland D., Greated C.A. & Easson W. J. 1991. Crest Kinematics In Wave Groups. *Proc. 1st Intl Conf Offshore Polar Engng,* Vol. 3, p97-103.

Swan,C., Bashir, T. And Gudmestad, O.T. 2001. Nonlinear Inertial Loading. Part1: Accelerations in Steep 2-D Water Waves. *Journal of Fluids and Structures,* ***16*** *(3)*, p391-416.

Taylor, P.H. (1992) On the kinematics of large ocean waves, *Proc. BOSS Conf.*, Vol.1, p134-145.

Tromans, P.S., Anaturk, A.R., Hagemeijer, P. 1991. A new model for the kinematics of large ocean waves: applications as a design wave. *In: Proceedings of the First International Offshore and Polar Engineering Conference, Edinburgh, Scotland*, *Vol. 3,* p64–71.

Tulin, M.P. and Landrini, M. 2001. Breaking waves in the ocean and around ships, *Proceedings of the 23rd symposium on naval hydrodynamics,* p713-745

Varyani, K.S. ; Pham, X.P and Crossland, P. 2004. Greenwater investigation onboard container ships and mobile units. Ship technology research (Schiffstechnick), 51(**4**), 151-161

Voogt, A. And Buchner, B. 2004.

Walker D.A.G., Taylor P.H. & Eatock Taylor R. 2005. The shape of large surface waves on the open sea and the Draupner New Year wave. *Applied Ocean Research,* **26** , p73–83

Westphalen, J., Greaves, D., Williams, C. 2007. Comparison of free surface wave simulations using STAR CCM+ and CFX. *Proceedings of the 10th numerical towing tank symposium, Hamburg, Germany. Vol. 23,* p47-88

Westphalen, J., Greaves, D., Williams, C., Zang, J. and Taylor, P. 2008. Numerical simulation of extreme free surface waves. *Proceedings of the 18th International Offshore And Polar Engineering Conference, Vancouver, Canada. Vol. 3,* p55-61

Wheeler, J.D. 1970. Method for calculating forces produced by irregular waves. *Journal of Petroleum Technology*, **22** (3), p359-367.

Wienke, J. and Oumeraci, H. 2005. Breaking wave impact force on a vertical and inclined slender pile - theoretical and large-scale model investigations. Coastal Engineering, **52**, 435-462.

Wilcox, D.C. 1998. Turbulence modelling for CFD. DCW Industries, Inc., La Canada, California.

Xia, J.Z.; Wang , Z.H. and Jensen, J.J. 1998. Non-linear wave loads and ship responses by a time-domain strip theory, *Marine Structures,* **11** (3) p101–123..

Xu, L. 2006. *Breaking wave slap loading on FPSO bows and shallow water cylinder.* PhD Thesis, Universities of Glasgow and Strathclyde, *Glasgow, Scotland.*

Xu, L. and Barltop, N.D.P 2005. *Wave slap loading on FPSO bows.* HSE Books.

Xu, L. and Barltop, N.D.P 2008. Bow impact loading on FPSOs 2- theoretical investigation. *Ocean Eng.,* **35**, p1158-1165.

Xu, L.; Zhang, M. and Wang, Y. 2007. Mathematical simulation of steep waves at a focus point. *J. Mar. Science & Application*, **6** (3), p6-11

Yan,S. and Ma, Q.W. 2008. Nonlinear simulation of 3d freak waves using a fast numerical method. *Proceedings of the 18th International Offshore and Polar Engineering Conference, Vancouver, Canada. Vol. 3,* p511-517

Yermakov, S.A., Ruvinsky, K.D., Salashin, S.G. and Freidman, G.I. 1986. Experimental investigation of the generation of capillary-gravity waves ripples by strongly non-linear waves on the surface of a deep fluid. *Izv. Atmos. Ocean. Phy.* **22**, p835-842 .

Zhang, J., Chen, L., Ye, M. and Randall, R.E. 1996. Hybrid wave model for unidirectional irregular waves, Part I. Theory and numerical Scheme” *Applied Ocean Research* **18**, p77–92.

Zhang, X. 1995. Capillary-gravity and capillary waves generated in a wind-wave tank: observations and theories. *J. Fluid Mech.,* **289**, p51-82.

Zhaowei, L., Renchuan, Z. and Guoping, M. 2005. Numerical Simulations For Green Water Occurence. *Journal of Hydrodynamics.* **B18(3),**498-504.

APPENDICES

APPENDIX A1: Theory of Fluid Flow (Navier-stokes equation)

A1.1 Continuity Equation

Consider an infinitesimal volume element *dxdydz of a* fluid , the mass inflow into the element in the x-direction for example, may be given by $d\boldsymbol{m} = \rho u dydz$ and the outflow by $d\boldsymbol{m} = [\rho\, u + \delta(\rho\, u\, dx)/\delta x]dydz$.

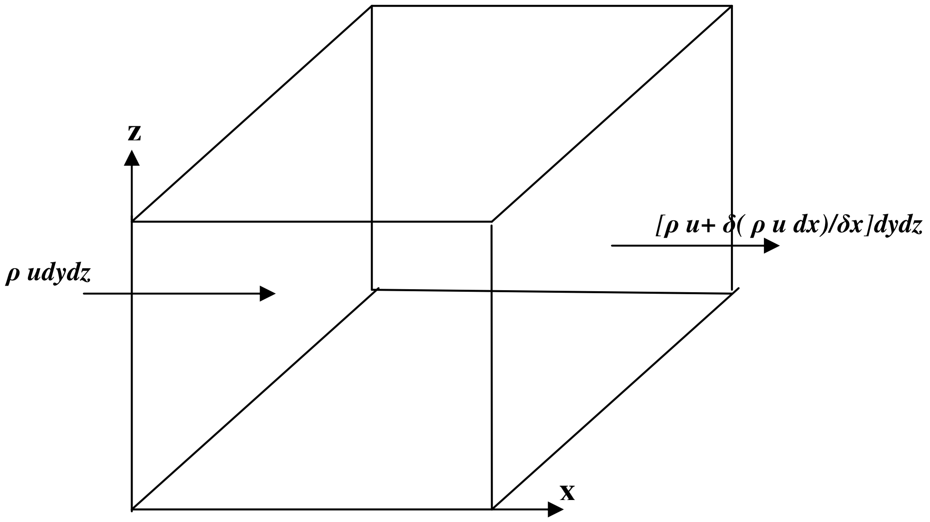

Fig A1.1 *infinitesimal fluid element*

The net outflow in the x direction is therefore $\delta(\rho u dxdydz)/\delta x$. Similarly, the net outflows are $\delta(\rho v dxdydz)/\delta y$ and $\delta(\rho w\ dxdydz)/\delta z$ in the y and z directions respectively. If we assume that the fluid is incompressible and mass is conserved (the amount of fluid flowing into the element is the same as that flowing out) , the sum of the outflows in all direction (x, y and z) must be zero :

$\delta u/\delta x+ \delta v /\delta y+ \delta w /\delta z = 0$. A-1

A1.2 Navier-Stokes (Momentum) Equations

In incompressible flows, the assumption of dynamic equilibrium (newton's second law) to an infinitesimal fluid element $dxdydz$, can be used to obtain a very good approximation of water flows:

$d\mathbf{F}=dm.\mathbf{a}$

where $d\mathbf{F}$ is the total force on an element of mass dm with acceleration $\mathbf{a}$

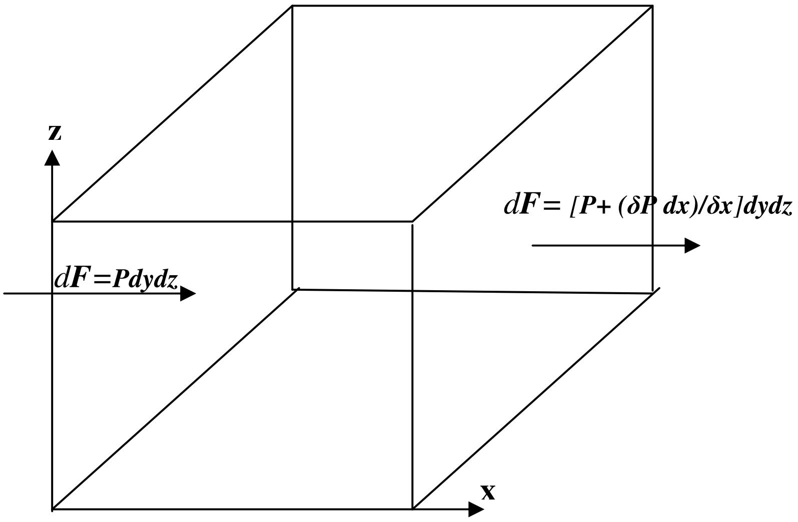

Fig A1.2 *Infinitesimal fluid element*

This total force consists of pressure forces $d\mathbf{F}_p$, body forces $d\mathbf{F}_b$ and viscous forces $d\mathbf{F}_v$ i.e

$$d\mathbf{F}_p + d\mathbf{F}_b + d\mathbf{F}_v = dm.\mathbf{a} \quad \text{......}A\text{-}2$$

Therefore:

$$\mathbf{a} = (d\mathbf{F}_p + d\mathbf{F}_b + d\mathbf{F}_v)/dm \quad \text{......}A\text{-}3$$

If *u, v* and *w* represent the x, y and z components of velocity respectively, applying the chain rule yields the substantive derivative from a velocity potential *Φ* (Larsson and Raven, 2004). The velocity potential is an arbitrary scalar function defined such that its gradient (the rate of change of *Φ* relative to the x , y and z coordinates) at any point in the fluid is the velocity vector, such that the associated components of acceleration may be written as:

$$\mathbf{a}_x = du/dt = \delta u/\delta t + u\, \delta u/\delta x + v\, \delta u/\delta y + w\, \delta u/\delta z \quad \text{......}A\text{-}4$$

$$\mathbf{a}_y = dv/dt = \delta v/\delta t + u\, \delta v/\delta x + v\, \delta v/\delta y + w\, \delta v/\delta z \quad \text{......}A\text{-}5$$

$$\mathbf{a}_z = dw/dt = \delta w/\delta t + u\, \delta w/\delta x + v\, \delta w/\delta y + w\, \delta w/\delta z \quad \text{......}A\text{-}6$$

When we split the forces $d\mathbf{F}$ on each fluid element into their x, y and z components, we can write that:

$\mathbf{a}_x = du/dt = \delta u/\delta t + u\,\delta u/\delta x + v\,\delta u/\delta y + w\,\delta u/\delta z = (d\mathbf{F}_{px} + d\mathbf{F}_{bx} + d\mathbf{F}_{vx})/\,dm$ A-7

$\mathbf{a}_y = dv/dt = \delta v/\delta t + u\,\delta v/\delta x + v\,\delta v/\delta y + w\,\delta v/\delta z = (d\mathbf{F}_{py} + d\mathbf{F}_{by} + d\mathbf{F}_{vy})/\,dm$........A-8

$\mathbf{a}_z = dw/dt = \delta w/\delta t + u\,\delta w/\delta x + v\,\delta w/\delta y + w\,\delta w/\delta z = (d\mathbf{F}_{pz} + d\mathbf{F}_{bz} + d\mathbf{F}_{vz})/\,dm$.....A-9

A1.2.1 Pressure Forces

The pressure force is due to difference in pressure between 2 opposite faces of the element. Considering the x-component of the pressure gradient , the pressure force can be written as

$d\mathbf{F}_{px} = -dxdydz\ \delta P/\delta x$ A-10

and since $d\mathbf{m} = \rho\ dxdydz$

$d\mathbf{F}_{px} / d\mathbf{m} = -1/\rho\ .\ \delta P/\delta x.$ A-11

Similarly,

$d\mathbf{F}_{px} / d\mathbf{m} = -1/\rho\ .\ \delta P/\delta y$ A-12

$d\mathbf{F}_{pz} / d\mathbf{m} = -1/\rho\ .\ \delta P/\delta z$ A-13

A1.2.2 Body Forces

Body forces are proportional to the mass of the element and may be reasonably assumed to act at its centre of gravity. Since we are here concerned with gravity waves, we assume that gravity is the only body force acting so that the x and y components of the body force become zero since gravity only acts along the vertical axis which is the negative z direction in the present coordinate system. Thus

$d\mathbf{F}_{bx} / d\mathbf{m} = 0,$ ……………………………………………………………………A-14

$d\mathbf{F}_{bx} / d\mathbf{m} = 0$ ……………………………………………………………………A-15

$d\mathbf{F}_{bz} / d\mathbf{m} = -g$ ……………………………………………………………………A-16

A1.2.3 Viscous Forces

Viscous forces derive from the viscosity of the fluid and are due to a combination of normal and tangential stresses acting on the sides of the fluid element (Larsson and Raven, 2004).The stresses in the x-direction may be represented as shown below:

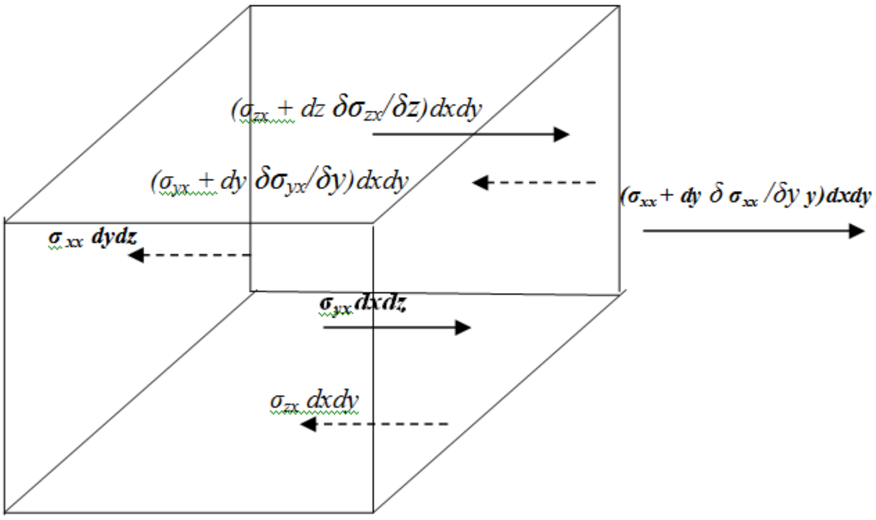

Fig A1.3 *infinitesimal fluid element*

The total viscous force in the direction (x in this case) may be obtained by summing up the individual stresses on each side of the fluid element so that the x-component of the viscous force may be written as $d\boldsymbol{F}_{vx}=(\ \delta\sigma_{xx}/\delta x+\ \delta\sigma_{yx}/\delta y+\ \delta\sigma_{zx}/\delta z)\,dxdydz$.
Since $d\boldsymbol{m}=\rho\ dxdydz$, we can write that:

$$d\boldsymbol{F}_{vx}/d\boldsymbol{m}=(\ \delta\sigma_{xx}/\delta x+\ \delta\sigma_{yx}/\delta y+\ \delta\sigma_{zx}/\delta z)\ /\rho. \quad \ldots\ldots\ldots\ldots\ldots\ldots\ldots\ldots A\text{-}17$$

Similarly in the y and z directions respectively, we can write that:

$$d\boldsymbol{F}_{vx}/d\boldsymbol{m}=(\ \delta\sigma_{xy}/\delta x+\ \delta\sigma_{yy}/\delta y+\ \delta\sigma_{zy}/\delta z)\ /\rho \quad \ldots\ldots\ldots\ldots\ldots\ldots\ldots\ldots A\text{-}18$$

$$d\boldsymbol{F}_{vz}/d\boldsymbol{m}=(\ \delta\sigma_{xz}/\delta x+\ \delta\sigma_{yz}/\delta y+\ \delta\sigma_{zz}/\delta z)\ /\rho \quad \ldots\ldots\ldots\ldots\ldots\ldots\ldots\ldots A\text{-}19$$

Larsson and Raven (2004) report that based on Newton's work in 1687 which linearly relates shear stress to the normal velocity gradient in the flow around a rotating cylinder, stokes proposed a generalized 3-dimensional model in 1845 where for incompressible flows, viscous stress tensor σ_{ij} is proportional to a rate-of-strain tensor S_{ij} i.e $\sigma_{ij}=\mu\ S_{ij}$ where μ is the fluid's absolute (dynamic) viscosity and $S_{ij} = \delta u_i/\delta x_j+\ \delta u_j/\delta x_i$.

Here, i and j are counters which may attain any one of the values of x, y or z. Acheson (1995), Panton (1984) and Schlichting (1987) present an extensive exploration of the theoretical foundation of this hypothesis. Since S_{ij} is symmetric, Larsson and Raven (2004) suggest that the stress tensors may be written as:

$\sigma_{xx}=2\,\mu\,\delta u/\delta x$

$\sigma_{xy}=\sigma_{yx}=\mu\,(\delta u/\delta y+\delta v/\delta x)$

$\sigma_{xz}=\sigma_{zx}=\mu\,(\delta w/\delta x+\delta u/\delta z)$

$\sigma_{yy}=2\,\mu\,\delta v/\delta y$

$\sigma_{yz}=\sigma_{zy}=\mu\,(\delta v/\delta z+\delta w/\delta y)$

$\sigma_{zz}=2\,\mu\,\delta w/\delta z$

Introducing these stresses into the Viscous Force relationship above (equations A-10 to A-12) results in

$$d\mathbf{F}_{vx}/d\mathbf{m} = (\delta\sigma_{xx}/\delta x+\delta\sigma_{yx}/\delta y+\delta\sigma_{zx}/\delta z)/\rho$$
$$= \mu/\rho(\delta^2u/\delta x^2+\delta^2u/\delta y^2+\delta^2u/\delta z^2+\delta^2v/\delta x\delta y+\delta^2w/\delta x\delta z) \ldots\ldots\ldots\ldots\ldots\ldots\text{A-20}$$

Because of continuity *(equation A-1)* and taking $\mu/\rho=\upsilon$ (kinematic viscosity) we can write that:

$dF_{vx}/dm = \upsilon\, (\delta^2 u/\delta x^2 + \delta^2 u/\delta y^2 + \delta^2 u/\delta z^2)$ A-21

and similarly in the y and z directions respectively,

$dF_{vy}/dm = \upsilon\, (\delta^2 \mathrm{v}/\delta x^2 + \delta^2 \mathrm{v}/\delta y^2 + \delta^2 \mathrm{v}/\delta z^2)$ A-22

$dF_{vz}/dm = \upsilon\, (\delta^2 w/\delta x^2 + \delta^2 w/\delta y^2 + \delta^2 w/\delta z^2)$ A-23

Recall from equation A-7 that:

$a_x = du/dt = \delta u/\delta t + u\, \delta u/\delta x + v\, \delta u/\delta y + w\, \delta u/\delta z = (dF_{px} + dF_{bx} + dF_{vx})/\, dm$

Therefore, introducing the above viscous forces (*equations A-21 to A-23*), the pressure forces (*equations A-11 to A-13*) and the body forces (*equations A-14 to A-16*) into *equations A-7 to A-9*, we obtain the so called Navier stokes equation in the x, y and z directions respectively, for the flow of an incompressible fluid where the only body force is gravity acting in the negative z direction and is sometimes called the momentum equation:

$$\frac{\partial u}{\partial t} + u\frac{\partial u}{\partial x} + \mathrm{v}\frac{\partial u}{\partial y} + w\frac{\partial u}{\partial z} = -\frac{1}{\rho}\frac{\partial P}{\partial x} + 0 + \upsilon\left(\frac{\partial^2 u}{\partial x^2} + \frac{\partial^2 u}{\partial y^2} + \frac{\partial^2 u}{\partial z^2}\right) \qquad \text{A-24}$$

$$\frac{\partial \mathrm{v}}{\partial t} + u\frac{\partial \mathrm{v}}{\partial x} + \mathrm{v}\frac{\partial \mathrm{v}}{\partial y} + w\frac{\partial \mathrm{v}}{\partial z} = -\frac{1}{\rho}\frac{\partial P}{\partial y} + 0 + \upsilon\left(\frac{\partial^2 \mathrm{v}}{\partial x^2} + \frac{\partial^2 \mathrm{v}}{\partial y^2} + \frac{\partial^2 \mathrm{v}}{\partial z^2}\right) \qquad \text{A-25}$$

$$\frac{\partial \mathrm{w}}{\partial t} + u\frac{\partial \mathrm{w}}{\partial x} + \mathrm{v}\frac{\partial \mathrm{w}}{\partial y} + w\frac{\partial \mathrm{w}}{\partial z} = -\frac{1}{\rho}\frac{\partial P}{\partial z} - g + \upsilon\left(\frac{\partial^2 \mathrm{w}}{\partial x^2} + \frac{\partial^2 \mathrm{w}}{\partial y^2} + \frac{\partial^2 \mathrm{w}}{\partial z^2}\right) \qquad \text{A-26}$$

APPENDIX A2: Theory of Surface Tension

Simplistically put, surface tension is a small but constant tensile force acting at the free-surface and tends to prevent distortion of the surface. Since it is small and constant, it is usually negligible relative to the large scales of realistic ocean waves whose surface may be several kilometres long and are therefore normally not accounted for in traditional wave theories. However, at smaller scales such as in scaled laboratory waves they may not be fully negligible and can become very important especially in situations where there is considerable deformation of the water surface such as in very steep near breaking or breaking waves.

In order to better explain the origin of this force, it is important to consider that at considerable depth within a liquid, molecules experience equal repulsive forces from surrounding molecules which cancel out. However, molecules at the surface of a liquid inter-facing a vacuum do not experience a balancing molecular repulsion since there are no molecules to provide this force. Instead molecules at the surface begin to attract themselves in order to maintain equilibrium (stability of the liquid surface). This attraction is in form of a tensile force acting tangentially to the surface and depends on the amount of force required to maintain equilibrium which itself is determined by the property of the other fluid in contact with the liquid.

Larsson and Raven (2004) illustrates this attraction as a tensile force which tends to open up a cut made in the free-surface of a liquid and the magnitude of this force is the length of the cut multiplied by a constant force γ known as the surface-tension coefficient.

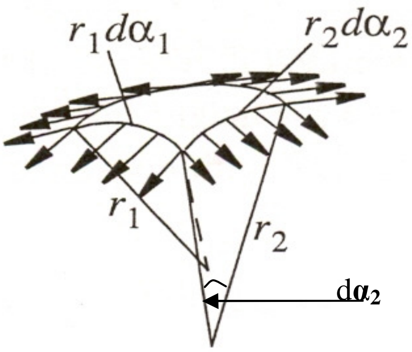

Figure A2.1: Surface tension in an infinitesimal element of the free-surface

In figure A2.1, an infinitesimal element of the liquid-surface enclosing liquid molecules below is shown and is defined by four of the type of cuts mentioned above. Due to the difference in the density of the two inter-facing fluids, there exists a pressure gradient ΔP at the inter-face resulting in a net force normal to the inter-face. In the case of a water-air boundary, this force is outward on the spherical surface of the water and is obtained by multiplying the surface area of the element $r_1 \, d\alpha_1 * r_2 \, d\alpha_2$ with the pressure difference ΔP i.e

$$F_{above} = r_1 \, d\alpha_1 \, r_2 \, d\alpha_2 \, \Delta P \quad \ldots\ldots \quad A\text{-}27$$

This force is balanced by an inward force normal to the spherical surface. The balancing force is the component of the surface-tension normal to the free-surface and for a unit length of each of the four cuts in figure 2.2, is $\gamma \sin(d\alpha_2/2)$. The total force considering all four sides of the cut is therefore

$F_{below}=2\ \gamma r_1\ d\alpha_1 \sin(d\alpha_2/2)+ 2\ \gamma r_2\ d\alpha_2 \sin(d\alpha_1/2)$ …………………………………*A-28*

Thus by equating equations 2.23 and 2.24, we can write that:

$r_1\ d\alpha_1\ r_2\ d\alpha_2\ \Delta P = 2\ \gamma r_1\ d\alpha_1 \sin(d\alpha_2/2)+ 2\ \gamma r_2\ d\alpha_2 \sin(d\alpha_1/2)$ ……………………*A-29*

but since $d\alpha_2$ is very small (i.e $\sin(d\alpha_2/2) = d\alpha_2/2$) we have that

$r_1\ d\alpha_1\ r_2\ d\alpha_2\ \Delta P = 2\ \gamma r_1\ d\alpha_1\ d\alpha_2/2+ 2\ \gamma r_2\ d\alpha_2\ d\alpha_1/2$ ………………………………A-*30*

which implies that

$r_1\ d\alpha_1\ r_2\ d\alpha_2\ \Delta P = \gamma r_1\ d\alpha_1\ d\alpha_2+ \gamma r_2\ d\alpha_2\ d\alpha_1= \gamma\ (r_1\ d\alpha_1\ d\alpha_2+ r_2\ d\alpha_2\ d\alpha_1)$ ………*A-31*

and finally

$\Delta P = \gamma(1/r_1 + 1/r_2\ )$ …………………………………………………………*A-32*

This pressure jump at the free surface may be represented as a volume force which is added as a source term in the momentum equation to represent the effect of surface tension.

APPENDIX A3: Linear-wave theory

Since the amplitude is assumed small it is also implied that wave steepness is negligible (i.e $d\Phi/dx * d\zeta/dx \rightarrow 0$) so that the kinematic free surface conditions becomes

$w = d\Phi/dz = d\zeta/dt$ ……………………………………………………*A-33*

By substituting this kinematic free surface condition into the dynamic free surface condition (equation *2.18*) we obtain a single equation in Φ:

$w = d[-1/g . \delta\Phi/\delta t]/dt = d\Phi/dz$ so that:

$\delta^2\Phi/\delta t^2 = -g\, d\Phi/dz$ ……………………………………………………*A-34*

Considering that the wave ζ is of the form

$\zeta = ae^{i(kx-\omega t)}$ ……………………………………………………*A-35*

Where a, k and ω represent amplitude, wave-number and frequency respectively.

In the light of equations *A-33 to A-35*, we can write (assuming the solution of equation *A-34* can be given as a product of the 3 variables x, z and t) that:

$\Phi=X(x)\,Z(z)\,T(t)$ ……………………………………………………A-36

The laplace equation gives that:

$$\frac{\partial^2\phi}{\partial x^2}+\frac{\partial^2\phi}{\partial z^2}=\left[X^{''}(x)Z(z)+X(x)Z^{''}(z)\right]T(t)=0 \quad \text{……………………A-37}$$

Assuming $T(t)\neq 0$

$$X^{''}(x)Z(z)+X(x)Z^{''}(z)=0 \quad \text{…………………………………………A-38}$$

So that $X^{''}(x)Z(z)=-X(x)Z^{''}(z)$ and eventually

$$\frac{X^{''}(x)}{X(x)}=\frac{Z^{''}(z)}{Z(z)} \quad \text{…………………………………………………A-39}$$

Assuming equation *A-39* is equal to the constant $-k^2$ (negative sign chosen to get harmonic solution in *x* direction), we have that:

$$\frac{X^{''}(x)}{X(x)}=-k^2 \qquad \text{Therefore,}$$

$$X^{''}(x)-k^2X(x)=0 \qquad \text{and similarly:}$$

$$Z^{''}(z)-k^2Z(z)=0$$

The solution to these second order differential equations in x and z is of the form:

$X(x)=Ae^{ikx}+ Be^{-ikx}$ ……………………………………………………A-40

$Z(z)=Ce^{ikz}+ De^{-ikz}$ ………………………………………………………A-41

Substituting equations *A-40* and *A-41* into *A-36* gives:

$\Phi=(Ae^{ikx}+ Be^{-ikx})(Ce^{ikz}+ De^{-ikz})\,T(t)$ where $T(t)\equiv e^{-i\omega t}$ (time variation of the wave)

Assuming the wave is propagating to the right, we can obtain a solution by setting A=1 and B=0 so that:

$\Phi=(1e^{ikx}+ 0e^{-ikx})(Ce^{ikz}+ De^{-ikz})\,e^{-i\omega t}$ which gives:

$\Phi= (Ce^{ikz}+ De^{-ikz})\,e^{i(kx-i\omega t)}$ ………………………………A-42

The no slip condition *(equation 2.8)* at the sea-bed (-d) implies from *equation 2.9* that

$w=\dfrac{\partial \phi}{\partial z}=0$ at z = -d ……………………………………………A-42

Thus by differentiating equation A-42 with respect to z we obtain:

$$\frac{\partial \phi}{\partial z}=\left[kCe^{kz}-kDe^{-kz}\right]e^{i(kx-\omega t)}$$ ……………………………………………A-43

Equating equations *A-42* and *A-43* (and substituting z = -d) gives:

$$[kCe^{k(-d)} - kDe^{-k(-d)}].e^{i(kx-\omega t)} = 0$$

Since $k \neq 0$ and $e^{i(kx-\omega t)} \neq 0$, it follows that $Ce^{-kd} - De^{kd} = 0$. Therefore

$C = De^{kd}/e^{-kd} = De^{kd-(-kd)} = De^{2kd}$ ……………………………………………A-44

Substituting equation *A-44* into *A-41* gives:

$Z(z)= De^{2kd}e^{kz} + De^{-kz} = De^{2kd} [e^{kz} + e^{-kz-2kd}]= De^{2kd} [e^{kz} + e^{-k(z+2d)}]$

$= De^{2kd} [e^{kz} + e^{-k(z+2d)}] (e^{2kd}/e^{2kd}) =De^{kd} [e^{kz+kd} + e^{-k(z+2d)+kd}]$

$= De^{kd} [e^{k(z+d)} + e^{-k(z+2d-d)}]= De^{kd} [e^{k(z+d)} + e^{-k(z+d)}]$ ……………………A-45

But $[e^{k(z+d)}+e^{-k(z+d)}]/2 = \cosh[k(z+d)]$, so that $[e^{k(z+d)}+e^{-k(z+d)}]=2\cosh[k(z+d)]$

Substituting into equation *A-45* gives:

$Z(z) = 2 De^{kd}\cosh[k(z+d)]$ ……………………………………………A-46

Recall from equations *A-42* and *A-40* that

$\Phi= (Ce^{ikz}+ De^{-ikz}) e^{i(kx-\omega t)} \equiv Z(z) e^{i(kx-\omega t)}$ ……………………………………*A-47*

Substituting *equation 2.54* into *2.55* gives:

$\Phi= 2 De^{kd}\cosh[k(z+d)] e^{i(kx-\omega t)}$ ………………………………………………*A-48*

The only unknown variable in the Φ function above *(equation A-48)* is D and to obtain it, we differentiate *it* with respect to *z,* giving

$$\frac{\partial\phi}{\partial z} = 2kDe^{kd}\sinh(kd)e^{i(kx-\omega t)}$$ ………………………………………A-49

Substituting *equation A-49* back into *A-33* (kinematic free surface condition assuming negligible steepness we have that:

$2kDe^{kd}\sinh(kd)e^{i(kx-\omega t)} = d\zeta/dt$ ………………………………………A-50

But from equation *A-35*

$d\zeta/dt = d(ae^{i(kx-\omega t)})/dt = -a\omega i e^{i(kx-\omega t)}$ ………………………………A-51

so that equation *A-50* becomes

$2kDe^{kd}\sinh(kd)e^{i(kx-\omega t)} = -a\omega i e^{i(kx-\omega t)}$ therefore

$D = -a\omega i / 2ke^{kd}\sinh(kd)$ …………………………………………........A-52

Going back to equation *A-48* and substituting equation *A-51* we have:

$\Phi = 2e^{kd}\cosh[k(z+d)]\, e^{i(kx-\omega t)}(-a\omega i)/2ke^{kd}\sinh(kd)$ …………………*A-53*

Therefore,

$$\phi = -a\omega i\frac{\cosh[k(z+d)]}{k\sinh(kd)}e^{i(kx-\omega t)}$$ ………………………………………*A-54*

Recall from equation *A-34* that

$\delta^2\Phi/\delta t^2 = -g\, d\Phi/dz$

Differentiating equation *A-48* with respect to t gives:

$\frac{\partial \phi}{\partial t} = -i\omega 2De^{kd}\cosh[k(z+d)].e^{i(kx-\omega t)}$ and

$$\frac{\partial}{\partial t}(\frac{\partial \phi}{\partial t}) = \frac{\partial^2 \phi}{\partial t^2} = -i^2\omega^2 2De^{kd}\cosh[k(z+d)].e^{i(kx-\omega t)}$$

So that:

$$\frac{\partial^2 \phi}{\partial t^2} = -\omega^2 2De^{kd}\cosh[k(z+d)].e^{i(kx-\omega t)} \quad \ldots\ldots\ldots\ldots\ldots\ldots\ldots\ldots\ldots A\text{-}55$$

Therefore, substituting equation *A-49* and *A-54* into the dynamic free surface condition (equation 2.18) yields:

$$\frac{\partial^2 \phi}{\partial t^2} = -g\frac{\partial \phi}{\partial z} = -\omega^2 2De^{kd}\cosh[k(z+d)].e^{i(kx-\omega t)} = -g2kDe^{kd}\sinh(kd)e^{i(kx-\omega t)} \ldots\ldots\ldots A\text{-}56$$

Simplifying equation *A-56* above gives:

$$-\omega^2\cosh[k(z+d)] = -gk\sinh(kd) \quad \ldots\ldots\ldots\ldots\ldots\ldots\ldots\ldots\ldots A\text{-}57$$

Taking z+d≈d, equation *A-57* becomes

$\omega^2 = gk\frac{\sinh(kd)}{\cosh(kd)}$ which implies that:

$\omega^2 = gk\tanh(kd)$ and therefore,

$$k = \frac{\omega^2}{g\tanh(kd)} \quad \ldots\ldots\ldots\ldots\ldots\ldots\ldots\ldots\ldots\ldots\ldots\ldots A\text{-}58$$

Inserting the above equation *A-58* in *A-54*, we get:

$$\phi = -a\omega i \frac{g \tanh(kd)}{\omega^2} \frac{\cosh[k(z+d)]}{\sinh(kd)} = -a\frac{g}{\omega} i \frac{\cosh[k(z+d)]}{\sinh(kd)} \frac{\sinh(kd)}{\cosh(kd)} e^{i(kx-\omega t)}$$

Therefore,

$$\phi = -a\frac{g}{\omega} i \frac{\cosh[k(z+d)]}{\cosh(kd)} e^{i(kx-\omega t)} \ldots\ldots\ldots\ldots\ldots\ldots\ldots\ldots\ldots\ldots\ldots\ldots\ldots\ldots A\text{-}59$$

Equation *A-59* can be written as:

$$\phi = -a\frac{g}{\omega} i \frac{\cosh[k(z+d)]}{\cosh(kd)} [\cos(kx-\omega t) + i\sin(kx-\omega t)]$$

Expanding the bracket [ ] gives:

$$\phi = -a\frac{g}{\omega} i \frac{\cosh[k(z+d)]}{\cosh(kd)} \cos(kx-\omega t) + a\frac{g}{\omega} \frac{\cosh[k(z+d)]}{\cosh(kd)} \sin(kx-\omega t)]$$

The corresponding real-valued Φ function is thus given as:

$$\phi = a\frac{g}{\omega} \frac{\cosh[k(z+d)]}{\cosh(kd)} \sin(kx-\omega t)] \ldots\ldots\ldots\ldots\ldots\ldots\ldots\ldots\ldots\ldots\ldots\ldots\ldots A\text{-}60$$

Recall from the dynamic free-surface boundary condition (equation 2.18) that

$$\zeta = -\frac{1}{g}\frac{\partial \phi}{\partial t}$$

Therefore the wave elevation ζ is given by differentiating equation *A-60* with respect to t:

$\zeta = -\frac{1}{g} a \frac{g}{\omega} \frac{\cosh[k(z+d)]}{\cosh(kd)} [-\omega \cos(kx - \omega t)]$. Near the free-surface, z→0

Therefore:

$\zeta = a \frac{\cosh[k(0+d)]}{\cosh(kd)} \cos(kx - \omega t)$ so that:

$\zeta(x,t) = a \cos(kx - \omega t)$ *A-61*

APPENDIX A4: Fifth-Order Stokes Wave

Fenton (1985) considered periodic waves propagated without change of form over a layer of fluid on a horizontal impermeable bed, where the origin is on the bed, the horizontal coordinate is x and the vertical coordinate is y, on a moving reference frame.

By assuming incompressibility Fenton (1985) introduced a stream function φ such that velocity components u and v in the x and y directions respectively, could be written

as $u = \delta\varphi / \delta x$ and $v = -\delta\varphi / \delta y$. Fenton further assumed irrotational flow so that ψ satisfied the Laplace equation i.e $\delta^2\varphi / \delta x^2 + \delta^2\varphi / \delta y^2 = 0$

On the free-surface $y = \zeta(x)$, the kinematic boundary condition applies:

$\varphi\ [x, \zeta(x)] = -Q$ where Q is a position constant denoting the total volume flow-rate underneath the stationary wave per unit length normal to the x-y plane.

By requiring constant pressure on the free-surface and combining with bernoulli's equation, we have:

$$\tfrac{1}{2}[\delta^2\varphi / \delta x^2 + \delta^2\varphi / \delta y^2] + g\zeta = R$$

G is the gravitational acceleration and R is a positive constant.

Fenton obtained a solution in terms of d (water-depth), H(wave-height) and λ(wave-length) by assuming the traditional expansion for φ

$$\frac{k\varphi}{u} = -ky + \sum_{i=1}^{\infty}\sum_{j=1}^{i} \mathrm{f_{ij}}\epsilon^{\mathrm{i}} \sinh(\mathrm{jky})\cos(\mathrm{jkx})$$

Where u = mean fluid speed for any constant value of y, k=2π/λ (wave-number) and ϵ = kH/2 (wave slope). By substituting the expansion for ψ into the kinematic boundary condition and bernoulli's equation, we can write that:

$$\frac{kQ}{u} = -k\zeta(\mathrm{x}) + \sum_{i=1}^{\infty}\sum_{j=1}^{i} \mathrm{f_{ij}}\epsilon^{\mathrm{i}}\sinh(\mathrm{jky})\cos(\mathrm{jkx})$$

By further assuming uniform flow in the fluid of depth d and speed $c_o(g/k)^{1/2}$ in the negative x direction, a perturbation expansion in terms of ϵ is obtained thus:

$$\mathrm{k}\zeta(\mathrm{x}) = kd + \sum_{i=1}^{\infty}\sum_{j=1}^{i} \mathrm{f_{ij}}\epsilon^{\mathrm{i}}\sinh(\mathrm{jky})\cos(\mathrm{jkx})$$

Fenton expanded the above equation to the fifth order and after a great amount of mathematical manipulation, gave the solution for kd/2π > 0.5 (deep water) as:

$$k\zeta(x) = kd + \epsilon\cos(kx) + \epsilon^2 B_{22}\cos(2kx) + \epsilon^3 B_{31}[\cos(kx) - \cos(3kx)] + \epsilon^4[B_{42}\cos(2kx) + B_{44}\cos(4kx)] + \epsilon^5[-(B_{53} + B_{55})\cos(kx) + B_{53}\cos(3kx) + B_{55}\cos(5kx) + 0(\epsilon^6)]$$

where $B_{22} = ½$, $B_{31} = -3/8$, $B_{42} = 1/3$, $B_{44} = 1/3$, $B_{53} = 99/128$ and $B_{55} = 125/384$. $0(\epsilon^6)$ represents higher order terms which are assumed negligible.

Since $\epsilon = kH/2$ where $H/2 = a$ (wave amplitude), $\epsilon/k = a$. So by replacing the phasing (kx) in each term with $\theta = kx-\omega t$ in the light of Fenton's solution, we can write with respect to a mean surface elevation $y=0$, that

$\zeta(x,t) = a\cos(kx-\omega t) + a^2 B_{22}\cos(2(kx-\omega t)) + a^3 B_{31}\,[\cos(kx-\omega t) - \cos(3(kx-\omega t))] + a^4[B_{42}\cos(2(kx-\omega t)) + B_{44}\cos(4(kx-\omega t))] + a^5[-(B_{53} + B_{55})\cos(kx-\omega t) + B_{53}\cos(3(kx-\omega t)) + B_{55}\cos(5(kx-\omega t))]$.

APPENDIX A5: RANS turbulence Modelling

In the Reynolds-Averaged form (see e.g Hewitt and Reeks, 2005 and Ferziger and Peric, 2002), the continuity equation (A1) may be written as:

$$\frac{\partial(\rho U_i)}{\partial x_i} = 0 \qquad (0.1)$$

while the momentum equations (A24 - A26) is as follows:

$$U_j \frac{\partial U_i}{\partial x_j} = \frac{1}{\rho}\frac{\partial P}{\partial x_i} + \frac{\partial}{\partial x_i}\left(\nu \frac{\partial U_i}{\partial X_j} - \overline{u_i' u_j'}\right) \qquad (0.2)$$

where U_i is the time averaged velocity in the direction x_i, ρ the fluid velocity, P the pressure, ν the kinematic viscosity and u_i' the instantaneous velocity (relative to U_i) of the fluid in the direction x_i. The term $\overline{u_i' u_j'}$ represents the turbulent motion which is averaged and the product $\rho\overline{u_i' u_j'}$ is the Reynold's stress.

Apparently, the RANS equations are 4 in 3-dimensions (one continuity and three momentum) but there are 10 unknowns (three *U, six* $\overline{u_i' u_j'}$ and one *P)* which means that the equations are not closed. Since the action of the Reynold's stresses are similar to the viscous stresses (Ferziger and Peric, 2002), they are modelled in the same way but in terms of a turbulent kinematic viscosity, ν_t :

$$-\overline{u_i' u_j'} = \nu_t\left(\frac{\partial U_i}{\partial x_j} + \frac{\partial U_j}{\partial x_i}\right) \qquad (0.3)$$

By inserting 3.3 in 3.2, equation 3.2 may be written as:

$$\boldsymbol{U_j \frac{\partial U_i}{\partial x_j} = \frac{1}{\rho}\frac{\partial P}{\partial x_i} + \frac{\partial}{\partial x_i}[(\nu + \nu_t)\frac{\partial U_i}{\partial X_j}]} \tag{0.4}$$

In this form, there are only 5 unknowns (3 *U,* one *P* and one μ_t). By defining an expression for ν_t, we get a fifth equation such that the number of unknowns are now equal to the number of equations and the equations are then said to be closed.

Therefore, the majority of turbulence modelling in the RANS approach is related to developing a good expression forν_t. To begin with, dimensional analysis (Ferziger and Peric, 2002) shows that:

$$\boldsymbol{\nu_t \propto ul} \tag{0.5}$$

where *u* is the same as in 3.2 and *l* is a characteristic length scale. This relationship constitutes a basis for the various RANS methods of determining ν_t. In the RANS approach, there are essentially four main methods for modelling ν_t and by extension, turbulence.

Mixing-length: This is the simplest and assumes that the only important mean velocity gradients interacting with the turbulent scales *u* is $\frac{\partial U}{\partial y}$ such that $u=l\frac{\partial U}{\partial y}$ and from 3.5

$$\boldsymbol{\nu_t = l^2 \frac{\partial U}{\partial y}} \tag{0.6}$$

Spalart-Almaras: The method gives ν_t in terms of a modified turbulent viscosity $\tilde{\nu}$ as:

$$\boldsymbol{\nu_t} = \frac{\tilde{\nu}\,(\frac{\tilde{\nu}}{\nu})^3}{(\frac{\tilde{\nu}}{\nu})^3 + C_{\nu 1}} \qquad (0.7)$$

where $C_{v1}$is an empirically defined constant and $\tilde{\nu}$ is obtained by solving the corresponding transport equation given by Spalart and Almaras (1992).

K-ε (k-epsilon): The method gives ν_t in terms of dissipation, ε and a turbulent kinetic energy, k which may be obtained by solving the corresponding transport equation given in standard literature (e.g Ferziger and Peric, 2002 and Fluent 6.3 user's manual) . Based on the assumption of equilibrium turbulent flow i.e rates of production and destruction of turbulence are approximately equal (Ferziger and Peric, 2002), ε and k are related by $\varepsilon \approx \frac{k^{3/2}}{l}$ so that :

$$l \approx \frac{k^{3/2}}{\varepsilon} \qquad (0.8)$$

Since naturally k $\propto$ u^2 (kinetic energy is proportional to square of flow velocity), we can write that:

$$u \propto k^{1/2} \qquad (0.9)$$

Therefore substituting 3.8 and 3.9 in the basic relationship of 3.5 we have:

$$\nu_t = C_\rho\, k^{1/2} \frac{k^{3/2}}{\varepsilon} = C_\rho \frac{k^2}{\varepsilon} \qquad (0.10)$$

where C_ρ is an empirically defined constant.

There are at least 3 variants of this method:

1. Standard

2. RNG- **R**e**N**ormalization **G**roup theory (large eddies are removed methematically)
3. Realizable – terms in the equation are tuned to ensure a physical (realizable) behaviour.

K-ω (k-omega): The method gives ν_t in terms of k and ω (specific dissipation rate) rather than ε (dissipation):

$$\boldsymbol{\nu_t = \frac{k}{\omega}} \tag{0.11}$$

where ω is obtained by similarly solving the transport equation given in standard texts (e.g Wilcox, 1988).

APPENDIX A6: Code (UDF) used to initialize the FLUENT simulation

```
/*This is the beginning of the udf to generate a wave packet
according new-wave theory as modifefed by Barltrop & Xu, 2005*/
#include "udf.h"
#include "stdio.h"
#include "math.h"


/*Sea state parameters*/
#define Hs    21.5579/*Significant wave height*/
#define Tz      13.4/* zero-crossing period*/
#define Beta    0.0/*Barltrop and Xu's steepness balance factor
                                        0<=ALPHA<=1*/
#define scale  800      /* scale written as 1:scale*/
#define N_frequencysteps 30
#define Fcut 2.25                    /*Upper Spectral Cut-off
Frequency*/
#define ffcut 0.65                    /*Lower Spectral Cut-off
Frequency*/
#define Target_position  80.0  /*according to calculation, Target
time is at about 11.612s*/
#define TimeShift 63                 /*time series shifted foreward
using 63s(the higher this value the closer to zero the initial
conditions will be) phase lag so that extreme event occurs at time
Tg+TimeShift and Surface elevation is zero at time zero in line
with initializing a new-wave in FLUENT*/
#define sten 0.073       /* surface tension coefficient*/


/*other particulars*/

#define Num    0.7
#define PI  3.14159265358979
#define XOR   0                             /*Inlet origin*/
#define YOR   0                       /*Height origin*/
#define SIDE  1
#define Record_time     3
const real gamma=2.0;/*  Spectral Peak enhancement factor*/
#define kb       1.4085                         /*  One of the
many Spectral coefficients*/
#define Uvel  0.0
#define Vvel  0.0
#define wDEN  998.2                         /*density of fresh
water*/
#define aDEN  1.225                         /*air density*/
#define dw     207.414               /*water depth*/

/*free-surface Pressure damping extent*/
#define x_zero 175.0 /*beginning of damping zone*/
#define x_one 312.0/*end of domain*/
```

```
/*Global declarations*/
/*real THETA[N_frequencysteps];*/
real K[N_frequencysteps];
real omega[N_frequencysteps];
real Abs_S_newwave[N_frequencysteps];
real arg_S_newwave[N_frequencysteps];
int j;
real TSi_omega[N_frequencysteps];
real old_K[N_frequencysteps];
real precision;
real f[N_frequencysteps];
real fprime[N_frequencysteps];


/* PART THREE: GIVES WAVE HEIGHT AT ANY TIME t(INSTATNTANEOUS WATER
SURFACE ELEVATION) FOR ANY HORIZONTAL POSITION x*/

real wave_heightabove(real t,real x)
{
real waveheightsin, nonlinear;
real NL,NLH;
real kd,S22,S31,S33,S42,S44,S55,S51,S53;
real ALPHA;
real Kp;
real K_gamma;
real Max_frequency;
real Min_frequency;
real  Delta_omega;
real Target_time;
real Aa[N_frequencysteps];
real Bb[N_frequencysteps];

real waveheight;
real Zigma;
real a[N_frequencysteps];
real E_Spectrum[N_frequencysteps];
real S_Spectrum[N_frequencysteps];

real A;
real B[N_frequencysteps];
real Zeroth_Moment;
real S_max;
real S_newwave[N_frequencysteps];
real Sum_S_Spectrum;

      Kp=1.17+0.327*exp(-0.315*gamma); /*      */
      K_gamma=1-(0.285*log(gamma));
      Max_frequency=(Fcut*2*PI)/(Kp*Tz);
      Min_frequency= (ffcut*2*PI)/(Kp*Tz) ;
      Delta_omega=(Max_frequency-Min_frequency)/(N_frequencysteps-
1);

      ALPHA=Beta/(((5*Hs/80)*(1-Beta))+Beta);
```

```
      Zeroth_Moment=0;
      Sum_S_Spectrum=0;

for (j=0;j<N_frequencysteps;j++)
  {
      omega[j]=Min_frequency+(j* Delta_omega);
      K[j]=(omega[j]*omega[j])/9.81;
      /*
      this "while" loop includes the effect of surface-tension in
the Wave-number, K  by iterating (Using Newton-Raphson method)
      to find the value of K at which w^2 -(gk +
sten*k^3/wDEN)tanh(kd) is zero */
      precision=0.0001;
      old_K[j]=0.0052;

      while ( fabs(K[j]-old_K[j])>precision)
      {
            old_K[j]=K[j];


      f[j]=((9.806*K[j])+(sten*scale*scale*K[j]*K[j]*K[j]/wDEN))*ta
nh(K[j]*dw)-(omega[j]*omega[j]);


      fprime[j]=((9.806+(3*sten*scale*scale*K[j]*K[j]/wDEN))*tanh(K
[j]*dw))-
(K[j]*dw*(9.806+(sten*scale*scale*K[j]*K[j]/wDEN))/(cosh(K[j]*dw)*c
osh(K[j]*dw)));

            K[j]=K[j]-(f[j]/fprime[j]);
      }


/* this following calculates JONSWAP spectrum */

      if( omega[j]/(2*PI) < 1.0/(Kp*Tz))
      {
            Zigma=0.07;
      }
      else
      {
            Zigma=0.09;
      }


      a[j]=exp(-(((omega[j]*Kp*Tz/(2*PI))-
1)*((omega[j]*Kp*Tz/(2*PI))-1))/(2*Zigma*Zigma));

E_Spectrum[j]=(pow((2*PI/omega[j]),5)*exp((-1/PI)*pow((omega[j]*
Kp*Tz/(2*PI*kb)),4))*((pow(kb,4)*Hs*Hs*K_gamma)/(8*PI*PI*pow((Kp*Tz
),4)))*pow(gamma,a[j])); /*JONSWAP spectrum*/
```

```
      A=(1-ALPHA)/(5*Hs);
      B[j]=-ALPHA*K[j];  /* A and B[j] are the real and imaginary
parts respectively, of Barltrop and Xu's steepness function*/



      S_Spectrum[j]=((A*A)+(B[j]*B[j]))*E_Spectrum[j];/* spectrum
of water surface slope/ front steepness*/


      /*..............................................*/

      Sum_S_Spectrum=Sum_S_Spectrum + S_Spectrum[j];

      /*initialize zeroth moment of slope/front-steepness
spectrum*/

      Zeroth_Moment=Zeroth_Moment + (S_Spectrum[j]*Delta_omega);
   }



S_max=0.5*sqrt(8*Zeroth_Moment*log(3600*Record_time/Tz));/* note
that this is for a half wave-height(i.e amplitude). For a full wave
height S_max=sqrt(8*Zeroth_Moment*log(Record_time*3600/Tz))*/

Target_time=2*Target_position*omega[N_frequencysteps-1]/9.81;


/*the  maximum slope/front steepness in the specific
duration,t="Record_time" is given as S_max....normally we know
this is the highest within the record time but we dont know when it
occurs in a stochastic process, so we traditionally
simulate the whole record time . However using the new-wave theory,
we can have an average idea of what
the most probable wave will look like so we use it right-away
without waiting to simulate the whole record time*/

waveheightsin=0;
waveheight=0;
      for (j=0;j<N_frequencysteps;j++)
      {

            S_newwave[j]=S_max*S_Spectrum[j]/Sum_S_Spectrum ;
/*Average of the most probabble extreme values of front
steepness/slope using
"New-wave theory"*/

            /*to convert front steepness/slope extreme value to
wave (i.e amplitude) extreme value we reverse-transform with
Barltrop and Xu's steepness function(the calculation here is done
in the real plane by representing the real part by a real number Aa
and the imaginary part by another real number Bb, rather than the
original complex plane */

            Aa[j]=S_newwave[j]*A/((A*A)+(B[j]*B[j]));
```

```
            Bb[j]=-S_newwave[j]*B[j]/((A*A)+(B[j]*B[j]));


      Abs_S_newwave[j]=sqrt((Aa[j]*Aa[j])+(Bb[j]*Bb[j]));/*magnitu-
de of the "most probable extreme" amplitude of each j frequency
component*/



            if(Bb[j]==0.0){arg_S_newwave[j]=0;} /*added to avoid
overflow errors(computing atan 0)*/

            else {arg_S_newwave[j]=atan2(Bb[j],Aa[j]);}  /*
arguement/angle/phasing of each j frequency component of the
"most probable extreme wave" */

                        TSi_omega[j]=(omega[j]*Target_time)-
(K[j]*Target_position); /*phasing is chosen such that all frequency
components become co-phased at x=Target_position*/


                        /*the mean temporal,t and spacial,x history
of most probable extreme water surface elevation  may be given
                        to 1st order(linear wave theory)as:*/


            /*        initialize wave-height of random sea*/

            waveheight=waveheight+(Abs_S_newwave[j]*cos(K[j]*x-
            (omega[j]*(t-TimeShift))+TSi_omega[j]+
            arg_S_newwave[j]));


            waveheightsin=waveheightsin+(Abs_S_newwave[j]*sin(K[j]*
            x-(omega[j]*(t-TimeShift))+TSi_omega[j]+
            arg_S_newwave[j]));



      }

      /*calculate non-linear wave-height according to Walker et
al(2005) */
NL=waveheight;        /*linear description*/
NLH=waveheightsin;    /*hilbert transform of the linear
description*/

kd=((2*PI/Tz)*(2*PI/Tz)*dw)/9.81;

S22=0.5*kd/dw;
S31=(-kd/dw)*(kd/dw)*3/8;
S33=(kd/dw)*(kd/dw)*3/8;
S42=(kd/dw)*(kd/dw)*(kd/dw)/3;
S44=S42;
S53=(kd/dw)*(kd/dw)*(kd/dw)*(kd/dw)*99/128;
S55=(kd/dw)*(kd/dw)*(kd/dw)*(kd/dw)*128/384;
```

```
S51=(kd/dw)*(kd/dw)*(kd/dw)*(kd/dw)*474/384;


nonlinear=NL+(S22*((NL*NL)-(NLH*NLH)))+(S31*((NL*NL)-
(NLH*NLH))*NL)+(S33*((NL*NL)-
(3*NLH*NLH))*NL)+(S42*((NL*NL)+(NLH*NLH))*((NL*NL)-(NLH*NLH)))
+(S44*((((NL*NL)-(NLH*NLH))*((NL*NL)-(NLH*NLH)))-
(2*NL*NLH*2*NL*NLH)))+(S51*((((NL*NL)-(NLH*NLH))*((NL*NL)-
(NLH*NLH)))*NL))
+(S53*((NL*NL)+(NLH*NLH))*NL*((NL*NL)-(3*NLH*NLH)))
+(S55*((((((NL*NL)+(NLH*NLH))*((NL*NL)+(NLH*NLH)))-
(2*NL*NLH*2*NL*NLH))*NL)-4*NLH*NLH*NL*((NL*NL)-(NLH*NLH))));

return nonlinear;
        }


/*GIVES U OF WAVE*/
real wave_u(real t, real x, real y)
{
        real u;
        real height;
        real depth_function[N_frequencysteps];
        if (y>0) {height=wave_heightabove(t,x);}
        else height=wave_heightabove(t,x);


        u=0; /*initialize x velocity profile*/

        for(j=0;j<N_frequencysteps;j++)
        {
                u=u+(Abs_S_newwave[j]*exp(K[j]*y)*omega[j]*cos(K[j]*x-
                (omega[j]*(t-
                TimeShift))+TSi_omega[j]+arg_S_newwave[j]));
        }


        return u;
}


/*GIVES V OF WAVE*/
real wave_v(real t, real x, real y)
{
        real v;

        real height;
        real depth_function[N_frequencysteps];
        if (y>0) {height=wave_heightabove(t,x);}
        else height=wave_heightabove(t,x);


        v=0; /*initialize y velocity profile*/
        for(j=0;j<N_frequencysteps;j++)
        {
```

```
           v=v+(Abs_S_newwave[j]*exp(K[j]*y)*omega[j]*sin(K[j]*x-
           (omega[j]*(t-
           TimeShift))+TSi_omega[j]+arg_S_newwave[j]));
      }

      return v;

}



/*
  DEFINES X inlet VELOCITY
*/
DEFINE_PROFILE(inlet_x_velocity, thread, position)
{
      real x[ND_ND];          /* this will hold the position vector
*/
      real y;
      face_t f;
      real t;
      real height;

      t=CURRENT_TIME;

      begin_f_loop(f, thread)
      {
                  F_CENTROID(x,f,thread);
                  y = x[1];
                  if (y>0) {height=wave_heightabove(t,0.0);}
                  else height=wave_heightabove(t,0.0);


                  if(y>YOR+height){F_PROFILE(f, thread,
position)=0.0+Uvel;}
                  else {F_PROFILE(f, thread, position)
=tf*wave_u(t,0.0,y-YOR)+Uvel;}
      }
      end_f_loop(f, thread)

      /*printf("Horizontal velocity  is \n", wave_u(0.0,0.0,y-
YOR));*/

}

/*
  DEFINES Y inlet VELOCITY
*/
DEFINE_PROFILE(inlet_y_velocity, thread, position)
{
  real x[ND_ND];        /* this will hold the position vector */
  real y;
  face_t f;
  real t;
  real height;
```

```
  t=CURRENT_TIME;

  begin_f_loop(f, thread)
    {
            F_CENTROID(x,f,thread);
            y = x[1];
            if (y>0) {height=wave_heightabove(t,0.0);}
            else height=wave_heightabove(t,0.0);


            if(y>YOR+height){F_PROFILE(f, thread,
position)=0.0+Uvel;}
            /*printf("Vertical velocity  is \n", wave_v(0.0,0.0,y-
YOR));*/
            else {F_PROFILE(f, thread, position) =
tf*wave_v(t,0.0,y-YOR)+Uvel;}
    }
  end_f_loop(f, thread)
}

/*
  DEFINES PHASES CONCENTRATION
*/
DEFINE_PROFILE(phase2_inlet, thread, position)
{
  real x[ND_ND];        /* this will hold the position vector */
  real y;
  face_t f;
  real t;
  real height;

  t=CURRENT_TIME;

  begin_f_loop(f, thread)
    {
            F_CENTROID(x,f,thread);
            y = x[1];

            if (y>0) {height=wave_heightabove(t,0.0);}
            else height=wave_heightabove(t,0.0);

            if(y>YOR+height){F_PROFILE(f, thread, position)=0;}
            else { F_PROFILE(f, thread, position)=1;}
    }
  end_f_loop(f, thread)
}


DEFINE_PROFILE(DStream_pressure_outlet, thread, position)
{
  real x[ND_ND];        /* this will hold the position vector */
  real y;
  face_t f;
  real t;

  real u_vel;
```

```
  real v_vel;


  t=CURRENT_TIME;

  begin_f_loop(f, thread)
  {
            F_CENTROID(x,f,thread);
            y = x[1];
            /*real height;     height=wave_height(t,x_one);
using x=x_one=245.0 is because grid lenght of 245.0m is used*/

            u_vel=0;/*wave_u( t, x_one, y-YOR);*/
            v_vel=0;/*wave_v( t, x_one, y-YOR) ;*/

            F_PROFILE(f, thread, position)=-wDEN*9.81*(y-YOR);

            if(y>YOR){F_PROFILE(f, thread, position)=0.0;}
  }
  end_f_loop(f, thread)
}


/*
  DEFINES PHASES CONCENTRATION
*/
DEFINE_PROFILE(phase2_outlet, thread, position)
{
  real x[ND_ND];        /* this will hold the position vector */
  real y;
  face_t f;
  real t;

  t=CURRENT_TIME;

  begin_f_loop(f, thread)
    {
      F_CENTROID(x,f,thread);
      y = x[1];

      /*height=wave_height(t, x_one);*/

      if(y>YOR){F_PROFILE(f, thread, position)=0;}
        else {F_PROFILE(f, thread, position)=1;}
    }
  end_f_loop(f, thread)
}
```

APPENDIX A7: Details of the *wave-rider* kinematics method

ENVIRONMENTAL CONDITIONS

Significant wave height $Hs := 0.0582 m \cdot \frac{32.941}{32.941}$

Spectral peak period $Tp := 1.5610 \cdot s$

Zero crossing Period $Tz := 0.710 Tp$

steepness balance factor $\alpha := 0$

Steepness Balance $\alpha_{SB} := \alpha$

$RECORDtime := 3$ (in Hours)

$NumberOf\_FrequencySteps := 234$

SPECTRAL ANALYSIS & New-Wave Theory

CALCULATION OF FACTORS

$\gamma := 2.0$

$K_b := 1.4084$ $\qquad K_p := 0.327 \cdot e^{-0.315 \cdot \gamma} + 1.17$ $\qquad K_\gamma := 1 - 0.285 \ln(\gamma)$

$\text{Peak}_{freq} := \frac{2 \cdot \pi}{K_p \cdot Tz}$ $\qquad \text{Max}_{freq} := \text{Peak}_{freq} \cdot 2.25$ $\qquad 3.1224$ $\qquad \text{Max}_{freq} = 0.7849 \frac{rad}{sec}$

Note the higher the value of Maxfreq the smaller the wave that is generated when $\alpha > 0$

$j := 1 .. \text{NumberOf\_FrequencySteps}$ $\qquad \delta\phi := \frac{\text{Max}_{freq}}{\text{NumberOf\_FrequencySteps}}$ $\qquad \phi_j := j \cdot \delta\phi$

$$\sigma_j := \text{if}\left[\frac{\phi_j}{2 \cdot \pi} < \left(K_p \cdot Tz\right)^{-1}, 0.07, 0.09\right]$$

$$a_j := e^{\frac{-\left[\left(\frac{\phi_j}{2\pi} \cdot K_p \cdot Tz\right) - 1\right]^2}{2 \cdot \left(\sigma_j\right)^2}}$$

Energy Spectrum With Frequency In rad/sec

$$S_{WE_j} := \left(\frac{2 \cdot \pi}{\phi_j}\right)^5 \cdot \left(\frac{1}{2 \cdot \pi}\right) \cdot \left[\frac{{K_b}^4 \cdot Hs^2 \cdot K_\gamma}{4 \cdot \pi \cdot \left(K_p \cdot Tz\right)^4}\right] \cdot e^{\frac{-1}{\pi} \left(\frac{\phi_j}{2 \cdot \pi} \cdot \frac{K_p}{K_b} \cdot Tz\right)^{-4}} \cdot \gamma^{a_j}$$

$f_p := \frac{1}{Tz \cdot K_p}$ $\qquad$ ***Spectral-Peak Frequency***

STEEPNESS TRANSFER FUNCTION

$i := \sqrt{-1}$

$k_j := \frac{(\phi_j)^2}{g}$ Wave number

$T_{c_j} := \frac{1 - \alpha_{SB}}{5 \cdot Hs} + -i \cdot \alpha_{SB} \cdot k_j$ Xu and Barltop’s transfer function

$S_{WS_j} := \left(\left| T_{c_j} \right| \right)^2 \cdot S_{WE_j}$ ***WAVE-SLOPE SPECTRUM***
(Incorporating Effects of Steepness)

$m_{0WE} := \sum_j \left(S_{WE_j} \cdot \delta\phi \right)$ **Zeroth Moment of the Energy Spectrum**

$\sigma_{AE} := \sqrt{m_{0WE}}$ Standard deviation of the amplitude spectrum

$\zeta_a := \sigma_{AE} \cdot \sqrt{2 \cdot \ln\left(\frac{RECORDtime3600\,s}{Tz} \right)}$

$w_j := \phi_j$

$m_o := \sum_j \left(S_{WS_j} \cdot \delta\phi \right)$ **Zeroth Moment of the Slope Spectrum**

$\sigma_x := \sqrt{m_o}$ Standard deviation of the slope spectrum

$$SumS_{ws} := \sum_j S_{WS_j}$$

$\chi_a := \sigma_x \cdot \sqrt{2 \cdot \ln(\mathrm{NumberOf\_FrequencySteps})}$ Maximum value of the amplitude of the quantity for the record time

$\chi_{n_j} := \frac{AMPmax \cdot S_{WS_j}}{SumS_{ws}}$ **Most probable extreme wave-slope, based on New-Wave Theory** (Troman et al, 1991)

$\zeta w_j := \frac{\chi_{n_j}}{T_{c_j}}$ **Amplitude Of the j^{th} Wave-Component having a Frequency of** wj.

Water Surface Elevation (Focused wave)

$x_{tg} := 100 \cdot m$ Target/focus Position

$$C_{gmin} := \frac{g}{w_{NumberOf\_FrequencySteps}} \cdot \frac{1}{2}$$ Celerity of the shortest wave

$$Tg := \frac{x_{tg}}{C_{gmin}}$$ Target Time Target Position

$$T\zeta\Phi_j := w_j \cdot T_g - \frac{(w_j)^2 \cdot x_{tg}}{g}$$

$\zeta w\Phi_j := \text{if}(\text{Im}(\zeta w_j) = 0, 0, \arg(\zeta w_j))$ Phase Angle of j th Wave.

$$\zeta(xx, tt) := \sum_j \left[|\zeta w_j| \cdot \cos\left[\frac{(w_j)^2 \cdot xx}{g} - w_j \cdot tt + T\zeta\Phi_j + \zeta w\Phi_j \right] \right]$$

Fifth-order New-Wave (Walker et al, 2004)

$$kd := \frac{\left(\frac{2\cdot\pi}{Tz}\right)^2 \cdot dw}{9.81 \cdot \frac{m}{s^2}}$$

$$\eta_L(xx, tt) := \sum_j \left(|\zeta w_j| \cdot \cos\left(k_j \cdot xx - w_j \cdot tt + T\zeta\Phi_j + \zeta w\Phi_j\right) \right)$$

$$\eta_{LH}(xx, tt) := \sum_j \left(|\zeta w_j| \cdot \sin\left(k_j \cdot xx - w_j \cdot tt + T\zeta\Phi_j + \zeta w\Phi_j\right) \right)$$

$$\zeta(xx, tt) := \sum_j \left[|\zeta w_j| \cdot \cos\left[\frac{(w_j)^2 \cdot xx}{g} - w_j \cdot tt + T\zeta\Phi_j + \zeta w\Phi_j \right] \right]$$

Phasing arranged in such a manner that all wavelets focus at a point in space (x_{tg}) or point in time (T_g)

$$s22 := \frac{kd}{dw}\cdot\frac{1}{2} \qquad s31 := -\left(\frac{kd}{dw}\right)^{2}\cdot\frac{3}{8}$$

$$s33 := \left(\frac{kd}{dw}\right)^{2}\cdot\frac{3}{8} \qquad s42 := \left(\frac{kd}{dw}\right)^{3}\cdot\frac{1}{3} \qquad s44 := \left(\frac{kd}{dw}\right)^{3}\cdot\frac{1}{3}$$

$$s51 := \left(\frac{kd}{dw}\right)^{4}\cdot\frac{474}{384} \qquad s53 := \left(\frac{kd}{dw}\right)^{4}\cdot\frac{99}{128} \qquad s55 := \left(\frac{kd}{dw}\right)^{4}\cdot\frac{128}{384}$$

$\zeta_{\text{NonLinear}} = \eta_L + (s_{22}/d)(\eta^2{}_L - \eta^2{}_{LH}) + (s_{31}/d^2)(\eta^2{}_L + \eta^2{}_{LH})\,\eta_L + (s_{33}/d^2)(\eta^2{}_L - 3\eta^2{}_{LH})\,\eta_L +$

$(s_{42}/d^3)(\eta^2{}_L + \eta^2{}_{LH})(\eta^2{}_L - 3\eta^2{}_{LH}) + (s_{44}/d^3)(\eta^2{}_L - \eta^2{}_{LH})^2 - (2\eta_L\,\eta_{LH})^2 + (s_{51}/d^4)(\eta^2{}_L + \eta^2{}_{LH})^2\,\eta_L +$

$(s_{53}/d^4)(\eta^2{}_L + \eta^2{}_{LH})[\eta_L(\eta^2{}_L - 3\eta^2{}_{LH})] + (s_{55}/d^4)(\eta^2{}_L - \eta^2{}_{LH})^2 - (2\eta_L\,\eta_{LH})^2\,\eta_L - 4\eta^2{}_{LH}\eta_L(\eta^2{}_L - \eta^2{}_{LH})$

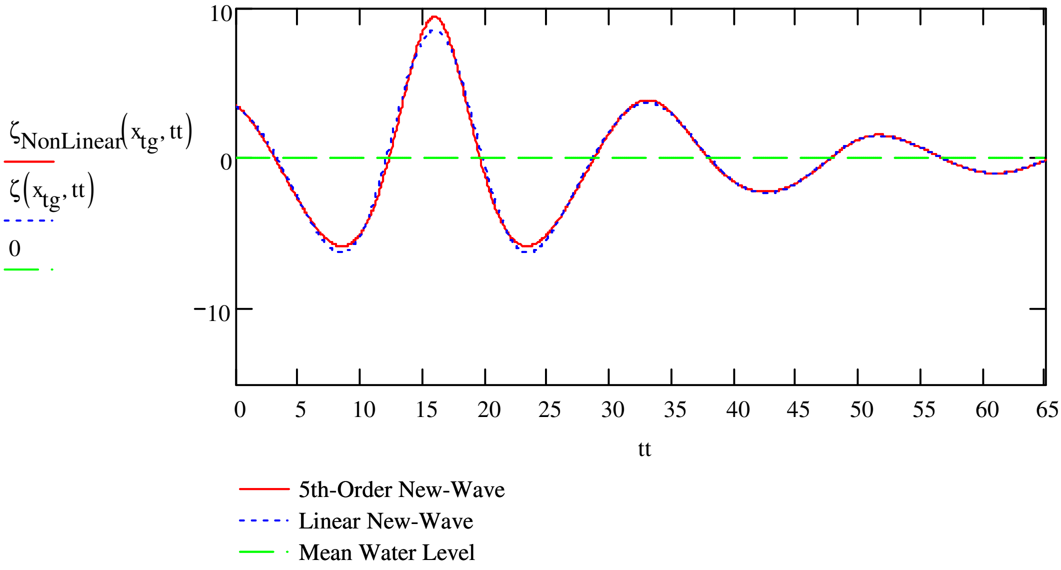

WAVE-RIDER KINEMATICS

Nn=NumberOf_FrequencySteps (Components)

$q := j$

$$nNum(j) := \min\left[3.8356\left(\frac{j}{Nn}\right)^4 - 10.93\left(\frac{j}{Nn}\right)^3 + 11.745\left(\frac{j}{Nn}\right)^2 - 5.8997\cdot\left(\frac{j}{Nn}\right) + 1.6669, 0.99\right]$$

Nn := NumberOf_FrequencySteps

$$gg(j, xx, tt) := \left|\zeta w_j\right|\cdot\cos\left[\frac{\left(w_j\right)^2\cdot xx}{g} - w_j\cdot tt + T\zeta\Phi_j + \zeta w\Phi_j\right]$$

Water Surface Profile contibuted by the jth frequency component

ii(j)=floor(nNum*j)

$$Gg(xx, tt) := \sum_j\left[\left|\zeta w_j\right|\cdot\cos\left[\frac{\left(w_j\right)^2\cdot xx}{g} - w_j\cdot tt + T\zeta\Phi_j + \zeta w\Phi_j\right]\right]$$

Overall Water Surface Profile

$$f(j, q) := \mathrm{if}\left[q > ii(j), \left(\frac{w_j}{w_q}\right) - 1, 1\right]$$

This is an arbitrary function defined for every jth wavelet in such a way that it assigns a value of unity to wavelets shorter than a certain fraction (nNum) of all wavelets up to the jth wavelet; and a value which decreases linearly at first then pseudo-exponentially, from 1 to 0 for wavelets above this threshhold defined by nNum.

$$Y(j, xx, tt) := \left[\sum_{q=1}^{j}\left(f(j, q)\cdot gg(q, xx, tt)\right)\right]$$

This is the baseline for the elevation of each jth wavelet. It is assumed that shorter wavelets are riding on longer ones so that the elevation of the shorter ones are measured from the water surface constituted by the longer wave. The f(j,q) function introduces the threshhold (nNum) below which wavelets are regarded as free waves and above which interaction sets in. This simplistic 2-wave interaction is extended to all j wavelets.

$\mathrm{Zz}(y, j, xx, tt) := y - Y(j, xx, tt)$ Elevation of each j wavelet at any vertical position y, time tt and position xx.

Velocity Profile Using the Linear Wave-rider

$$\mathrm{VELnew}(y, xx, tt) := \sum_{j} \left(w_j \cdot \exp\left(k_j \cdot \mathrm{Zz}(y, j, xx, tt)\right) \cdot \left|\zeta w_j\right| \cdot \cos\left(k_j \cdot xx - w_j \cdot tt + T\zeta\Phi_j + \zeta w\Phi_j\right)\right)$$

Velocity Profile Using a Higher (5th) Order form of Wave-rider

$$\eta_L(xx, yy, tt) := \sum_{j} \left(\exp\left(k_j \cdot \mathrm{Zz}(yy, j, xx, tt)\right) \cdot w_j \cdot \left|\zeta w_j\right| \cdot \cos\left(k_j \cdot xx - w_j \cdot tt + T\zeta\Phi_j + \zeta w\Phi_j\right)\right)$$

$$\eta_{LH}(xx, yy, tt) := \sum_{j} \left(\exp\left(k_j \cdot \mathrm{Zz}(yy, j, xx, tt)\right) \cdot w_j \cdot \left|\zeta w_j\right| \cdot \sin\left(k_j \cdot xx - w_j \cdot tt + T\zeta\Phi_j + \zeta w\Phi_j\right)\right)$$

$$kd := \frac{\left(\frac{2 \cdot \pi}{Tz}\right) \cdot dw}{9.81 \cdot \frac{m}{s^2}}$$

$$s22 := \frac{kd}{dw} \cdot \frac{1}{2} \qquad s31 := -\left(\frac{kd}{dw}\right)^2 \cdot \frac{3}{8} \qquad s33 := \left(\frac{kd}{dw}\right)^2 \cdot \frac{3}{8} \qquad s42 := \left(\frac{kd}{dw}\right)^3 \cdot \frac{1}{3}$$

$$s44 := \left(\frac{kd}{dw}\right)^3 \cdot \frac{1}{3} \qquad s51 := \left(\frac{kd}{dw}\right)^4 \cdot \frac{474}{384} \qquad s53 := \left(\frac{kd}{dw}\right)^4 \cdot \frac{99}{128} \qquad s55 := \left(\frac{kd}{dw}\right)^4 \cdot \frac{128}{384}$$

Nonlinear horizontal particle velocity

$$U_{\mathrm{NonLinear}}(x,y,t) = \eta_L + (s_{22}/d)(\eta^2_L - \eta^2_{LH}) + (s_{31}/d^2)(\eta^2_L + \eta^2_{LH})\,\eta_L + (s_{33}/d^2)(\eta^2_L - 3\eta^2_{LH})\,\eta_L$$

$$+ (s_{42}/d^3)(\eta^2_L + \eta^2_{LH})(\eta^2_L - 3\eta^2_{LH}) + (s_{44}/d^3)(\eta^2_L - \eta^2_{LH})^2 - (2\eta_L\,\eta_{LH})^2 + (s_{51}/d^4)(\eta^2_L + \eta^2_{LH})^2\,\eta_L$$

$$+ (s_{53}/d^4)(\eta^2_L + \eta^2_{LH})[\eta_L(\eta^2_L - 3\eta^2_{LH})] + (s_{55}/d^4)(\eta^2_L - \eta^2_{LH})^2 - (2\eta_L\,\eta_{LH})^2\,\eta_L - 4\eta^2_{LH}\eta_L(\eta^2_L - \eta^2_{LH})$$